Image Acquisition and Attenuation Map Estimation for Multi-pinhole Clinical SPECT

Chen, Y.

DOI
10.4233/uuid:49102b45-50fc-4d17-a38b-eb9de43f6c1e

Publication date
2021

Document Version
Final published version

Citation (APA)
Chen, Y. (2021). *Image Acquisition and Attenuation Map Estimation for Multi-pinhole Clinical SPECT*. https://doi.org/10.4233/uuid:49102b45-50fc-4d17-a38b-eb9de43f6c1e

Image Acquisition and Attenuation Map Estimation for Multi-pinhole Clinical SPECT

Yuan Chen

Image Acquisition and Attenuation Map Estimation for Multi-pinhole Clinical SPECT

Dissertation

for the purpose of obtaining the degree of doctor

at Delft University of Technology

by the authority of the Rector Magnificus, prof.dr.ir. T.H.J.J. van der Hagen,

Chair of the Board for Doctorates

to be defended publicly on

Tuesday 13 July 2021 at 15:00 o'clock

by

Yuan CHEN

Master of Science in Applied Physics,
Delft University of Technology, the Netherlands
born in Xiangtan, China

This dissertation has been approved by the promotors.

Composition of the doctoral committee:

Rector Magnificus,	chairperson
Prof.dr. F. J. Beekman	Delft University of Technology, promotor
Dr.ir. M. C. Goorden	Delft University of Technology, copromotor
Independent members:	
Prof.dr. G. T. Gullberg	University of California San Francisco, USA
Prof.dr. M. A. King	Umass Medical School, USA
Prof.dr. F. A. Verburg	Erasmus Medical Center
Prof.dr. W. J. Niessen	Delft University of Technology/ Erasmus Medical Center
Prof.dr. H. T. Wolterbeek	Delft University of Technology, reserve member

The research leading to this thesis is conducted with financial support of the Netherlands Organization for Scientific Research (NWO), Physics Valorization Prize 2015 'Ultra-fast, ultra-sensitive and ultra-high resolution SPECT' co-financed by MILabs B.V.

Keywords: brain SPECT, pinhole collimation, DaTscan, sufficient sampling, convolutional neural network, Monte Carlo simulation

Printed by: Gildeprint – Enschede

Cover design: Yuan Chen

ISBN 978-94-6384-232-7

An electronic version of this dissertation is available at https://repository.tudelft.nl

Contents

Summary

Single-photon emission computed tomography (SPECT) is a well-established nuclear imaging modality for studying functional and pathological properties of the brain. Conventional general purpose SPECT systems typically offer a spatial resolution of about 10 mm with a sensitivity of 0.01-0.02%. A few dedicated brain SPECT scanners have been proposed, but resolutions and sensitivities are no better than 7 mm and 0.03% respectively, and some of these scanners are not manufactured anymore. This limited resolution hampers detection of localized brain abnormalities, while the low sensitivity requires a long scanning time that limits fast dynamic studies. Besides a compromised resolution and sensitivity, conventional SPECT systems require rotation of heavy detectors to obtain sufficient angular projections, which hamper fast dynamic imaging.

To cope with several limitations of conventional SPECT, a prototype clinical system dubbed G-SPECT-I was launched by MIlabs BV (Utrecht, the Netherlands). It is based on the use of a stationary combination of an exchangeable multiple-pinhole collimator and nine large field-of-view detectors. For objects the size of a human head, G-SPECT-I achieved an unprecedented reconstructed resolution down to 2.5 mm with a 0.042% peak sensitivity and a reconstructed resolution of 3.5 mm with a 0.090% peak sensitivity, when using collimators with an inner diameter of $\sim$ 38 cm and a respective pinhole diameter of 3.0 and 4.5 mm.

Due to its stationary detector geometry, rotation of heavy detectors (hundreds of kilos) and collimators is not required for G-SPECT-I, which can be an advantage for fast dynamic imaging. G-SPECT-I employs a geometry in which all pinholes are simultaneously viewing a central volume. This focusing geometry results in a central region that is subject to complete sampling and therefore can be imaged in a fully stationary mode. To expand the volume that is sampled sufficiently, the patient bed is translated during imaging. Thus, G-SPECT-I offers the flexibility of performing fully stationary confined-region scans while also allowing for extended volume scans in which only the bed needs to be translated. For brain scanning with G-SPECT-I, the overhead time for a bed translation during scanning is currently $\sim$ 1.7 s, meaning that for fast dynamic scans of a larger area or the entire head, a significant fraction of the acquisition time could still be lost. To enable fast dynamic SPECT imaging, image acquisition protocols with a minimized number of bed translations with G-SPECT-I were developed in this thesis.

For brain SPECT, two important applications are dopamine transporter imaging (DaTscan) using the tracer ^{123}I-FP-CIT and brain perfusion imaging using ^{99m}Tc-labelled tracers

(^{99m}Tc-HMPAO or ^{99m}Tc-ECD). The former provides a visualization of dopamine transporters in the brain's striatum for diagnosis of e.g., Parkinson's disease. Perfusion imaging is often applied to the entire brain for assessment of e.g. cerebrovascular diseases or detection of epileptic foci. In this thesis, we developed dedicated optimal bed trajectories for both applications based on simulation studies. Specifically, for DaTscan imaging, we proposed a focused striatum scanning strategy to maximize the striatal count yield while ensuring appropriate sampling for surrounding brain tissue; for full brain perfusion imaging, we confined the scan region to the minimum required and investigated the effect of reduction of the number of bed translations on perfusion image quality. Evaluation of the proposed strategies were performed using corresponding clinical assessment criteria. Results show that G-SPECT-I is able to achieve a focused DaTscan with only 4 bed translations while a full brain perfusion scan can be achieved with only 18 bed translations. As a consequence, the corresponding overhead times for the bed movement are only seconds or half a minute respectively, which facilitates fast dynamic brain imaging using the G-SPECT-I technology.

Apart from optimizing image acquisition, we investigated accurate attenuation map estimation for brain SPECT imaging solely using emission data. In clinical SPECT, attenuation correction can be applied to obtain images that provide quantitative information on the regional activity concentration. This correction generally requires an attenuation map, usually derived from a registered CT scan, that gives the attenuation coefficient at each voxel in the patient. However, such a CT scan is often not available and errors in image registration can induce inaccuracies in the attenuation corrected SPECT images. Alternatively, the scattered photons from the SPECT emission data contain essential information about the tissue attenuation coefficient. In this thesis, we proposed to extract this information using deep learning techniques. To this end, we performed multiple image reconstructions from different energy windows to employ the energy-spatial information of the photons over a broad energy range (primary and scattered). This image set is subsequently used as input to a convolutional neural network (CNN) to generate a SPECT-aligned attenuation map as output. Using Monte Carlo simulations, the proposed CNN method was validated for full brain perfusion imaging and for focused DaTscan imaging with G-SPECT-I. Different CNN architectures were investigated for an optimal application on the focused DaTscans. Results show that CNNs can be employed to estimate accurate attenuation maps using SPECT data only, which could allow for attenuation correction to be independent of data from other imaging modalities.

Although the proposed strategies presented in this thesis show promising results, the studies were solely based on simulations. Future validation using patient scans is essential to bring the developed methods closer to clinical applicability.

Samenvatting

Single-photon emission computed tomography (SPECT) is een veel gebruikte nucleaire beeldvormende methode voor het bestuderen van functionele en pathologische eigenschappen van de hersenen. Conventionele SPECT systemen voor algemene doeleinden hebben doorgaans een ruimtelijke resolutie van ongeveer 10 mm met een gevoeligheid van 0.01-0.02%. Er zijn enkele specifieke SPECT scanners voor hersenen ontwikkeld, maar resoluties en gevoeligheden zijn niet beter dan respectievelijk 7 mm en 0.03%, en sommige van deze scanners worden niet meer geproduceerd. Deze beperkte resolutie belemmert de detectie van gelokaliseerde hersenafwijkingen, terwijl de lage gevoeligheid een lange scantijd vereist, wat resulteert in een verhoogd risico op bewegingsartefacten en grenzen aan snelle dynamische studies. Naast een matige resolutie en gevoeligheid, vereisen conventionele SPECT systemen rotatie van zware detectoren om voldoende hoekprojecties te verkrijgen, wat een snelle dynamische beeldvorming belemmert.

Om het hoofd te bieden aan verschillende beperkingen van conventionele SPECT, werd een prototype klinisch systeem genaamd G-SPECT-I gelanceerd door MIlabs BV (Utrecht, Nederland). Het is gebaseerd op het gebruik van een stationaire combinatie van een verwisselbare collimator met meerdere pinholes en negen grote detectoren. Voor objecten ter grootte van een menselijk hoofd behaalde G-SPECT-I een ongekende gereconstrueerde resolutie tot 2.5 mm met een piekgevoeligheid van 0.042% en een gereconstrueerde resolutie van 3.5 mm met een piekgevoeligheid van 0.090% bij gebruik van collimatoren met een binnendiameter van $\sim$ 38 cm en pinhole-diameters van respectievelijk 3.0 en 4.5 mm.

Vanwege de stationaire detectorgeometrie is rotatie van zware detectoren (honderden kilo's) en collimatoren niet vereist voor G-SPECT-I, wat een voordeel kan zijn voor snelle dynamische beeldvorming. G-SPECT-I maakt gebruik van een geometrie waarin alle pinholes tegelijkertijd een centraal volume bekijken. Deze focusseergeometrie resulteert in een centraal gebied met volledige bemonstering en kan daarom worden afgebeeld in een volledig stationaire modus. Om het volume dat voldoende wordt bemonsterd uit te breiden, wordt het patiëntbed tijdens beeldvorming getransleerd. G-SPECT-I biedt daarmee de flexibiliteit om volledig stationaire scans van beperkte gebieden uit te voeren, terwijl ook uitgebreide volumescans mogelijk zijn waarbij alleen het bed hoeft te worden getransleerd. Voor hersenscans met G-SPECT-I is de overheadtijd voor een bedtranslatie tijdens het scannen momenteel $\sim$ 1.7 s, wat betekent dat voor snelle dynamische scans van een groter gebied of het hele hoofd, een aanzienlijk deel van de acquisitietijd nog

steeds verloren zou kunnen gaan. Om snelle dynamische SPECT beeldvorming mogelijk te maken, werden in dit proefschrift beeldacquisitieprotocollen ontwikkeld met een minimaal aantal bedtranslaties met G-SPECT-I.

Voor hersen SPECT zijn twee belangrijke toepassingen dopamine transporter beeldvorming (DaTscan) met behulp van de tracer ^{123}I-FP-CIT en beeldvorming van de hersenperfusie met behulp van ^{99m}Tc-gelabelde tracers (^{99m}Tc-HMPAO of ^{99m}Tc-ECD). De eerste geeft een visualisatie van dopamine transporters in het striatum van de hersenen voor de diagnose van bijvoorbeeld de ziekte van Parkinson. Perfusiebeeldvorming wordt vaak toegepast op de gehele hersenen voor beoordeling van b.v. cerebrovasculaire ziekten of detectie van epileptische haarden. In dit proefschrift hebben we optimale bedtrajecten speciaal ontwikkeld voor beide toepassingen op basis van simulatiestudies. Specifiek, voor DaTscan beeldvorming, hebben we een gefocuste striatum scanstrategie voorgesteld om de telopbrengst van het striatum te maximaliseren en tegelijkertijd de juiste bemonstering voor omringend hersenweefsel te garanderen; voor beeldvorming van de perfusie van de volledige hersenen hebben we het scangebied tot het minimum vereiste beperkt en het effect van reductievan het aantal bedtranslaties op de beeldkwaliteit van de perfusie onderzocht. Evaluatie van de voorgestelde strategieën werd uitgevoerd met behulp van toepasselijke klinische beoordelingscriteria. De resultaten tonen aan dat G-SPECT-I in staat is om een gerichte DaTscan te bereiken met slechts 4 bedtranslaties en een volledige hersenperfusiescan kan worden bereikt met slechts 18 bedtranbslateis. Als gevolg hiervan zijn de bijbehorende overheadtijden voor de bedtranslaties respectievelijk slechts seconden of een halve minuut, wat snelle dynamische beeldvorming van de hersenen mogelijk maakt met behulp van de G-SPECT-I technologie.

Afgezien van het optimaliseren van de beeldacquisitie, hebben we een nauwkeurige schatting van de verzwakkingskaart voor hersen SPECT beeldvorming onderzocht, alleen op basis van emissiegegevens. In klinische SPECT kan verzwakkingscorrectie worden toegepast om beelden te verkrijgen die kwantitatieve informatie verschaffen over de regionale activiteits concentratie. Deze correctie vereist in het algemeen een verzwakkingskaart, meestal afgeleid van een geregistreerde CT scan, die de verzwakkingscoëfficiënt bij elke voxel in de patiënt geeft. Een dergelijke CT scan is echter vaak niet beschikbaar en fouten in de beeldregistratie kunnen onnauwkeurigheden veroorzaken in de voor verzwakking gecorrigeerde SPECT beelden. Als alternatief kunnen de verstrooide fotonen van de SPECT tracer essentiële informatie over de weefselverzwakkingscoëfficiënt verschaffen. In dit proefschrift hebben we voorgesteld om deze informatie uit de emissie data te halen met behulp van deep learning technieken. Daartoe hebben we meerdere beeldreconstructies uitgevoerd met verschillende energievensters om de energieruimtelijke informatie van de fotonen over een breed energiebereik (primair en verstrooid) te gebruiken. Deze beeldsets worden vervolgens gebruikt als invoer voor een convolutioneel neuraal netwerk (CNN) om een met SPECT uitgelijnde verzwakkingskaart als uitvoer te genereren. Met behulp van Monte Carlo simulaties werd de voorgestelde CNN methode

gevalideerd voor beeldvorming van de volledige hersenperfusie en voor gefocuste DaTscan beeldvorming met G-SPECT-I. Verschillende CNN architecturen werden onderzocht voor een optimale toepassing op de gefocuste DaTscans. Resultaten tonen aan dat CNN's kunnen worden gebruikt om nauwkeurige verzwakkingskaarten te schatten met alleen SPECT gegevens, waardoor verzwakkingscorrectie onafhankelijk kan zijn van gegevens van andere beeldvormingsmodaliteiten.

Hoewel de voorgestelde strategieën in dit proefschrift veelbelovende resultaten laten zien, waren de studies uitsluitend gebaseerd op simulaties. Toekomstige validatie met behulp van patiëntenscans is essentieel om de ontwikkelde methoden dichter bij klinische toepasbaarheid te brengen.

1

Introduction

1.1. Radionuclide imaging

1.1.1. SPECT and PET

Single-photon emission computed tomography (SPECT) is one of the major clinical radionuclide imaging techniques for studying e.g. cardiac, liver, thyroid, bone and brain abnormalities. In SPECT, radiolabelled molecules ("tracers") are injected into the body and subsequently accumulate at specific tissues. SPECT systems estimate the 3D distribution of the tracer by detecting gamma photons emitted by the tracer leaving the patient, and the resulting SPECT images that can be displayed on a screen give insights into functional and pathological properties of the tissue.

SPECT has often been compared with PET, another important nuclear imaging technique. A major difference between SPECT and PET lies in the nature of the radioactive decay of their tracers: a SPECT tracer decays by emitting single gamma photons with a typical energy of 75-360 keV, while decay of a PET tracer results in the emission of pairs of annihilation photons with a fixed energy of 511 keV (for all positron emitters). Thus, SPECT permits simultaneous imaging of multiple tracers by separating them based on their photon emission energies. This is not possible with PET as annihilation photons from different PET tracers are indistinguishable by energy. Furthermore, SPECT tracers often apply long living radionuclides that allow for long-distance transportation from production site to hospital while PET tracers are usually more short-lived requiring tracers to be produced close to clinical facilities. Besides, different gamma photon collimation principles are used in clinical SPECT and PET: SPECT relies on mechanical collimation to

obtain directional information of the detected gamma photons while clinical PET is commonly based on electronic collimation, meaning that the direction of the two annihilation photons detected in coincidence is assumed to be given by the line joining the two detected locations. The different collimation techniques lead to a difference in resolution and sensitivity of clinical conventional SPECT systems (about 8-10 mm and 0.01-0.02% respectively) and PET systems (about 4 mm and 1% respectively). Additionally, the use of different techniques result in a significant difference in costs; SPECT is generally much more cost-efficient than PET (scanners are typically 4 times cheaper [1, 2]). Generally, SPECT and PET are highly complementary technologies that have overlapping but unique applications. The choice of either modality largely depends on the clinical task as well as the availability of systems and tracers. Currently, about 75% of the clinical nuclear imaging procedures are performed with SPECT [3]. Worldwide, about 40 million SPECT scans are annually performed, while in the Netherlands, around 250,000 SPECT examinations are conducted each year [4]. In this thesis, we focus on clinical SPECT imaging for assessment of brain abnormities based on a newly developed prototype SPECT system.

1.1.2. SPECT application for brain imaging

Two important applications of brain SPECT are DaTscans using ^{123}I-FP-CIT (159 keV) as a tracer and brain perfusion scans with ^{99m}Tc-labelled tracers (^{99m}Tc-HMPAO or ^{99m}Tc-ECD at 140 keV).

DaTscans provide visualization of the dopamine transporter (DaT) density in the brain (Fig 1.1). Dopamine is a neurotransmitter found in the brain's striatum that regulates activities such as movement and emotion. Therefore, a DaTscan is useful in evaluation of patients with suspected parkinsonian syndromes (a group of diseases sharing similar symptoms of slow movement, resting tremor and trouble walking). For patients with Parkinson's disease (PD), dementia with Lewy body, or other parkinsonian syndromes due to neurodegeneration, an abnormal DaTscan with a reduced DaT density is observed. An illustration of the shape and location of the striatum as well as several clinical DaTscans are given in figure 1.1 (a-b).

Brain perfusion scans image regional cerebral perfusion (see Fig. 1.1c-d). As cerebral blood flow is closely linked to neuronal activity, and thus the perfusion distribution can indirectly reflect the cerebral metabolism level in different areas of the brain. A hyperperfusion pattern can be related to an increased neuronal activity (e.g. in epilepsy) while hypo-perfusion might be associated with impaired cerebral function. SPECT is the only imaging modality that is capable of an ictal perfusion scan in routine clinical settings for epileptic foci detection. This is accomplished by the rapid injection of the ^{99m}Tc-labelled tracer (^{99m}Tc-HMPAO or ^{99m}Tc-ECD) at the time of seizure onset. The tracer is trapped in the tissue compartment and does not change its relative distribution over time, which allows a SPECT scan several hours after the injection when the patient is sedated. Be-

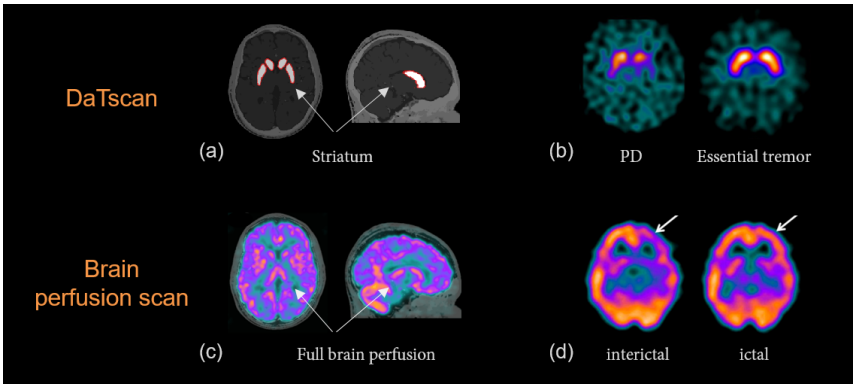

Figure 1.1: Examples of DaTscans and brain perfusion scans. (a) Illustration of the shape and location of the striatum (target structure for a DaTscan); the tracer ^{123}I-FP-CIT binds selectively to the striatum with high affinity. (b) Examples of a DaTscan obtained from a patient with Parkinson's disease and from a patient with essential tremor; note that Parkinson's disease and essential tremor have overlapping clinical symptoms and are difficult to distinguish based on clinical examinations only. (c) Illustration of a normal brain perfusion scan with a tracer distribution over the entire brain; (d) examples of an interictal and an ictal SPECT scan; epileptic foci can be detected by subtracting the interictal scan from the ictal scan. Examples in (b) and (d) are adapted from [5, 6] with permission.

sides, brain perfusion scans can aid in medical cases for assessment of cerebrovascular diseases, differential diagnosis of dementia, evaluation of brain traumatic injury and brain death, etc.

1.2. SPECT systems

1.2.1. Gamma detectors and collimators

SPECT systems consist of gamma detectors and collimators. The detectors are mainly based on NaI scintillators (a crystal that converts high-energy gamma photons into visible light photons) and photomultiplier tubes (PMTs, which absorb light photons and generate electric signals with amplitude ideally proportional to the number of light photons that reach the tube). For each incoming gamma photon that hits the detector, position and energy are estimated by the position and the intensity of the electric pulses of the array of PMTs. The typical intrinsic spatial resolution of the detector is 3-4 mm due to the uncertainty of light collection and the light conversion process. The energy resolution of the detector is around 10% for photons with an energy of 140 keV that are emitted by ^{99m}Tc (the most commonly used SPECT isotope).

Between the detector and the patient, a collimator is placed. Collimators are made of dense materials with high stopping power (e.g. lead or tungsten) to reduce penetration of high energy photons. Only gamma photons coming from certain directions can pass the collimator and reach the detector. This way of selective blocking provides directional

information on the detected gamma photons. Such information is necessary for later retrieval of the 3D tracer distribution.

Several types of collimators have been proposed, and a few of them are illustrated in figure 2. The parallel-hole collimator is one of the most important and currently the most widely used collimator in clinical practice. The pinhole collimator is another important collimator used in some clinical systems and is now widely applied in preclinical SPECT for animal imaging. Converging and diverging hole collimators are used in a few clinical systems. Converging hole collimators can be further categorized into fan-beam and cone-beam collimators. In the latter cone-beam case, the holes are tilted both in the transaxial plane and in the axial direction. The parallel-hole and pinhole collimator are explained in detail in the following text as they are most relevant for this thesis.

A parallel-hole collimator typically has a honeycomb structure, with each cell being a long and narrow hole (see Fig. 1.2). Ideally at each detector pixel, only the accumulated photons coming along a common single direction perpendicular to the detector surface are recorded. In practice, each hole has a finite width and length, and thus photons coming from a direction slightly deviating from the perpendicular view are also detected (see Fig. 1.2). Wider and shorter holes permit more photons to pass and thus increase count yield (higher sensitivity), however at the cost of a degraded spatial definition (lower collimator resolution). A conventional parallel-hole general purpose system has a system resolution (a combined detector and collimator resolution) of about 10 mm.

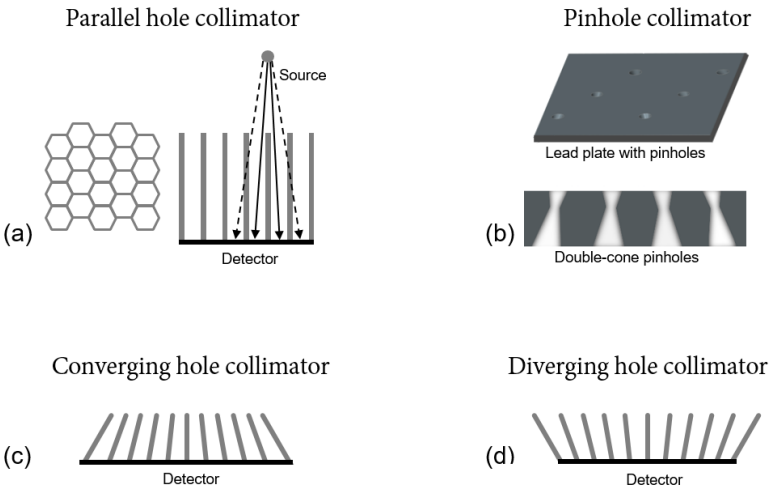

Figure 1.2: Illustration of (a) parallel-hole collimator, (b) pinhole collimator, (c) converging and (d) diverging hole collimator.

A pinhole collimator is made of a large plate or a cylinder with one or multiple holes in it (typically having a double cone shape, see Fig. 1.2). The pinhole permits an object to be projected onto the detector with a magnification factor if the object-pinhole distance l is smaller than the pinhole-detector distance z. Thus, for objects smaller than the detector

surface area, the crystal detector can be efficiently used (see also Fig. 1.3). Due to the magnification, the effect of detector resolution is reduced by a factor of z/l, while the collimator resolution becomes $D(z+l)/z$ where D is the pinhole diameter. By employing a large number of pinholes and focusing them on the same region, a high sensitivity can be obtained within the focal region of the pinholes.

Our group initially developed various multi-pinhole SPECT systems for preclinical purposes that are nowadays in use by hundreds of researchers worldwide. Excellent resolutions of down to 0.12 mm and 0.25 mm for ex-vivo and in-vivo mice imaging were achieved respectively [7, 8]. For clinical SPECT, multi-pinhole collimation systems are mostly under investigation in research studies. A detailed overview is given in a recent paper [9]. Currently, few multi-pinhole clinical scanners are on the market (one example is the Discovery NM530c for cardiac SPECT). Recently, a prototype multi-pinhole system launched by MIlabs BV (the Netherlands) has demonstrated a resolution of 2.5 mm in physical phantom studies [10].

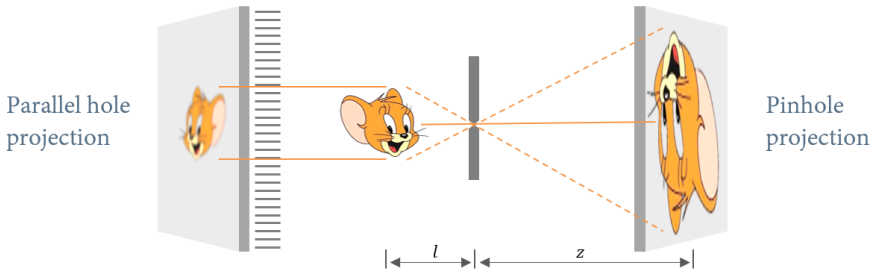

Figure 1.3: Projections using a parallel-hole collimator and a pinhole collimator. With parallel-hole collimation, projections are blurred with a detector intrinsic resolution R_i. In contrast, projections can be magnified on the detector with pinhole collimation, which results in an equivalent detector resolution of $R_i(l/z)$. Here l is the object-pinhole distance and z is the pinhole-detector distance.

1.2.2. Sampling completeness

To retrieve the 3D tracer distribution, multiple 2D projections on the detectors acquired from different angles are needed for sufficient sampling. The sampling conditions for SPECT imaging can in practice be categorized into i) angular sampling in the transaxial plane (xy plane) and ii) axial sampling (z direction).

Angular sampling completeness demands that every part of the object should have projections acquired from an orbit covering at least 180 degrees at sufficiently small angular intervals. If part of the objects fails to have these projections, 'projection truncation' happens which might result in artefacts in the estimated 3D tracer distribution. Angular sampling sufficiency can be achieved by rotating the detector-collimator (gantry) around the patient. Current clinical SPECT systems with dual-head parallel-hole configurations (the most prevalent) are mostly rotation-based. To obtain a total of 120 views (as generally

recommended), 60 detector positions are needed for a dual-head scanner. Meanwhile, the overhead time associated with rotation of heavy detectors (hundreds of kilos) could be minutes, which hampers fast dynamic capabilities. Alternatively, stationary systems that have multiple pinhole-collimated detectors mounted in a ring have been proposed in several research groups [10–13]. Such a ring-based system could allow acquiring projections from different directions simultaneously without any rotation of the heavy detectors, while a high sensitivity can be achieved with the use of multiple detectors.

For parallel-hole systems, holes in each collimator are directed towards a common direction that is parallel to the transaxial plane (see Fig. 1.3). Axial sampling sufficiency is obtained by scanning at different stops along the axial direction in a "step-and-shoot" mode. For multi-pinhole systems, not all projection views are parallel to the transaxial plane (as indicated by the dashed orange lines in Fig. 1.3). In principle, sampling completeness is only achieved for the central plane (as illustrated by the solid orange line in Fig. 1.3). Practical ways to extend the region with sufficient axial sampling are using multiple rings of pinholes and/or scanning at different stops along a spiral trajectory or a multi-planar trajectory [14].

1.2.3. Multi-pinhole stationary G-SPECT-I system

Nowadays, clinical SPECT is mostly performed with dual-head parallel-hole systems. Due to the limited resolution and sensitivity of these systems (about 8-10 mm and 0.01-0.02% respectively), attempts to improve the performance have been made, including the development of triple-head fan beam systems (e.g. GCA-9300A and Prism 3000XP). While for these systems the sensitivity was increased to around 0.03%, the resolution was only slightly improved to about 7 mm, and these systems are available from a limited number of vendors. Besides, a few SPECT systems dedicated for cardiac or brain imaging were built. In dedicated cardiac systems (e.g. D-SPECT and Discovery NM 530c), detectors are arranged in such a way that a high sensitivity (0.06-0.1%) is obtained in the heart region while resolution is not much improved (about 10 mm). Particularly, Discovery NM 530c is a multi-pinhole stationary system that does not require detector movement. For dedicated brain SPECT, scanners were constructed by using either sophisticated detectors (e.g. Mediso X-Ring/4R), or a large number of focusing collimators and detectors (e.g. NeuroFocus and inSpira HD with a resolution of about 7 mm). However, only few clinical validations are available with the dedicated brain systems and some are not manufactured anymore.

SPECT systems with multi-pinhole collimators have demonstrated enhanced resolution and detection sensitivity especially when imaging small objects. Simulation studies were carried out in several groups to optimize a multi-pinhole system geometry for clinical purposes. Lately, a multi-pinhole prototype clinical G-SPECT-I system was launched by MIlabs BV (Utrecht, the Netherlands). A few phantom scans have been performed, which

demonstrated a superior resolution of G-SPECT-I down to 2.5 mm and a peak sensitivity of 0.042%. The superior resolution and sensitivity of G-SPECT-I is facilitated by the use of a stationary combination of multi-pinhole collimators and nine large field-of-view detectors. Owing to this stationary detector geometry, rotation of heavy detectors and collimators is not needed, which can be an advantage of G-SPECT-I for fast dynamic imaging. Additionally, while conventional parallel-hole collimators were designed for imaging isotopes emitting gammas with a typical energy of around 140 keV, G-SPECT-I permits imaging isotopes with medium- and high-energy photons due to the better penetration characteristics with pinholes. A high resolution of 4.5 mm was obtained when imaging isotopes emitting gamma photons at 511 keV energy (MIlabs G-SPECT brochure, www.milabs.com). Hence, G-SPECT-I might be a unique platform that permits simultaneous imaging of multiple diagnostic and therapeutic isotopes (i.e., α and β emitters that co-emit high-energy gammas e.g. ^{213}Bi with 440 keV gammas) over a broad energy range.

An illustration of the G-SPECT-I configuration is given in Fig. 1.4. The G-SPECT-I system consists of nine gamma detectors applying NaI(Tl) scintillators (the most widely used detector for clinical SPECT). Each detector has a large size of $595 \times 472 \times 9.5$ mm^3. The multi-pinhole collimator is interchangeable (as shown in Fig. 1.4). In this thesis, collimators that have a bore diameter of around 38 cm which are very suitable for brain, selected extremity or pediatric imaging were used. These collimators are termed brain collimators in this thesis. Other collimators having a larger bore size have also been designed and built for body SPECT scans with G-SPECT-I (e.g. for cardiac imaging).

With the brain collimators, the influence of intrinsic detector resolution (3.5 mm) is diminished by using a pinhole-detector distance (542 mm) that is larger than the object-pinhole distance (215 mm). All pinholes are focusing on a central volume. Within this central volume, projections over 360° are acquired (meaning that sufficient sampling is ensured) and a high sensitivity is obtained. This region is thus called the complete data volume (CDV, see Fig. 1.4). Imaging of an object covered by the CDV can thus be performed in a fully stationary mode enabling sub-second time resolution. The transaxial diameter R_c and axial length L_c of the CDV are 100 mm and 60 mm respectively. For a scan of an object larger than the CDV, the bed is translated to position different parts of the object in the CDV for sufficient sampling of the entire object. This bed translation is facilitated by a precisely controlled xyz stage. In this way, G-SPECT-I also allows for extended volume scans in which only the bed needs to be translated.

Employing a large number of bed translations with small steps to make sure every part of the object is at least once positioned in the CDV would warrant sufficient sampling. This however comes at the cost of an increased overhead time needed for bed movement (around 1.7 seconds per bed translation). For fast scans or multi-frame dynamic studies (e.g. with half-minute time frames), a significant fraction of acquisition time could be lost, which leads to a reduced number of detected counts and a compromised effective sensitivity. For this reason, optimizing the bed translation trajectory with a limited number

of bed movement is one of the topics of this thesis.

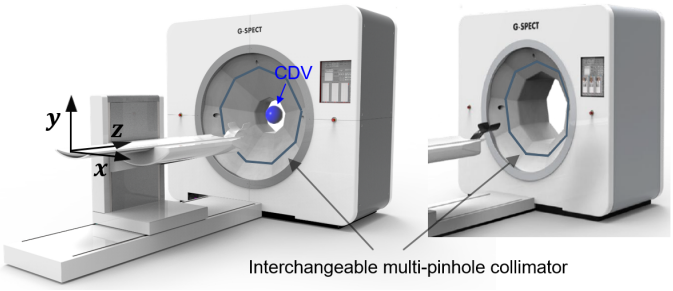

Figure 1.4: G-SPECT-I system; the left image shows the brain collimator, and the right image shows the body collimator.

1.2.4. Simulation and image reconstruction

1.2.5. Physics in photon transport

A gamma photon emitted by a tracer might interact with human tissue, with the collimator and with the detector before being detected. In clinical SPECT, two main photon interactions are relevant. The first one is the photoelectric effect which takes place primarily in heavy metal materials (e.g. collimator and detector). The consequence of the photoelectric effect is photon absorption with a resulting loss in the number of gamma photons being detected. The second relevant interaction is Compton scatter which is the dominating interaction in soft tissue (accounting for over 95% of the total interactions for 140 keV photons). In the case of Compton scatter, photons are deflected and lose part of their energy. This leads to a broad energy spectrum of the detected gamma photons even when imaging isotopes that emit gammas at a single energy. The cross section of Compton scatter is proportional to the density of a substance.

Ideally, one would hope that the primary photons emitted from the tracer can be captured entirely and exclusively (i.e., free of scattered photons) for estimating the tracer distribution. Differentiation of the primary photons from the scattered ones can be done based on the photon energy. However due to energy uncertainty associated with the intrinsic detector energy resolution, an energy window centred at the photo-peak energy is used to maximally include the primary photons while excluding the scattered photons (e.g. a window width of 20% at 140 keV for ^{99m}Tc). Even so, scattered photons still make up a non-negligible contribution of the total number of counts within the photo-peak window (30%-40% in most clinical cases [15]). As a result, scatter artefacts arise which are characterized by a reduced contrast in the estimated tracer distribution. Apart from scatter artefacts, the loss of primary photons due to photon scattering and photon absorption leads to attenuation artefacts. As a typical example of attenuation artefacts, a uniform activity distribution would show a decreased intensity in the image especially

at the central part of the object. Besides leading to a degraded image quality, accurate quantification of the underlying tracer distribution is prohibited when corrections for scatter and attenuation are not applied.

Currently, scatter correction is commonly done using the triple energy window (TEW) subtraction method [16]. The TEW uses two narrow windows at each side of the photopeak to estimate the fraction of scattered counts in the photopeak window. These scattered counts are then taken into account in a later step when retrieving the tracer distribution, e.g. via a subtraction from the total number of counts in the photopeak window to obtain a scatter-corrected projection. While TEW is a simple and effective method that has been widely used for scatter correction, accurate attenuation correction is challenging for clinical SPECT. Attenuation correction generally requires an attenuation map that provides the tissue attenuation coefficient at each voxel in the patient. Ideally, an attenuation map is derived from a registered CT scan. However, such a CT is often not available, and errors in image registration can induce inaccuracies in SPECT images. Besides the CT based approach, manually drawing an ellipse around the head contour and assuming uniform attenuation within the ellipse is widely used for attenuation map approximation. This ellipse method, however, could suffer from observer subjectivity and insufficient estimation of the head contour and internal head anatomy.

1.2.6. Simulations

Simulations are done in this thesis to generate projections via a computer program instead of physically acquiring them from the actual G-SPECT-I scanner. Simulations are commonly performed for optimization of the system design and acquisition protocols, or for the generation of projections assuming a certain system geometry. In simulations, assumptions of the tracer distribution in a patient are made based on earlier clinical observations. For the given tracer distribution, the projections are then obtained by modelling the SPECT system as well as the photon interactions within the system and patient.

Two types of simulations with different modelling approaches were conducted in this thesis. The first type of simulation generates projections based on a voxelized ray tracing (VRT) simulator [17]. This simulation is therefore termed VRT in this thesis. VRT tracks the paths from the gamma source to the detector and calculates the attenuation of gamma photons along these paths. In this way, attenuation is modelled but scatter is ignored. Such scatter-free simulated projections are generally considered acceptable for the purpose of system or image acquisition optimization, as scattered photons can be partially corrected for with a TEW method on the projections. Meanwhile, because of the simplification of ignoring scatter effects, computation time can be greatly reduced which makes VRT an efficient simulation tool. For the research described in this thesis, a full simulation of a subject scan can be done within 1-2 hours when the modelling of the SPECT system is pre-calculated (which is generally the case as this modelling only

needs to be done once per SPECT system). Additionally, VRT allows generation of noiseless projections, which is desirable for visualization and quantification of some artefacts that would otherwise be hidden beneath the noise. In this thesis, VRT is used to optimize acquisition protocols by performing multiple noiseless simulations assuming different settings, which is not feasible with physical scanning.

The second approach is Monte Carlo (MC) simulation. MC simulation is a stochastic method that estimates a solution to the problem of interest using random numbers and statistical sampling. For individual particles emitted from the source, at each stage of the particle's life, there is a probability distribution for the possible types of interaction between particle and matter to occur, as well as for the distance it travels before a next collision and the energy and angle after a collision. By randomly sampling the probability distributions, the outcome at each step of the particle's life is determined. MC simulation is computationally expensive and generally requires a large cluster with parallel computing and then still takes a long time (several days in our applications). The advantage of MC simulation is the capability of accurately representing the real photon transport by fully modelling particle interactions and their cross-sections. In this thesis, MC simulation is performed to generate 'realistic' SPECT projections, as G-SPECT-I is not yet certified for patient scanning.

1.2.7. Reconstruction algorithms

The process of estimating the 3D distribution of the radioactivity from a set of 2D projections is called image reconstruction. For SPECT reconstruction with multi-pinhole geometries, iterative algorithms, e.g. maximum likelihood expectation maximization (MLEM), are often used due to their flexibility to handle complex geometries. For MLEM, an initial estimation of the activity distribution (e.g. a uniform cylindrical distribution) is assumed. This estimation is subsequently updated in each iteration. For an estimated activity distribution, the noiseless projection can be modelled by

$$P = MA. \tag{1.1}$$

Here A is a vector of voxels representing the 3D activity distribution in object space, P is a vector representing the number of gamma photons detected in each pixel, and M is the system matrix. An element M_{ij} of this matrix gives the probability of a photon emitted at voxel j to be detected in pixel i in P. In principle, all physical effects of photon transport can be modelled in the system matrix. In practice, an approximation of the system matrix is often made by neglecting photon scatter and absorption within the patient. This approximation was made for all system matrices used for image reconstruction in this thesis. In such cases, the system matrix depends only on the system, e.g. the geometry and resolution of the collimators and detectors. This system matrix can be pre-calculated

(e.g. with a VRT simulator) and only needs to be computed once per system.

In this thesis, we used an accelerated version of MLEM for image reconstruction, which is called similarity-regulated ordered subset expectation maximization (SR-OSEM) [18]. With OSEM based approaches, a subset of the projection data is used for each update instead of the full data as in MLEM. For standard OSEM, one needs to pre-determine the number of subsets; a too large number of subsets results in undesirable noise levels or even erasure of lesions in low-activity regions while a small number of subsets leads to long reconstruction times. SR-OSEM is an improved version of OSEM that automatically and locally determines the number of subsets by checking a similarity criterion of different update factors, and thus it is a safe and efficient reconstruction algorithm.

1.3. Convolutional neural networks (CNNs)

Artificial neural networks (ANNs) have become one of the most famous machine learning models since their first introduction in the 1940s. An artificial neural network consists of a number of elements, called neurons, most times organized in layers. An input layer contains the user defined variables or inputs to the network. An output layer produces the predictions of the network. In between, there are one or more hidden layers (see figure 1.5).

For supervised learning, ANNs allows to nonlinearly transform an input to an output based on information learned from example input-output pairs. To establish such a transformation, neurons in each layer are connected to those in the next layer with weight parameters w. As in the example of figure 1.5, the network starts with an input layer. The i'th neuron of this layer has a value x_i (defined by users). Then, to obtain a value for the j'th neuron in the next layer (i.e., the first hidden layer), each value in the input layer is multiplied by a weight, and the sum of all weighted inputs $\sum w_{ij}x_i$ is added with a bias term b_j, i.e., $\sum w_{ij}x_i + b_j$ (see Fig. 1.5). The resulting value subsequently goes through an activation function f. The output of the activation function determines the value Z_j (the final output of the j'th neuron in the hidden layer). The Z_j further serves as an input for neurons in the next layer. In this way, the information is propagated towards the output layer. The activation function (generally non-linear) is involved to increase the expression capability of the network as it allows for complex mapping.

Initially, parameters of the networks (weights and bias) are set in a random manner. Optimization of the parameters of the network is achieved via a training procedure. Training is performed based on a dataset consisting of pairs of input data and the corresponding ground truth (see figure 1.6). Given the input, the network is trained by minimizing the difference between the network predictions and the assigned ground truth. This difference is defined by a loss function. Commonly used loss functions are mean square error and cross-energy for regression tasks (continuous output values) and classification tasks

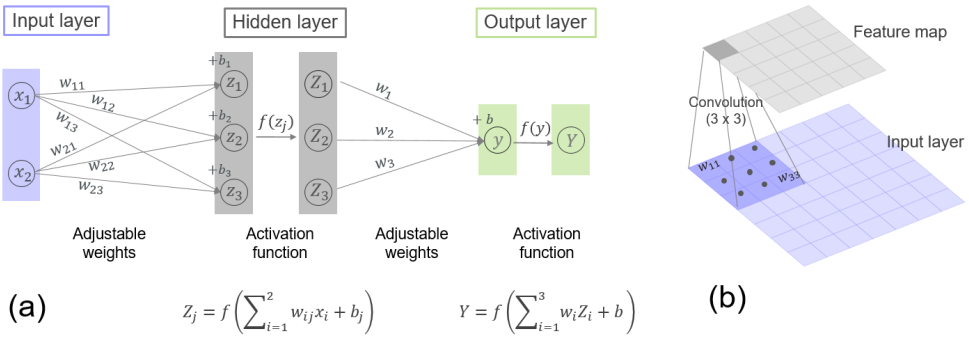

Figure 1.5: Illustration of (a) a traditional ANN and (b) a convolution operation of a CNN architecture. Traditional ANN consist of fully connected layers meaning that all neurons of one layer are connected to those in the next. In CNN, the same convolutional kernel 'scans' across the entire input to produce a feature map.

(discrete output values) respectively. When training is completed, the weights of the network can be saved. This allows the network to give a prediction for incoming new input data.

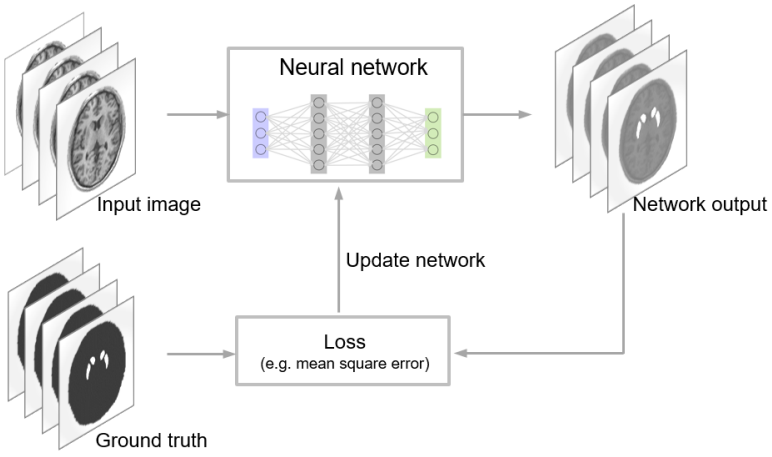

Figure 1.6: Illustration of a neural network for image segmentation. Generally, a large number of pairs of input (MR images) and ground truth segmentation are used for training. Parameters of the network is optimized such that the difference between the network output and the ground truth (defined as the loss) is minimized. When training is finished, the network can be used to predict an output image given a new brain MR image as input.

Traditional ANNs use fully connected layers that connect all neurons of one layer to those in the next. This is extremely inefficient and makes the algorithm computationally expensive especially when dealing with 2D or 3D image data. A convolutional neural network is an ANN with advanced architecture specifically designed and well suited for image-related tasks. CNNs are currently widely used in medical image analysis for image restoration [19], tissue segmentation [20], image transformation (e.g. MR to CT) [21], lesion detection [22], etc. In nuclide imaging with SPECT and PET, CNNs have been inves-

tigated for attenuation map estimation [23], attenuation correction [24], image denoising [25] and motion correction [26].

In a CNN, neurons in one layer do not connect to all the neurons in the next layer. Instead, each set of neurons sees only a small region of the previous layer via a convolution operation (as shown in Fig. 1.5). Besides, the exact same convolutional kernel 'scans' across the entire input to produce a so-called feature map. This 'weights-sharing' scheme drastically reduces the number of parameters needed to be learned while the spatial relationship in data is preserved. The convolution procedure is repeated by using multiple kernels to generate several feature maps with each representing a certain characteristic of the input.

A CNN typically consists of multiple convolutional layers, activation layers and pooling layers. Currently, the most widely used activation function in CNN is the ReLU function, which is defined as $\mathrm{ReLU}(z) = \max(0, z)$. The pooling layer performs a down-sampling operation that reduces the dimensionality of the feature maps. A max pooling is commonly used by taking maximum values in a grid region. As only one value is produced for each grid region in the input feature map, this operation introduces a translational invariance to small shifts, and could reduce overfitting with the loss of some data and a decreased model complexity.

1.4. Outline of the thesis

This thesis focuses on image acquisition and attenuation map estimation for a multi-pinhole prototype clinical SPECT system. In Chapter 2 and Chapter 3, image acquisition protocols were optimized to enable fast dynamic capabilities of G-SPECT-I for DaTscans and brain perfusion imaging. Specifically, in Chapter 2, we developed a focused DaTscan imaging strategy for a maximized effective sensitivity while ensuring appropriate sampling. Angular sampling sufficiency with the multi-pinhole G-SPECT-I system was investigated. Multiple VRT simulations were performed for various sampling strategies with the use of different bed trajectories. A trajectory that requires only 4 bed translations was proposed. Such a trajectory entails seconds for bed movement, which may enable fast dynamic DaTscans.

While Chapter 2 aimed for focused striatum imaging with a confined axial scanning length, Chapter 3 is dedicated to optimizing image acquisitions for full brain perfusion scans. Based on the angular sampling condition investigated in Chapter 2, here we studied the axial sampling sufficiency for scanning the full length of the brain. Multiple VRT simulations were performed for various sampling strategies with a reduced number of bed positions. It is demonstrated that full brain perfusion imaging can be performed with G-SPECT-I using a total of 18 bed stops (overhead time of about half a minute), which may bring fast whole brain SPECT into reach for G-SPECT-I.

Chapter 4 and Chapter 5 were aimed at accurate attenuation map estimation for brain perfusion scan and DaTscan. In Chapter 4, a CNN based approach was developed that solely uses SPECT data for attenuation map estimation. The proposed CNN method was validated using Monte Carlo simulated brain perfusion scans. The bed trajectory investigated in Chapter 3 was used in this Chapter for brain perfusion imaging with G-SPECT-I.

The proposed CNN method in Chapter 4 was tested for DaTscans in Chapter 5. Meanwhile, the sampling strategy developed in Chapter 2 was used for the Monte Carlo simulation of DaTscans in Chapter 5. Different CNN architectures were investigated for an optimal application on DaTscans acquired with a focused striatum strategy. We concluded that accurate attenuation maps can be estimated by only using SPECT data, which could enable attenuation correction to be independent from other modalities for full brain perfusion and DaTscan imaging.

Chapter 6 provides a conclusion on this thesis. Besides, the value of this thesis and its limitations were discussed.

2

Optimized image acquisition for dopamine transporter imaging with ultra-high resolution clinical pinhole SPECT

This chapter is adapted from:
Yuan Chen, Brendan Vastenhouw, Chao Wu, Marlies C. Goorden, Freek J. Beekman. *Optimized image acquisition for dopamine transporter imaging with ultra-high resolution clinical pinhole SPECT*, Physics in Medicine & Biology **63** (2018), 225002 [27].

SPECT can be used to image dopamine transporter (DaT) availability in the human striatum, e.g. for diagnosis of Parkinson's disease (PD). As traditional SPECT provides limited resolution and sensitivity, we proposed a full ring focusing multi-pinhole SPECT system dubbed G-SPECT-I (Beekman 2015 *Eur. J. Nucl. Med. Mol. Imaging* 42 S209) which demonstrated a 2.5 mm reconstructed resolution in phantom scans. G-SPECT-I achieves data completeness in the scan region of interest by translating the patient bed with an *xyz*-stage and combining projections from all bed positions into image reconstruction using a scanning focus method (SFM). This paper aims to develop dedicated SFM parameters for performing a DaTscan with high effective sensitivity and appropriate sampling. To this end, the axial scanning length was restricted and transaxial bed trajectories with a reduced number of positions based on a convex hull data-completeness model were tested. Quantitative accuracy was assessed using full G-SPECT-I simulations of an Alderson phantom based on measured system matrices. For each sampling strategy, the specific binding ratio (SBR) and asymmetry index (AI) in the left and right striatum, as well as the localized SBR (L-SBR) and the localized AI (L-AI) in eight striatal sub-regions were calculated and compared to those of the reference scan which performs full brain oversampling using 112 bed positions. Results show that structures essential for PD diagnosis were visually and quantitatively barely affected even when using the lowest number of bed translations (i.e. 4). The maximum deviation from the reference was only 1.5%, 1.5%, 5.5% and 7.0% for the SBR, AI, L-SBR and L-AI, respectively, when 4 positions were used. Thus, it is possible to perform an accurate DaTscan with a confined axial scan region and a limited number of focused bed positions. This enables protocols for extremely fast dynamic SPECT scans with less than half-minute time frames, which can be useful for motion correction.

2.1. Introduction

SPECT imaging of the dopamine transporter (DaT) density with e.g. ^{123}I-ioflupane has been used as an imaging biomarker for e.g. Parkinson's disease diagnosis and for differentiation of dementia with Lewy Body from other dementias [28–31]. Currently, the diagnosis derived from a DaTscan mainly relies on visual interpretation based on the bilateral striatal shape, the striatal symmetry, the gradient between the two striatal parts (caudate and putamen) and the striatal DaT density [32]. However, conventional dual-head SPECT scanners equipped with low-energy high-resolution (LEHR) parallel hole collimators - the most frequently used collimators for SPECT DaT imaging [33, 34] - generally provide a limited resolution of about 8-10 mm and a sensitivity of about 70-90 cps/MBq/head [35]. This results in a compromised ability to recover the striatum and to separate putamen and caudate, and demands a long scanning time and/or a relatively high radioactive dose. The development of three-head fan beam SPECT was an attempt to improve the resolution-sensitivity tradeoff by the use of image magnification with converging collimation and the use of more detectors surrounding the patient. While the sensitivity was indeed increased to around 250 cps/MBq (e.g. GCA-9300A and Prism 3000XP [35, 36], the resolution that was achieved was only slightly improved to about 7 mm [37–40]. Some

dedicated brain SPECT scanners have been developed that strive to achieve a slightly better resolution by either using sophisticated detectors (e.g. Mediso X-Ring/4R), or a large number of focusing collimators and detectors (e.g. NeuroFocus and inSpira HD with a resolution of about 7 mm [41–43]), yet only few clinical validations with these scanners are available [42, 44, 45] and some are not even manufactured anymore. A SPECT system which could achieve a much better resolution-sensitivity tradeoff would be very desirable for its ease of dose requirement and possibility for dynamic scans or longitudinal studies.

Recently, SPECT systems with multi-pinhole collimators are gaining increasing interest owing to their enhanced resolution-sensitivity tradeoff, especially when imaging small objects. Research has been carried out in many groups to improve the performance of brain SPECT by optimizing a multi-pinhole system geometry in simulations [12, 13, 46–48]. However, to the best of our knowledge, these systems are still in the design phase and few have acquired physical scans. In [34], a physical multi-pinhole SPECT system was assembled by mounting 20-multipinhole collimators onto a dual-head conventional SPECT scanner. The authors concluded that with their chosen multi-pinhole collimator, scan time can be shortened by one-third compared to that of a LEHR collimator (20 min against 30 min) while achieving comparable image quality. However, with the big aperture size of 7.5 mm and the small pinhole-detector distance compared to the object-pinhole distance, the authors estimated the resolution of this multi-pinhole SPECT system to be about 20.6 mm.

Our group recently launched a multi-pinhole clinical SPECT system with full angular coverage using stationary detectors, that demonstrates excellent resolution-sensitivity tradeoff (G-SPECT-I [10]). For objects the size of a human head, unprecedented resolutions and sensitivities were achieved in phantom scans: 2.5 mm resolution with 415 cps/MBq sensitivity and 3.5 mm resolution with 896 cps/MBq sensitivity, using 3-mm and 4.5-mm-diameter pinhole collimators respectively. These collimators contain a total of 54 focusing pinholes and a total of nine large field of view cameras surrounding the patient (Figure 2.1). The geometry is designed such that all pinholes are 'viewing' a central volume, in which a very high sensitivity is obtained over a 360° angular range. This central volume is referred to as the complete data volume (CDV) in subsequent sections, as photons emitted from this volume are captured by all pinholes at different angles and sufficient angular sampling for accurate image reconstruction is attained without any detector rotation or bed shift. For extending the volume from which complete data is obtained, the bed is stepped through the scanner with an automated *xyz*-stage, allowing different parts of the patient to be positioned in the CDV. Projections from all pinholes and all bed positions are then used simultaneously for image reconstruction, a strategy referred to as the scanning focus method (SFM) [49]. Preclinical applications of a similar design have been successfully applied in U-SPECT+ [7, 49, 50] which enables dynamic animal scans with sub-second frame dynamics or extremely low dose scans (fractions of

1 MBq). Hence, it may be possible that the G-SPECT-I technology could bring e.g. dynamic scanning or very low dose (longitudinal) scanning into reach for larger subjects, including patients.

This paper focuses on an optimal application of G-SPECT-I to DaT imaging with high effective sensitivity. It is plausible that this could be achieved by confining the scan to the volume of interest (VOI) in which the striatum locates, such that more gamma photons from the VOI are captured and the effective count yield is increased compared to that for whole brain scanning. Based on the Hammers N30R83 brain atlas [51] (average over 30 healthy MR scans) and a CT image of the Alderson brain phantom, the axial length of the striatum is estimated to be about 35 mm. Actually, visual inspections and semi-quantitative analyses of DaTscans often only use the three consecutive slices with the highest striatal intensity, which in total measure approximately 10 to 12 mm axially [52–55]. Hence, we aim to ensure an accurately reconstructed region of 35 mm in the axial direction, which should be more than sufficient for DaTscan analysis. However, for a scan confined to only part of the brain it needs to be investigated whether limited sampling and projection truncation in axial direction do induce artefacts. Apart from confining the axial scan region, it is also desirable to optimize the bed translation trajectory on the transaxial plane such that, (i) sufficient sampling on the transaxial plane is ensured to circumvent the interior problem, and (ii) the effective count yield is maximized. The latter can be achieved by placing transaxial bed positions such that they focus more on the striatum and/or by limiting the number of bed positions to reduce the overhead time needed for the bed movements. However, a more focused bed position placement may not cover the entire brain especially the periphery, and scanning with a limited number of bed positions may mean that not every part of the scan region is covered at least once by the CDV. Both could have consequences for data completeness over the VOI and thus have to be investigated in detail.

The aim of this paper is to develop sampling strategies for G-SPECT-I DaT imaging with high effective sensitivity by (i) confining the scan region in the axial direction, and (ii) focusing the bed positions transaxially in the brain and limiting the number of transaxial bed positions, while always ensuring sufficient sampling in the transaxial plane. Quantitative accuracy attained with different sampling strategies is assessed using full G-SPECT-I system simulations of an Alderson phantom based on measured system matrices.

2.2. Methods

2.2.1. System design and collimator geometry

G-SPECT-I (Figure 1.1) is based on a stationary ring consisting of nine pinhole-collimated gamma cameras with large-area 595 × 472 × 9.5 mm NaI crystals. The interchangeable nonagon-shaped collimator assumed in this paper consists of a total of 54 3-mm-

diameter pinhole apertures. Pinholes are placed in 3 rings with a relative rotation of 1/3 of an inter-pinhole distance in between rings. Pinholes each have an opening angle of 27°, all focusing on the CDV (Figure 1.1). The transaxial diameter R_c and axial length L_c of the CDV are 100 mm and 60 mm respectively. A precisely controlled 3D stage is incorporated for bed translations, enabling enlargement of the scan region. Scan region selection can be accomplished with the system's user interface that takes the images from three optical cameras as its input (Figure 1.1a), see description in [56, 57]. The influence of intrinsic detector resolution (3.5 mm) is diminished by using a pinhole-detector distance (542 mm) that is larger than the object-pinhole distance (215 mm), such that projections are magnified onto the detector. Images from each pinhole are directly projected on the detectors. Shielding is placed between the pinhole and the detector to prevent overlapping projections. The inner diameter of the collimator is about 400 mm, making the system suitable for brain, selected extremity or pediatric imaging.

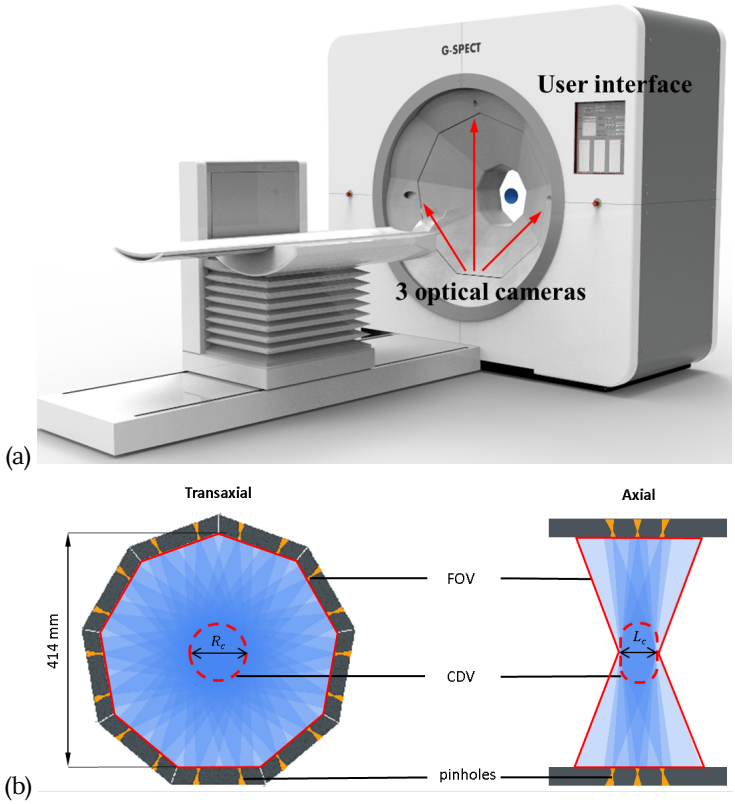

Figure 2.1: Illustration of G-SPECT-I scanner. (a) G-SPECT-I system with three optical cameras and a user interface for VOI selection; (b) multi-pinhole collimator of G-SPECT-I system. All 54 pinholes distributed over three rings are focusing on the CDV. Pinholes each have an opening angle of 27°, resulting in a CDV with transaxial diameter R_c of 100 mm and axial length L_c of 60 mm.

2.2.2. Convex hull principle

Sufficient sampling in the transaxial plane can be ensured by providing over 180° angular coverage for each point in the brain [58–60]. As G-SPECT-I employs a multi-bed-position scan and uses the SFM which combines projections from different bed positions simultaneously into reconstruction, sufficient angular coverage is achieved when the brain is contained in the convex hull surrounding the CDVs from different scan positions. This is referred to as the convex hull principle and a demonstration of this principle is provided in Figure 2.2. Figure 2.2(a) shows that the angular coverage α in the point p is determined by the angle between the two lines tangential to the CDV. Furthermore, Figure 2.2(b) demonstrates that in case of two CDV positions, the angular coverage α in the point p is the union of the coverage from the two CDVs. Figure 2.2(c) gives an example of over 180° angular coverage being achieved in the transaxial plane for a brain scan with four CDV positions. The circles indicate the CDVs and the orange line denotes the convex hull surrounding the CDVs. Any point within the convex hull obtains an angular coverage of more than 180°.

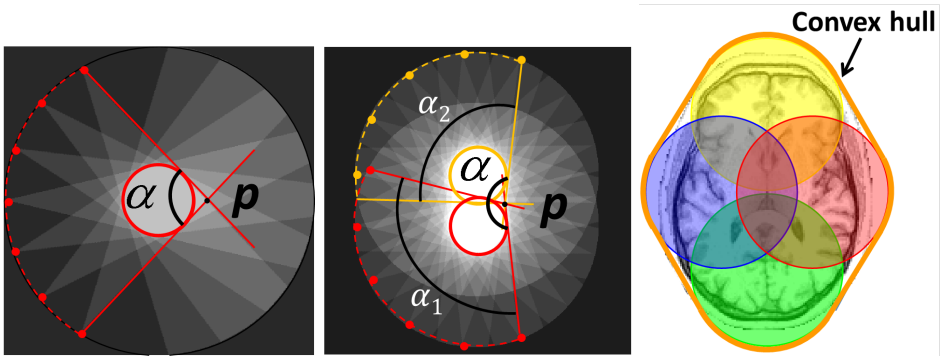

Figure 2.2: Illustration of convex hull principle in the transaxial plane. The red and yellow circles in (a) and (b) indicate the CDVs. (a) The angular coverage α in point p is determined by the angle between the two lines tangential to the CDV. (b) In case of two CDV positions, the angular coverage α in the point p is the union of the coverage from the two CDVs. (c) An example of full angular coverage being achieved in this transaxial plane for a brain scan with 4 CDV positions. The circles indicate the CDVs and the orange line denotes the convex hull surrounding the CDVs.

2.2.3. Sampling sequence

As G-SPECT-I enables selection of the VOI that is to be scanned (via the user interface shown in Figure 2.1), users can select the VOI based on the head contour on the optical images when performing a DaTscan, and the sampling sequence is then designed based on the selected VOI. Below we explain a general protocol for designing sampling sequences that should work on a variety of subjects. We aim to cover the entire brain in the convex hull with an extra minimal margin of 5 mm (minimal distance between the convex hull

and the brain) for every subject in the test. This is to compensate for any mispositioning when selecting the VOI, and to make the protocol more applicable to all types of patients.

For our sampling sequence design, 30 brain MR scans were randomly selected from the HCP database [61] to check how one should position the bed transaxially once the head contour is known. First, a box (the selected VOI) was drawn manually on the transaxial plane based on the skull contour for each subject (as in Figure 2.3a) with ImageJ [62]. This box is selected to be just large enough to cover the head and this was checked by scrolling through all transaxial slices. Secondly, four sampling sequences with a reduced number of bed positions, from oversampling using 16 positions per plane, to 8, 6 and 4 were designed based on the selected VOI. All the transaxial sampling sequences follow elliptical trajectories. Initially these sequences were chosen such that the convex hull was just contained within the box as in Figure 2.3(b)-(e). In Figure 2.3, the dashed blue box is the selected VOI and the orange line highlights the convex hull. Then, we checked if the convex hull was large enough to cover the brain of all subjects with a minimal margin of 5 mm. When this was not the case, bed positions were shifted outwards to enlarge the convex hull as in the example of Figure 2.3(f) where the bed positions are shifted resulting in a convex hull 10 mm outside the VOI box. We performed this procedure for all four sampling sequences on each subject, increasing the shift in steps of 1 mm, until the minimal margin of 5 mm was obtained for every subject. This way, we found that the sequences need to be shifted outwards by 0 mm, 2 mm, 5 mm and 15 mm when 16, 8, 6 and 4 bed positions were used, respectively. For clinical scans with G-SPECT-I, the VOI selection based on the optical images could be affected by scalp, hair, head support, etc. As a result, we would expect a slightly larger VOI than the one selected on the MR images, meaning that the minimal margin of 5 mm is a conservative estimation.

The above knowledge was subsequently applied in transaxial sequence design for a DaTscan with the Alderson phantom (RSD, USA). The VOI as indicated by the dashed blue box in Figure 2.4(a)-(d) was selected based on the head contour of the phantom. The sampling sequences were then designed based on the selected VOI, taking the required shift according to MR scan findings into account.

For sufficient sampling along the axial direction, the transaxial bed positions are replicated. The required number of axial bed stops and distance between them are investigated. Firstly, as a reference, we start with a full brain scan with a large number of bed stops to be sure that sampling is more than sufficient. This scan with full brain oversampling uses 7 axial bed stops as well as 16 bed positions per transaxial plane (thus a total of 112 bed positions is used). The distance between subsequent axial bed stops is set to 21 mm, which is small compared to the axial coverage L_c (60 mm) of each CDV.

To optimize the scanning length in axial direction, a reduced number of axial bed stops down to only one stop at the central position in the striatum is subsequently tested. The distance between consecutive axial bed stops remains 21 mm while oversampling is al-

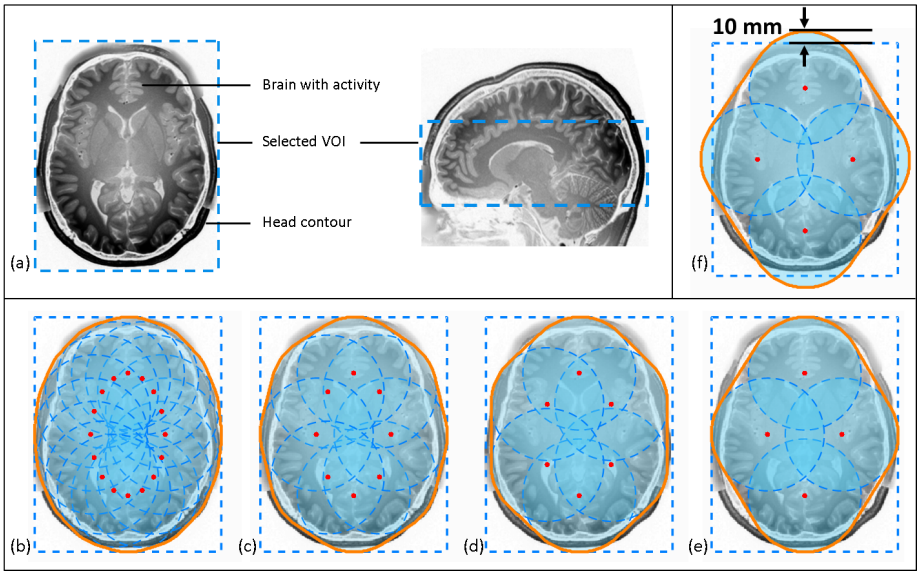

Figure 2.3: Illustration of VOI selection and the design of sampling sequences based on a set of MR scans. (a) Selection of the VOI based on the skull contour on an MR scan; (b)-(e) initial design of sampling sequences based on the selected VOI using 16, 8, 6 and 4 bed positions per transaxial plane. (f) Sampling sequence initially designed based on the skull contour is now shifted resulting in a convex skull 10 mm outside of the VOI. The dashed blue box is the selected VOI and the orange line indicates the corresponding convex hull. The bed positions are highlighted by the red dots that follow an elliptical trajectory. The semi-transparent blue circles with dashed blue edge are the CDVs at different bed positions.

ways ensured with 16 bed positions in the transaxial plane as performed in the reference image. This is to investigate whether projection truncation in the axial direction that occurs when the axial scan length is confined would induce artefacts. Meanwhile, transaxial sampling with fewer (8, 6 and 4 as in Figure 2.4) bed stops is tested for each simulated scan with a set axial scanning length.

Additionally, to determine the optimal distance between axial bed positions, we increase the distance from 21 mm to 42 mm and to 60 mm (equal to the axial CDV length L_c). All the other procedures remain the same as implemented for 21 mm axial distance (i.e. gradually reducing the number of axial bed positions and testing with a reduced number of transaxial bed positions). All simulated scans are compared with the oversampled reference image.

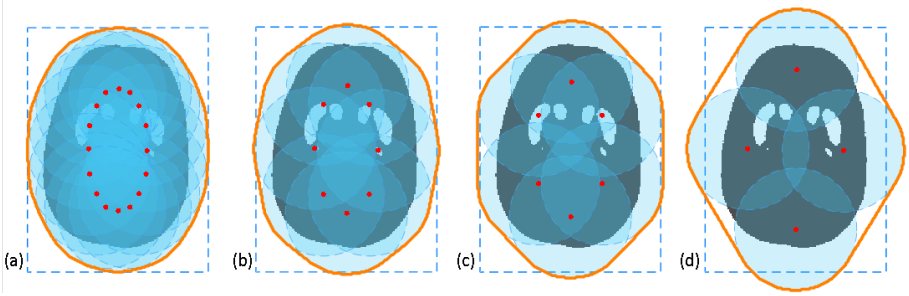

Figure 2.4: Transaxial sampling sequences used in this paper for a DaTscan of the Alderson phantom. Panels (a)-(d) show the sequences with 16, 8, 6 and 4 bed positions per transaxial plane as in Figure 2.3, but with a shift of 0 mm, 2 mm, 5 mm and 15 mm respectively based on the test results of the MR scans to contain the brain in the convex hull with a minimal margin of 5 mm.

2.2.4. Simulations

A digital phantom containing four striatum parts (left/right putamen and left/right caudate) was generated based on a CT image of the physical Alderson phantom. The remaining brain volume is the background compartment. Striatum-to-background concentration ratio is set to 8:1 to mimic a realistic distribution of ^{123}I-ioflupane (159 keV) in the brain. The emission process simulator is based on ^{99m}Tc (140 keV) point source measurements and geometry modeling [63]. This approach of modeling low-energy isotope transport is also used when reconstructing experimental scans and has proven to provide good performance in many cases [57, 64–66]. Resolution is barely degraded when applied to isotopes with nearby peak energies (e.g. ^{111}In with photopeak of 171 - 245 keV [57] and ^{123}I with photopeak of 159 keV) compared to the scans with ^{99m}Tc. The phantom for projection has a voxel size of 0.75 mm, half the size of voxels in the reconstructed images, to mimic a continuous activity distribution. Both the projection simulation and reconstruction model the same physical effects, e.g. collimator attenuation, detector blurring, etc. and are derived from the same set of point source measurements. Besides, to make the simulation more realistic, phantom attenuation is modelled in the simulated projections using a voxelized ray tracer [67, 68]. The attenuation map is derived by segmenting the CT image of the Alderson phantom, and assigning attenuation coefficients of 0 cm^{-1} to air, 0.15 cm^{-1} to soft tissue and 0.31 cm^{-1} to bone. Similarity-regulated OSEM [18] with 8 subsets and 10 iterations is performed using SFM which combines projections from all bed positions simultaneously into image reconstruction. As we here aim to quantify errors induced only by sampling, no noise is simulated.

Moreover, to quantify the effects of different sampling strategies on the striatal count yield, a separate digital phantom with only the striatum was made by setting the tracer concentration in the background compartment to 0. The total striatal count for each sequence with reduced sampling is divided by that obtained with the reference scan. This way the gain of striatal count yield compared to that of the reference full brain oversampling is obtained.

2.2.5. Evaluation

As performed in clinical DaTscan assessment, visual inspection and semi-quantification of the DaTscan images are both included. The latter is achieved by calculating the specific binding ratio (SBR) and the asymmetry index (AI) in the left and right striatum, as well as the Localized SBR (L-SBR) and the Localized AI (L-AI) in eight striatal sub-regions. The definitions of the metrics are given by:

$$\text{SBR} = \frac{C_{VOI\_str} - C_{VOI\_bkg}}{C_{VOI\_bkg}} \tag{2.1}$$

$$\text{AI} = 2 \times \frac{C_{RVOI\_str} - C_{LVOI\_bkg}}{C_{RVOI\_str} + C_{LVOI\_bkg}} \times 100\% \tag{2.2}$$

Here C_{VOI_bkg} denotes the mean DaT image intensity in the background VOI. C_{VOI_str} represents the mean DaT image intensity within the striatal region, with C_{LVOI_str} and C_{LVOI_str} referring to the left and right part of striatum, respectively. While SBR and AI take values from the entire left or right striatum at one central slice as usually performed with traditional SPECT (Figure 2.5a), L-SBR and L-AI give more detailed assessments in eight striatal sub-regions individually (Figure 2.5b). These eight striatal VOIs, i.e. the posterior, middle and anterior putamen, and the caudate, for both the left and right striatum, are generated in PMOD v3.7 (PMOD Technologies Ltd., Switzerland) by placing small circles or ellipses over the putamen and caudate on the transaxial slices and are placed over 10.5 mm slices in the axial direction. The three parts of the putaminal VOIs have almost equal area on each transaxial slice. As there is no cerebellum or occipital cortex in the Alderson phantom, the background region is generated using the Southampton

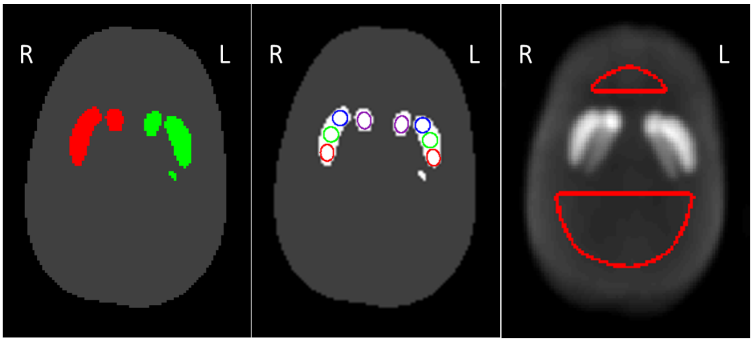

Figure 2.5: VOIs for semi-quantitative analysis. (a) Striatum VOI taken from the phantom at the central slice of the striatum; (b) example of eight striatal VOIs on one transaxial slice; (c) background VOI generated using the Southampton method. In (a), the left and right striatum are denoted by the red and green shapes, respectively. In (b), the striatal VOIs consist of eight sub-regions that are indicated by circles or ellipses in different colors. Red, green, purple and blue ones denote the posterior, middle, anterior putamen and the caudate, respectively. The background VOI in (c) is composed of two parts highlighted by the red shapes.

method (Figure 2.5c) [69]. No filtering is applied on the phantom or the DaTscan images for the semi-quantification analysis to reduce partial volume effects.

As an additional quantitative measure of the image quality within the entire transaxial brain, the Maximum Undersampling Error (MaxUSE) and Average Undersampling Error (AvgUSE) are calculated. These two metrics are defined as the maximum and average relative difference of each reconstructed image from the oversampled reference image, respectively. The relative difference is expressed by:

$$\text{Difference(i)} = \frac{\text{Image}(i) - \text{Reference}(i)}{\text{Reference}(i)} \tag{2.3}$$

where i denotes the image voxel. All images are post filtered with a Gaussian filter of 4 mm full width at half maximum (FWHM) to suppress insignificant local fluctuations. Afterwards, the relative difference is calculated based on Equation 2.3. As the relative differences can be either positive or negative, the absolute values are used for the calculation of MaxUSE and AvgUSE. Only the voxels within the brain are taken into account. Since the quantitative assessment of a DaTscan in a clinical setting is typically based on regions with the size of striatal structures (from 4 cm^3 to 12 cm^3 [52, 54, 69]), we resized the Difference image from a voxel size of 1.5 mm to $10.5 \times 10.5 \times 9$ mm^3. This gives cubic VOIs of about 1 cm^3, which are small enough to estimate relevant intensity deviations in the striatal structures.

2.3. Results

2.3.1. Visual inspection

To illustrate the visual effect on DaTscan images when reducing the number of bed positions, Figure 2.6 shows the gold standard (digital phantom), the reference reconstruction (simulated full brain oversampling scan), and three representative DaTscans acquired with a reduced number of bed positions. Five slices within an axial region of 36 mm that are most relevant to DaTscan inspection and quantification are displayed. The center of the striatum in axial direction is defined as 0 mm, while the slice 18 mm underneath or above the center is defined to be at -18 or 18 mm, respectively. Figure 2.6 demonstrates that reducing the number of bed positions from full brain oversampling to 16 positions hardly has a visual effect on DaTscan images. When further decreasing the number of bed positions, background homogeneity is somewhat degraded due to the presence of stripe artifacts. However, for the striatum and its sub-structures, the shapes are always preserved with no obvious distortions, even with the use of only 4 bed positions. A full overview of the DaTscan images for all the tested sampling sequences using 1 or 2 axial positions as well as their difference images from the reference scan are included in the appendix (Figure 2.9-2.12).

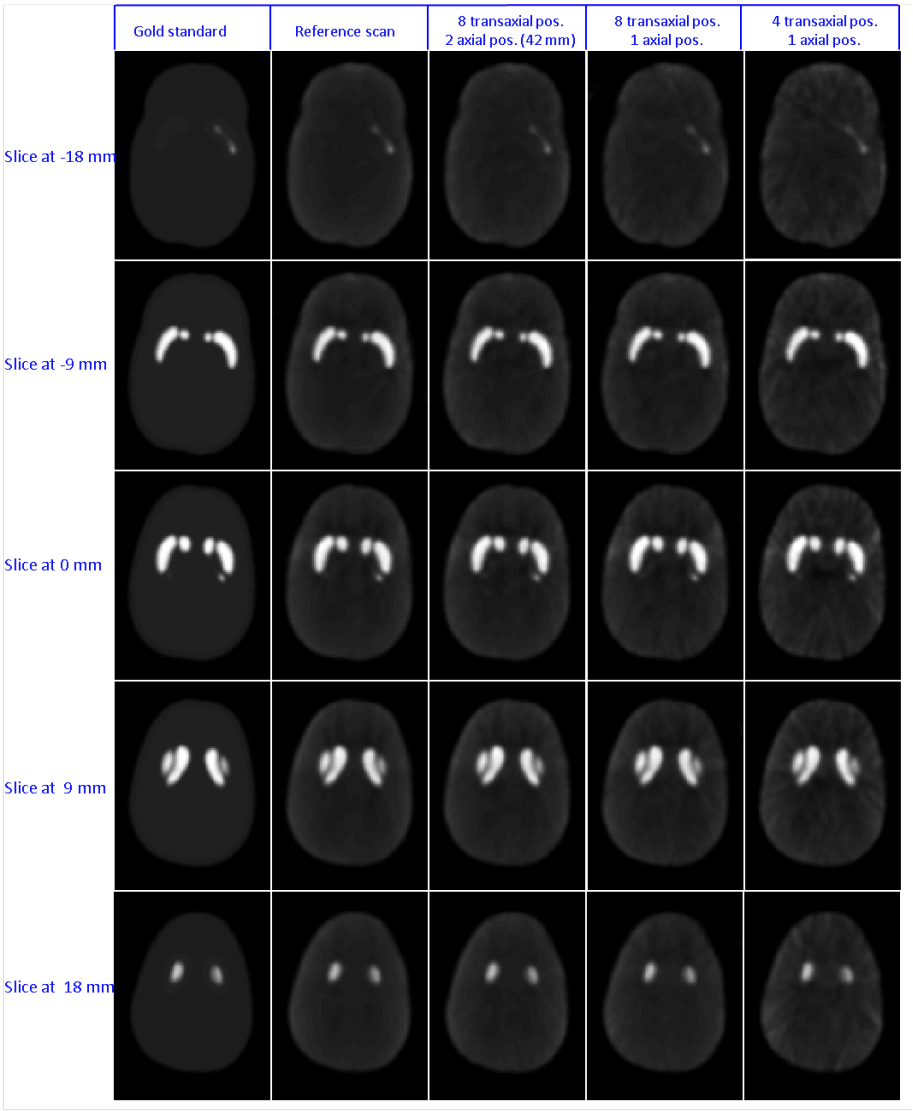

Figure 2.6: Comparison of the DaTscan image slices from the gold standard (the digital phantom), the reference scan (simulated full brain scan with oversampling), the DaTscan acquired with 2 axial positions combined with 8 transaxial positions (distance between 2 axial positions is 42 mm), the scan with 1 axial position combined with 8 transaxial positions, and the scan with 1 axial position combined with 4 transaxial positions. The center of the striatum in axial direction is defined to be at 0 mm. The top row to the bottom row represent the slices from 18 mm underneath the center of the striatum to 18 mm above it. All images have a pixel size and slice thickness of 1.5 mm and are post-filtered with a Gaussian filter of 4 mm FWHM. The concentration ratio in striatum and background compartment is 8:1. A full overview of the DaTscan images for all the tested sampling sequences using 1 or 2 axial positions as well as their difference images from the reference scan are included in the appendix.

2.3.2. Semi-quantification

Table 2.1-2.2 show the effect on SBR quantification when scanning with a reduced number of bed positions. For validation of the oversampled reference scan, the SBR and L-SBR from the phantom are included for comparison and are denoted as a Gold Standard SBR (GS-SBR) and GS-L-SBR, respectively, while those from the reference scan are termed the Ref-SBR and Ref-L-SBR. Table 2.1 demonstrates that accurate SBR quantification can be achieved with the reference full brain oversampling. A maximum deviation of 3.1% and 6.3% in the posterior putamen and among all eight striatal sub-regions, respectively are found when comparing the Ref-L-SBR with the GS-L-SBR. When decreasing the number of axial and/or transaxial bed positions from the oversampled reference scan, the effect on SBR quantification is very limited (Table 2.2), which is demonstrated by a maximum

Table 2.1: Deviation between the reference scan and the GS in terms of SBR and L-SBR. Sub-regions are assessed separately. Post Put. = posterior putamen, Mid. Put. = middle putamen, Ante. Put. = anterior putamen. "L" and "R" indicate the left and right striatum, respectively. The deviation is calculated by subtracting the GS-SBR from the Ref-SBR and normalized by dividing by the GS-SBR. The same goes for the deviation of L-SBR The absolute value of the deviations is used.

	L-SBR in eight sub-regions								**SBR striatum**	
	Post. Put.		Mid. Put.		Ante. Put.		Caudate		Striatum	
Deviation from GS	R(%)	L(%)	R(%)	L(%)	R(%)	L(%)	R(%)	L(%)	R(%)	L(%)
Reference scan (112 pos.)	2.16	3.05	0.71	6.03	2.35	6.32	5.39	0.22	6.83	3.91

Table 2.2: Deviations from the Ref-SBR and Ref-L-SBR for scans with a reduced number of bed positions. The 21 mm and 42 mm in parenthesis in the first column indicate the distance between the two axial bed positions. Post Put. = posterior putamen, Mid. Put. = middle putamen, Ante. Put. = anterior putamen. 'R' and 'L' indicate the right and left striatum, respectively. The deviation is calculated by subtracting the Ref-SBR and normalized by dividing by the Ref-SBR. The same goes for the deviation of L-SBR. The absolute value of the deviations is used.

		L-SBR in eight sub-regions								**SBR striatum**	
		Post. Put.		Mid. Put.		Ante. Put.		Caudate		Striatum	
Deviation from reference		R(%)	L(%)	R(%)	L(%)	R(%)	L(%)	R(%)	L(%)	R(%)	L(%)
One axial stop	16 trans. pos	0.74	3.08	4.53	4.28	1.15	3.91	6.17	5.04	4.53	3.57
	8 trans. pos	0.94	4.63	3.79	4.04	0.43	4.94	4.98	3.82	3.99	3.64
	6 trans. pos	3.58	6.58	0.89	1.46	0.13	3.52	0.41	2.77	2.43	3.34
	4 trans. pos	1.47	5.47	2.02	2.33	2.61	1.64	1.83	1.15	0.04	1.51
Two axial stops (21 mm)	16 trans. pos	2.32	2.35	3.32	2.03	3.19	3.17	3.64	2.88	2.94	2.94
	8 trans. pos	2.01	2.95	3.48	1.27	2.42	3.29	2.88	2.58	2.52	2.78
	6 trans. pos	3.30	3.32	0.64	0.74	1.89	1.88	0.30	0.19	1.07	1.70
	4 trans. pos	3.48	4.05	0.16	1.85	6.63	2.57	1.74	2.08	1.82	0.57
Two axial stops (42 mm)	16 trans. pos	0.64	0.23	0.22	0.23	1.24	0.66	1.11	0.24	1.47	0.27
	8 trans. pos	0.11	1.51	0.16	0.30	1.76	0.30	1.62	0.30	1.70	0.29
	6 trans. pos	1.14	0.27	0.17	0.64	1.63	1.94	2.83	1.56	2.45	0.23
	4 trans. pos	6.98	0.47	4.06	1.18	7.42	2.84	2.28	1.80	3.70	3.75

deviation of 4.5% and 7.4% from the Ref-SBR and Ref-L-SBR, respectively for all scans included in the table. Particularly, the mean deviation from the reference among all striatal sub-regions reads only 0.8% and 2.3% when using 16 positions (2 axial positions and 8 transaxial positions with a between stop distance of 42 mm) and 4 positions (1 axial positions and 4 transaxial positions), respectively. The results for 2 axial bed positions with a distance of 60 mm between stops is not included, as it leads to diminished focus on the striatum and larger errors compared to 42 mm distance (see Figure 2.11-2.12 in the appendix).

As another confirmation of the accurate SBR quantification for the tested sampling sequences, Figure 2.7 directly shows the L-SBR values. As a benchmark, the GS-L-SBR is also shown by the dotted red line of L-SBR = 7 since the striatum-to-background concentration ratio is set to be 8:1.

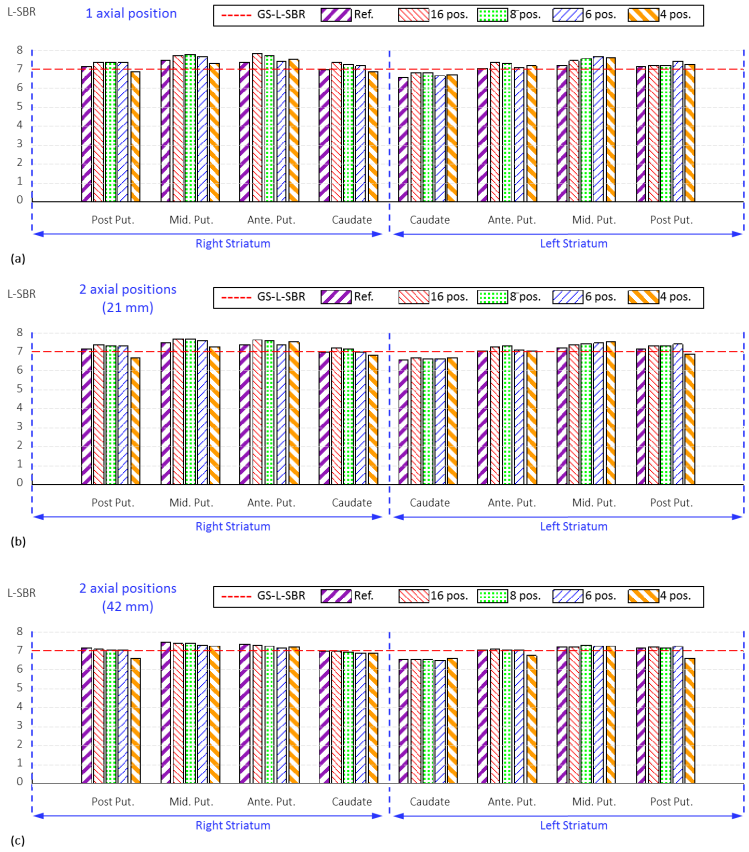

Figure 2.7: Comparison of the L-SBR for scans with different sampling sequences. The subplot at each row shows the results of (a) using 1 axial bed position, (b) using 2 axial bed positions with a between stops distance of 21 mm, and (c) using 2 axial bed positions with a between stops distance of 42 mm. The GS-L-SBR is indicated by the dotted red line (L-SBR = 7, since the striatum-to-background concentration ratio is 8), while the Ref-L-SBR is denoted by "Ref." in the figure.

Table 2.3-2.4 show the effect on left-right asymmetry when scanning with reduced number of bed positions. The definitions of GS-AI, GS-L-AI, Ref-AI and Ref-L-AI which refer to phantom and reference scan values, are the same as for SBR, but consider the left-right asymmetry index. The GS-AI and GS-L-AI are 0% since the intensity in the left or right striatum are all set to the same value in the phantom. Table 3 manifests that a good left-right symmetry can be achieved with the oversampled reference scan. A maximum Ref-L-AI of 6.3% among all the striatal sub-regions is found. For the posterior putamen, the intensity in the left or right has an almost perfect match, resulting in an asymmetry of only 0.05%. Similar to the SBR results, decreasing the number of axial and/or transaxial bed positions has a limited effect on the left-right symmetry (Table 2.4). The maximum deviation from the Ref-AI and Ref-L-AI is 2.4% and 7.0% in the striatum and among all eight striatal sub-regions, respectively for all scans included in the table. Particularly, the mean deviation from the reference reads only 1.4% and 3.7% respectively among all sub-regions when using 16 positions (2 axial positions and 8 transaxial positions with a between stop distance of 42 mm) and 4 positions (1 axial positions and 4 transaxial positions).

Table 2.3: Deviation between the reference scan and the GS in terms of AI and L-AI. The GS-L-AI and GS-AI are 0% as the intensity in the left or right striatum are all set to the same value in the phantom. The deviation from the GS-AI is calculated directly by subtracting the GS-AI (0%) from the Ref-AI, as AI is already a normalized index expressed in percentage. The absolute value of the deviations is given in the table. Post Put. = posterior putamen, Mid. Put. = middle putamen, Ante. Put. = anterior putamen.

Deviation from GS	**L-AI in eight sub-regions**				**AI in striatum**
	Post Put. (%)	Mid. Put. (%)	Ante. Put. (%)	Caudate (%)	Striatum (%)
Reference scan (112 pos.)	0.05	3.13	4.54	6.28	2.77

Table 2.4: Deviations between the scan with a reduced number of bed positions and the reference scan in terms of AI and L-AI. This deviation is calculated by directly subtracting the Ref-AI, as AI is already a normalized index expressed in percentage. The absolute value of the deviations is given in the table. Post Put. = posterior putamen, Mid. Put. = middle putamen, Ante. Put. = anterior putamen.

Deviation from reference		**L-AI in eight sub-regions**			**AI in striatum**	
		Post. Put. (%)	Mid. Put. (%)	Ante. Put. (%)	Caudate (%)	Striatum (%)
One axial stop	16 trans. pos	0.41	0.80	1.56	0.72	0.92
	8 trans. pos	0.50	0.30	1.14	0.21	0.34
	6 trans. pos	3.64	2.91	0.48	1.29	0.89
	4 trans. pos	4.10	6.98	0.18	3.46	1.45
Two axial stops (21 mm)	16 trans. pos	0.85	0.80	0.31	0.82	0.01
	8 trans. pos	0.40	0.33	0.59	1.29	0.25
	6 trans. pos	1.37	1.40	0.94	0.55	0.63
	4 trans. pos	3.32	6.57	1.56	3.93	2.40
Two axial stops (42 mm)	16 trans. pos	1.88	0.43	1.34	0.47	1.21
	8 trans. pos	1.89	1.80	1.80	0.00	1.43
	6 trans. pos	2.78	2.23	2.70	0.94	2.25
	4 trans. pos	0.48	3.35	1.84	2.98	0.05

Similar to Figure 2.7, Figure 2.8 directly shows the L-AI values for scans with different sampling sequences. While the maximum L-AI for the reference scan is 6.3% among all striatal sub-regions, this value degrades only slightly to 7.6% for all scans included in the figure, confirming the good left-right symmetry even when scanning with reduced sampling. Besides, compared to a mean L-AI of 3.4% for the reference scan, comparable result of 3.0% and 3.8% is achieved for the scan with 16 positions (2 axial positions and 8 transaxial positions with a between stops distance of 42 mm) and the scan with 4 positions (1 axial positions and 4 transaxial positions), respectively.

Figure 2.8: Localized asymmetry index results when using different sampling sequences. Assessment is performed in each sub-region as in Figure 2.7. Note that the scale is from 0% to 8%.

2.3.3. MaxUSE and AvgUSE

Table 2.5 summarizes the MaxUSE and AvgUSE for evaluation of the image quality in the entire transaxial plane when scanning with different sampling strategies. These two values are calculated from those transaxial slices relevant for a DaTscan, along an axial length of 36 mm (-18 mm to 18 mm). Table 2.5 shows that using a single bed position in axial direction results in a MaxUSE of 15.0%, 15.8%, 22.1%, 40.7% in relevant transaxial slices (-18 mm to 18 mm) when 16, 8, 6 and 4 transaxial bed positions are used respectively, while the AvgUSEs are all below 5.2% for the four sampling sequences. Besides, using 2 axial bed positions can improve both the MaxUSE and AvgUSE, while a 42 mm distance between axial stops gives the best accordance with the reference image compared to a 21 mm or 60 mm distance. For that separation, a MaxUSEs and AvgUSEs of 8.7% and 1.8% respectively could be achieved along 36 mm axial length when using 8 transaxial bed positions. These two values are only slightly affected (12.9% and 2.0%) when the axial length is extended to 90 mm (see the appendix). Increasing the number of transaxial bed positions from 8 to 16, the improvement of the results is limited.

Table 2.5: Comparison of the MaxUSE and AvgUSE for scans with different sampling strategies in the transaxial slices relevant for a DaTscan, along an axial length of 36 mm (–18 mm to 18 mm).

MaxUSE along an axial length of 36 mm		Number of transaxial positions			
		4	6	8	16
One axial position		40.7%	22.1%	15.8%	15.0%
Two axial positions	(21 mm distance)	39.6%	17.1%	12.5%	13.8%
	(42 mm distance)	29.0%	11.4%	8.7%	7.6%
	(60 mm distance)	30.8%	16.6%	18.6%	17.4%
AvgUSE along an axial length of 36 mm		Number of transaxial bed positions			
		4	6	8	16
One axial position		5.2%	3.4%	3.2%	3.6%
Two axial positions	(21 mm distance)	4.6%	2.9%	2.4%	2.5%
	(42 mm distance)	4.0%	2.6%	1.8%	1.2%
	(60 mm distance)	5.0%	4.0%	3.5%	3.4%

2.3.4. Striatal count yield

Table 2.6 gives the quantitative measure of how much striatal counts can be gained compared to the reference full brain sampling when using a confined axial scanning length and different transaxial sequences. All count numbers are relative to the striatal count yield obtained with the reference scan. This table indicates that using a limited axial scanning length leads to a higher striatal count yield than full brain imaging. The maximal gain in striatal count yield is a factor 2.8 when only 1 axial bed stop is used, while 2.6, 1.9 and 1.0 times higher count yields are obtained with two axial bed positions at a

distance of 21 mm, 42 mm and 60 mm, respectively. Meanwhile, the striatal count yield increases when more transaxial bed positions are applied. An increase of 10% is obtained when increasing the number of transaxial bed positions from 4 to 8. This is due to the fact that the sampling sequence can be more focused in the brain when more transaxial bed positions are used, while the whole brain is still contained in the convex hull (see Figure 2.4).

Table 2.6: Comparison of the striatal count yield for scans with different sampling strategies. All count numbers are normalized by dividing by the striatal count yield achieved for full brain oversampling (sequence for reference scan).

Striatal count yield gain compared to full brain oversampling	Number of transaxial positions			
	4	6	8	16
One axial position	2.45	2.65	2.77	2.83
Two axial positions (21 mm distance)	2.25	2.43	2.54	2.60
(42 mm distance)	1.64	1.74	1.81	1.85
(60 mm distance)	0.88	1.04	1.01	1.02

2.4. Discussion

We investigated the effects of using different sampling strategies on visual image quality, semi-quantitative analysis accuracy, and striatal count yield for DaT imaging. By testing on a series of sampling sequences with a reduced number of bed stops, we found that the use of only 4 bed positions (1 axial position combined with 4 transaxial positions) could already achieve very accurate semi-quantification. Compared to the oversampled reference scan, the deviation is only 1.5% for both the SBR and AI in the striatum, and 5.5% and 7.0% maximally for L-SBR and L-AI among eight striatal sub-regions. Meanwhile, with the same sequence a striatal count yield of 2.5 times that of the reference full brain imaging could be achieved. However, due to the reduced sampling with less bed positions, the homogeneity in the background region is degraded, which leads to an MaxUSE of 40.1% at a few pixels. For a DaTscan, this might not be an important issue as structures essential for PD diagnosis are visually and quantitatively barely affected. However, for other types of scans such as brain perfusion scans, the affected homogeneity in the brain should be avoided.

As expected, the use of only a single axial bed position results in the highest striatal count gain (2.8 times that of the reference scan), since all bed positions are placed central to the striatum in the axial direction. Meanwhile, increasing the number of transaxial bed positions can also improve the number of detected striatal counts, owing to the more focused bed position placement in the brain (see Figure 2.4 and Table 2.6). For example, using 8 transaxial positions leads to a 10% higher striatal count yield compared to utilizing 4 transaxial bed positions. It is worth noting that the total scan time is assumed to be the same for all simulated scans and the time for bed movements is not included in the

simulation since it is highly dependent on the bed in use. Thus a slight decrease of the striatal count yield would be expected when increasing the number of transaxial bed positions from 4 to 16 (e.g. 2 axial positions combined with 8 transaxial positions) under equivalent total scan time if this overhead time would be taken into account. This favors the choice of using 4 bed positions (an overhead time of about 6 s based on our rough estimation using the current G-SPECT-I bed in design) for a multi-frame dynamic scan or fast scan. With the use of 2 axial positions combined with 8 transaxial positions, the overhead time is estimated to be 24 s, which is still quite small compared to common acquisition times.

Note that here we aim to ensure an accurately reconstructed region of 35 mm in axial direction. Hence for clinical DaTscans, doctors who are familiar with DaTscan acquisition can select a VOI along an axial length of 35 mm. Determination of the striatum position could also be improved based on a brain MR database analysis that G-SPECT-I could provide. On the other hand, the scan region in axial direction can be extended by using more axial bed positions, which is shown by comparing the results of using 1 or 2 axial positions in the appendix (Figure 2.9-2.12). For the use of 2 axial positions combined with 8 transaxial positions, the MaxUSE and AvgUSE are below 12.9% and 2.0% respectively along a 90 mm axial length, while very accurate semi-quantification results are still achievable (a deviation of 1.7% and 1.4% for the SBR and AI respectively in the striatum, and 1.8% and 1.9% maximally for the L-SBR and L-AI among eight striatal subregions).Thus an extended axial region (e.g. 90 mm) could be selected to compensate for some mispositioning uncertainty (27 mm in both directions axially). As 90 mm is already much larger than the axial length of the reconstructable region aimed for (35 mm), more axial bed positions are not included.

We modelled attenuation using a voxelized ray tracer in the simulated projections. Attenuation correction is not performed for this study as it is not trivial with multi-pinhole systems and we aim to focus on sampling issues here. The reconstructed DaTscan images (Figure 2.6) show that attenuation results in reduced intensities in the central part of the image, which is similar to what happens using parallel hole collimated SPECT systems. Nevertheless, the effect of different sampling sequences on G-SPECT-I DaTscan semi-quantification turns out to be not significant even with attenuation (Figure 2.7-2.8 and Table 2.1-2.4).

2.5. Conclusion

We have designed and evaluated different sampling strategies for performing a DaTscan based on full G-SPECT-I simulations using measured system matrices. We find that structures essential for PD diagnosis were visually and quantitatively barely affected even when using four bed positions (a deviation of 1.5% for both the SBR and AI in the striatum, and 5.5% and 7.0% maximally for L-SBR and L-AI, respectively, among eight striatal sub-

regions). With such a focused striatum scan, the effective count yield from the striatum increased by a factor of 2.5 compared to full brain imaging and much less overhead time is needed. This could enable acquisition with a total estimated overhead of bed-moving of only a few seconds and protocols for extremely fast dynamic brain SPECT and motion correction. Thus, the use of a limited number of bed positions does not significantly affect quantitative accuracy of a DaTscan while the striatal count yield is improved.

Appendix

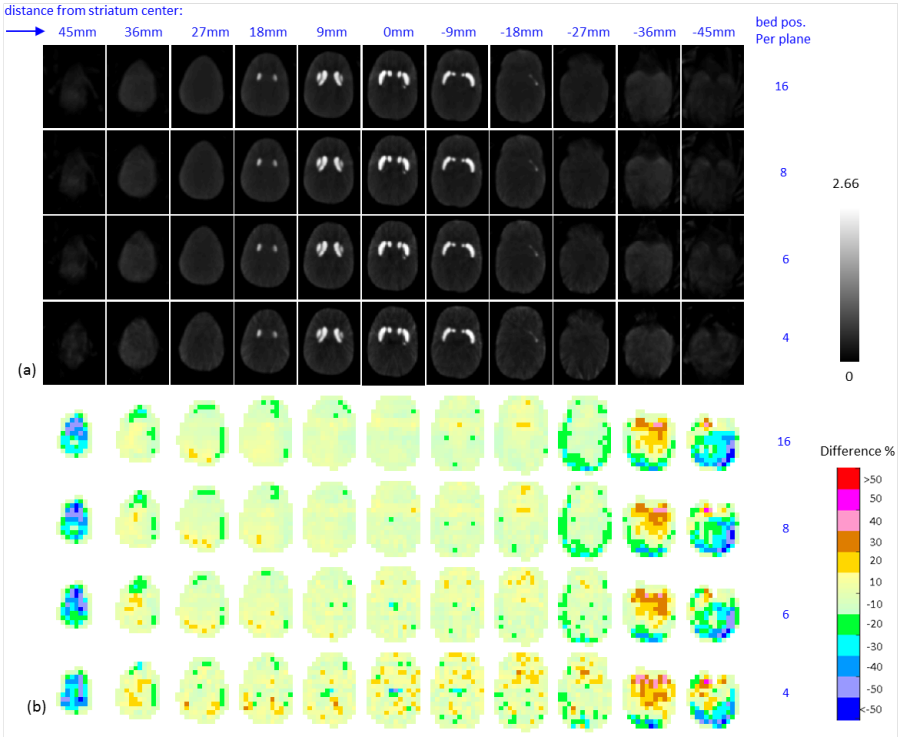

Figure 2.9: Comparison of simulated DaTscan images with the reference image when a single axial bed position is used. The single axial bed position is placed at the center of the striatum. (a) The simulated DaTscan image; (b) the Difference image calculated from the relative difference between the simulated DaTscan image in (a) and the reference image. Each row in (a) corresponds to one simulated scan, with the transaxial bed positions decreasing from 16, 8, 6 to 4 from the top to the bottom row, respectively. Images from left to right show the transaxial slices from 45 mm above the center of the striatum to 45 mm underneath it. The simulated DaTscan images in (a) have a pixel size and slice thickness of 1.5 mm and are filtered with a Gaussian filter of 4 mm FWHM. The Difference images in (b) have a pixel size of 10.5 mm and slice thickness of 9 mm.

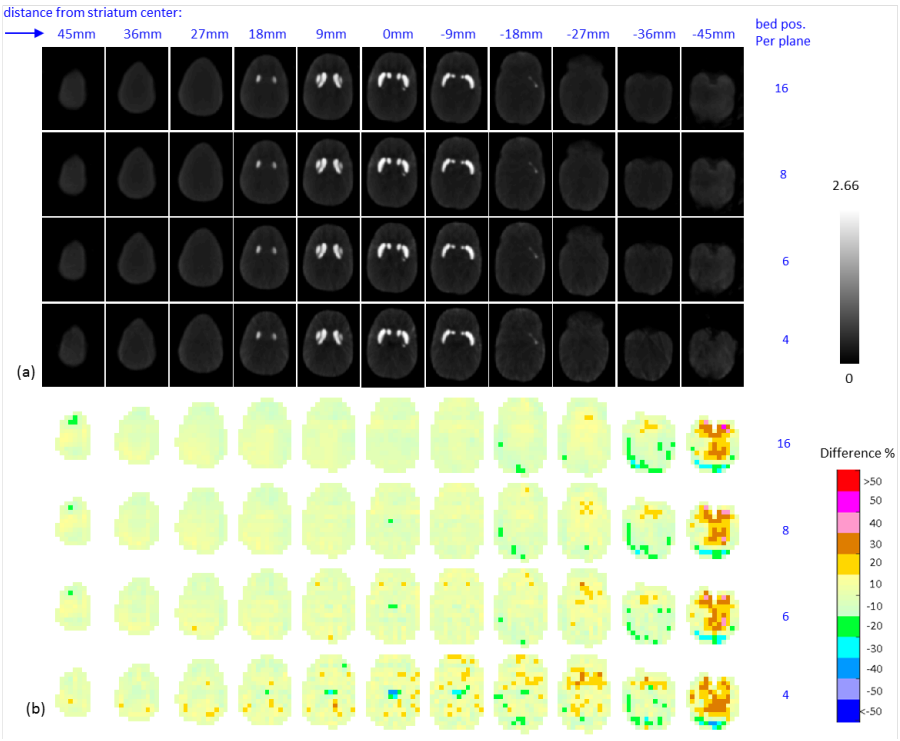

Figure 2.10: Like Figure 2.9, but with two axial bed positions with a between stops distance of 21 mm.

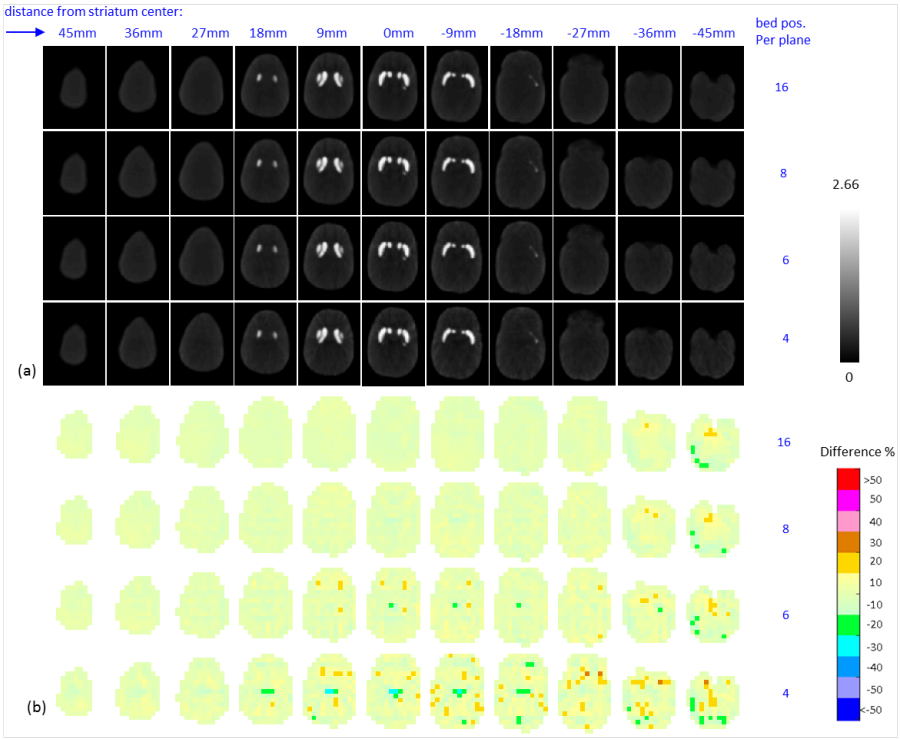

Figure 2.11: Like Figure 2.9, but with two axial bed positions with a between stops distance of 42 mm.

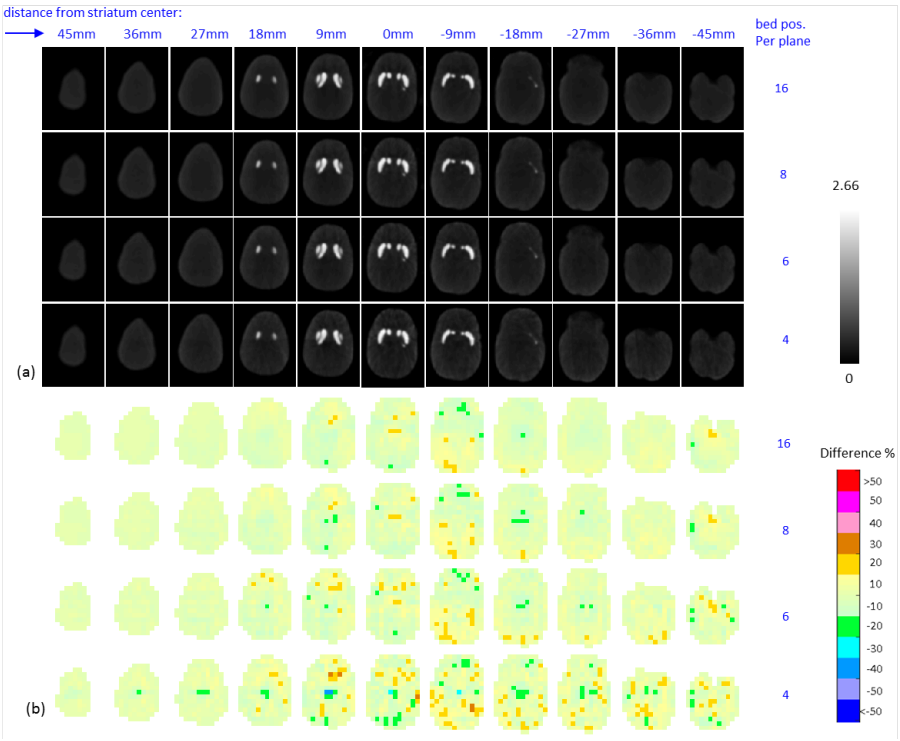

Figure 2.12: Like Figure 2.9, but with two axial bed positions with a between stops distance of 60 mm.

3

Optimized sampling for high resolution multi-pinhole brain SPECT with stationary detectors

This chapter is adapted from:
Yuan Chen, Marlies C. Goorden, Brendan Vastenhouw, Freek J. Beekman. *Optimized sampling for high resolution multi-pinhole brain SPECT with stationary detectors*, Phys. Med. Biol. **65** (2020) 015002 [70]

Brain perfusion SPECT can be used in the diagnosis of various neurologic or psychiatric disorders, e.g., stroke, epilepsy, dementia and posttraumatic stress disorder. As traditional SPECT provides limited resolution and sensitivity, we recently proposed a high resolution focusing multi-pinhole clinical SPECT scanner dubbed G-SPECT-I (Beekman et al 2015, *Eur. J. Nucl. Med. Mol. Imaging* 42 S209). G-SPECT-I achieves data completeness in the scan region of interest (ROI) by making small translations of the patient bed while using projections from all bed positions together for image reconstruction. A strategy to restrict the number of bed translations is desired to minimize overhead time. Previously we presented optimized bed translation paths for focused partial brain imaging, while here we focus on whole brain imaging which is the common procedure in perfusion studies. Thus, a series of noise-free scans using a reduced number of bed positions were simulated and compared to an oversampled reference scan acquired with 128 bed positions. Noisy simulations were included to validate the utility of the optimized sequences in more realistic situations. Brain uptake ratios (BURs) and left–right Asymmetry Indices (AIs) in 51 selected regions of interest (ROIs) were calculated for assessment. Results show that images were barely affected by decreasing the number of bed positions from 128 down to 18 (mean deviation from the reference of only 2.2% and 1.5% for the BUR and AI, respectively) while slightly larger deviations (2.9% and 2.7%, respectively) were obtained when using 12 positions. For both 18- and 12-position sequences these deviations due to sampling were much smaller than those induced by noise (mean deviation of 6.5% and 8.6%, respectively). Given an associated total overhead for bed movement of half a minute (18 positions) or 20 s (12 positions), G-SPECT-I can be a clinical platform that brings new protocols for fast (dynamic) whole brain SPECT and motion correction into reach.

3.1. Introduction

Brain SPECT with ^{99m}Tc, e.g. with ^{99m}Tc-HMPAO or ^{99m}Tc-ECD, has a widely demonstrated utility in detecting regional cerebral blood flow and in indirectly measuring neuronal activity. This enables the noninvasive assessment of cerebrovascular disease (e.g. stroke) and neurological dysfunction (e.g. epilepsy, dementias) [71, 72]. In particular, SPECT is the only imaging modality practically capable to perform an ictal scan during epileptic seizures due to the 'snapshot' property of the tracers in use [73, 74]. Besides these clinically well-established applications, additional indications in the psychiatric domain are currently under active evaluation [75–77], for example in post-traumatic stress disorder, anxiety and depression [78, 79].

Presently general purpose single-, dual- or triple-head SPECT scanners provide a limited spatial resolution of 7–10 mm, with sensitivity in the range of 100–250 cps/MBq. Some dedicated brain SPECT scanners, e.g. CeraSPECT, inSpira HD or NeuroFocus [41, 43, 80, 81], have been developed, but resolutions are still around 7 mm and some are not manufactured anymore. Such a limited resolution hampers detection of small localized perfusion abnormalities which can compromise accuracy of diagnosis and early detec-

tion of neuropathology while a low sensitivity requires a relatively high tracer dose and long scanning time resulting in patient discomfort as well as increased risk of motion artefacts. These limited resolution-sensitivity tradeoffs of previous SPECT scanners are due to the conventional collimator designs, a limited number of detectors or restricted detector surface area, lack of image magnification, etc.

Recently, efforts have been made to develop brain SPECT systems based on multi-pinhole collimation owing to its enhanced resolution-sensitivity tradeoff especially when imaging small objects. Simulation studies have been carried out to optimize multi-pinhole systems [10, 12, 13, 46, 47], however only a few systems have been built and/or acquired physical scans [10, 34]. Our group initially developed various focused multi-pinhole SPECT systems for preclinical purposes, e.g. U-SPECT-I, U-SPECT-II, VECTor, U-SPECT+ [50, 57, 64, 65], and lately this technology was translated in a prototype system named G-SPECT-I for clinical applications [10]. The preclinical systems achieve sub-halfmillimeter SPECT resolution and sub-second-frame dynamic scans for small animals [7, 50, 82] and are now in use in labs worldwide. The G-SPECT-I system offers an unprecedented resolution down to 2.5 mm and a sensitivity of 415 cps/MBq in scans of human head sized phantoms when a collimator with 3-mm-diameter pinholes is used [10]. These enhanced resolution-sensitivity tradeoffs are facilitated by the systems' design in which all pinholes are focusing on a central volume. This central volume is termed the complete data volume (CDV). For a scan of an object larger than the CDV, the bed is translated in order to extend the volume with ensured sufficient angular sampling. Subsequently, all pinhole projections from all bed positions together are used for image reconstruction of the entire volume using the scanning focus method [49].

Recently, we showed that scans of a region which contains a limited number of transaxial slices of the brain (up to 36 mm) can be performed by G-SPECT-I using only 4 bed translations, demanding an estimated overhead time of seconds and thus allowing for very fast dynamic imaging [27]. The present paper aims to optimize bed translations of G-SPECT-I for full brain scanning, which is commonly done in brain perfusion studies. To maximize effective sensitivity, scanning speed as well as 4D SPECT frame rate, we investigated (i) confining the axial length to the minimum required, and (ii) limiting the number of bed translations while avoiding truncation artifacts or undersampling, all based on extensive G-SPECT-I simulations including attenuation modeling. Resulting images were assessed both visually and quantitatively.

3.2. Methods

3.2.1. System design

The G-SPECT-I scanner (Figure 3.1) consists of nine scintillation gamma detectors each comprised of a $595 \times 472 \times 9.5$ mm^3 NaI(Tl) crystal based cameras, an interchangeable

collimator, a precisely controlled xyz-stage for bed translation, three optical cameras and an appropriate user interface for the selection of the scanning volume of interest (VOI) based on the optical cameras [56, 83]. The collimator assumed in this paper for brain imaging has a total of 54 pinholes [10]. All pinholes are focusing towards the collimator's center, offering a CDV with a transaxial diameter and axial length of 100 mm and 60 mm, respectively. Note that for activity in the large volume of the gantry outside the CDV, the emitted photons are still captured by a part of the pinholes (see Figure 3.1). Other details concerning the G-SPECT-I system have been explained in [27].

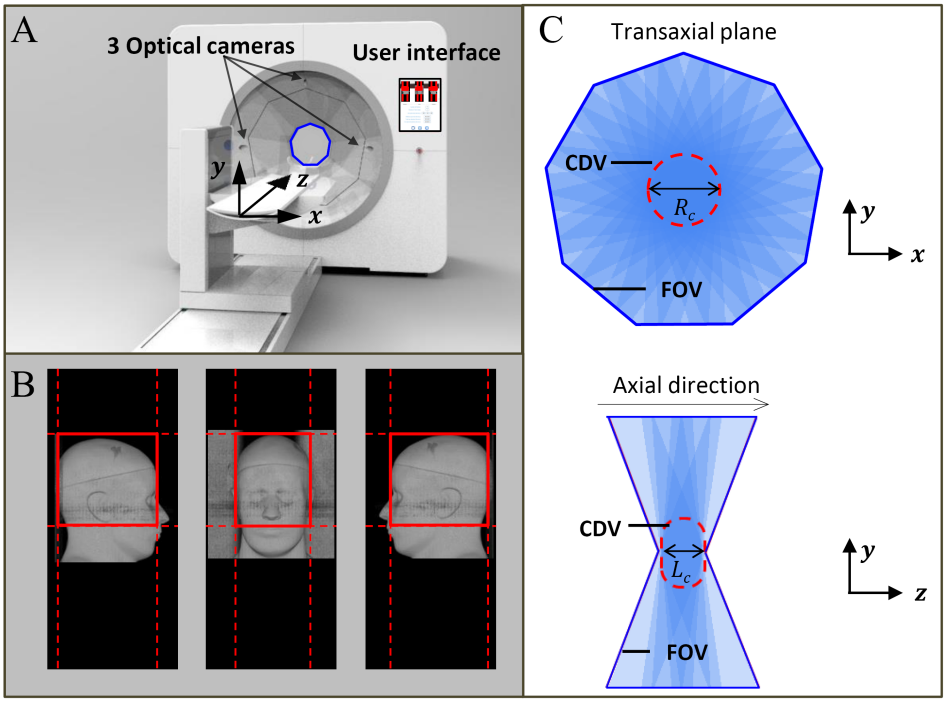

Figure 3.1: Illustration of the G-SPECT-I scanner. (A) G-SPECT-I system with three optical cameras and a user interface for VOI selection; (B) an example of how VOI selection is done with the user interface. The user interface takes the images from three optical cameras as input. (C) The CDV in transaxial view (top image) and along axial direction (bottom image). The CDV is the volume 'seen' by all pinholes; it has a transaxial diameter R_c of 100 mm and an axial length L_c of 60 mm. The entire field of view (FOV) of the scanner, at one bed position, is much larger than the CDV; it extends over the gantry as shown in the figure.

3.2.2. Simulation set up

A digital Zubal phantom [84] was used for simulating normal brain perfusion images (Figure 3.2). The activity map was generated by segmenting the Zubal phantom into grey matter, white matter and cerebral spinal fluid (CSF) and assigning activity concentrations to these regions with a ratio of 4:1:0, respectively, as in [85–87]. We forced the phantom

to be perfectly symmetric by mirroring the phantom left hemisphere to the right. This was to avoid any bias induced by the intrinsic left–right asymmetry of the Zubal phantom during image analysis. This phantom was subsequently interpolated (trilinearly) in PMOD v4.0 (PMOD Technologies Ltd, Switzerland) from its original size of $1.1 \times 1.1 \times 1.4$ mm^3 to $0.75 \times 0.75 \times 0.75$ mm^3 voxel size, half the voxel size of the reconstructed image ($1.5 \times 1.5 \times 1.5$ mm^3), to mimic a continuous activity distribution reconstructed on a discrete grid. System matrices for forward projection of the activity distribution and reconstruction were both generated using a set of ^{99m}Tc (140 keV) point source measurements and geometrical modeling [63]. To obtain realistic simulated projections, effects of attenuation were included using a voxelized ray tracer [17, 68]. Attenuation map were obtained by assigning regions in the Zubal phantom to bone, soft tissue and air with an attenuation coefficient of 0.31, 0.15 and 0 cm^{-1}, respectively (Figure 3.2(C)). Although attenuation was included in simulating projections, no attenuation correction was performed on the reconstructed images. Similarity regulated OSEM [18] with eight subsets and ten iterations was performed using the scanning focus method [49] to combine all projections from all bed positions simultaneously into image reconstruction.

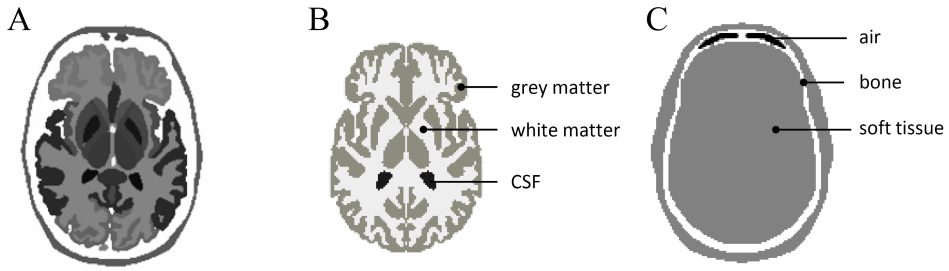

Figure 3.2: Phantoms used for brain perfusion simulation: (A) the Zubal phantom, (B) activity distribution in phantom, and (C) attenuation map. Tracer concentration in grey matter, white matter and CSF is set to be 4:1:0. Attenuation coefficients assigned to bone, soft tissue and air are 0.31, 0.15 and 0 cm^{-1}, respectively.

3.2.3. Noise-free simulations for bed sequence optimization

Bed sequence optimization was performed using noise-free simulations to quantify errors solely induced by sampling. Sequences investigated here all follow a multi-planar trajectory, meaning that bed positions in each transaxial plane are replicated along axial direction to extend the scan length. To serve as a reference, we first simulated an oversampled full brain scan obtained by (i) scanning the full axial length of the brain; (ii) keeping a small separation (compared to the 60 mm length of the CDV) of 21 mm between consecutive axial positions; and (iii) using a large number of 16 bed positions in each transaxial plane. This reference scan thus employs a total number of 128 small bed translations (8 axial and 16 transaxial positions).

Subsequently, to optimize the bed translation path, a series of scans using a reduced number of bed positions were simulated and compared to the reference scan. This opti-

mization was done according to the following three steps (see also Figure 3.3).

1. Confine the axial scan length by searching the maximum allowed edge margin D_{em} that still allows for artifact-free whole brain imaging.
2. Maximize the separation D_{sp} between consecutive axial positions to facilitate a minimum number of axial positions.
3. Further minimize the required number of transaxial positions per plane N_{tr} , using the optimal settings found in the previous steps.

Each step is explained in detail in the subsections below.

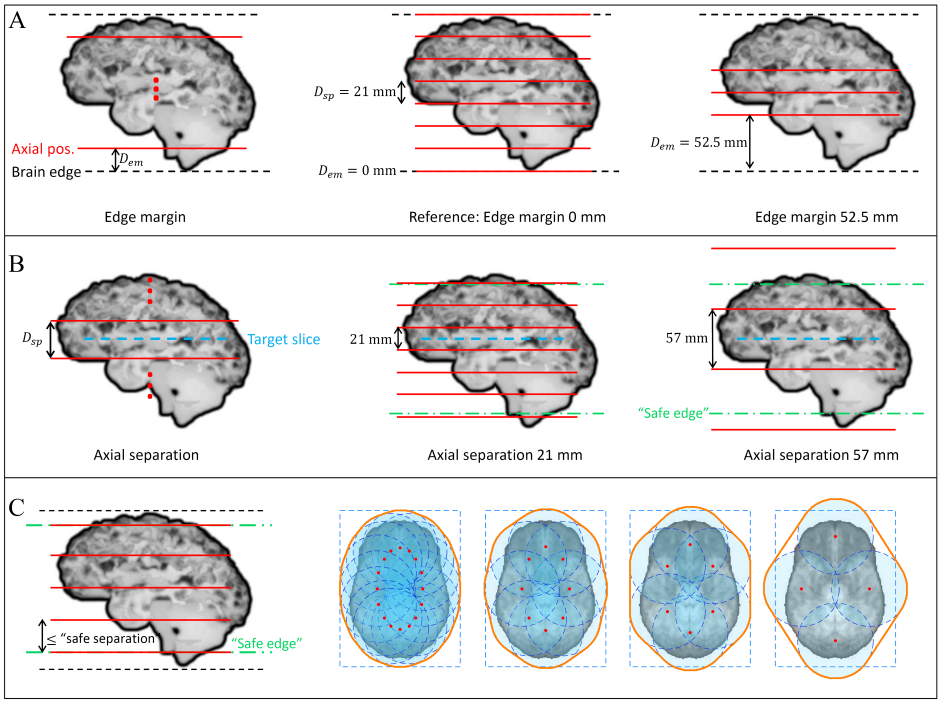

Figure 3.3: Illustration of the bed sequence optimization for (A) edge margin D_{em}, (B) axial separation D_{sp}, and (C) number of transaxial bed positions N_{tr} . The brain image shown represents a maximum intensity projection of the brain perfusion phantom in the coronal view. In (A), oversampling in the brain between the first and last sampling planes is always ensured by using a safe D_{sp} of 21 mm and a N_{tr} of 16. In (B), bed positions are added until at least the 'safe' edge found in step (A). In (C) the left figure illustrates the final axial position placement, based on the results of the optimal D_{em} and D_{sp}. With this axial placement, sampling sequences with a N_{tr} of 16, 8, 6 and 4 are tested which are displayed at the right. The red dots highlight the transaxial bed positions, and the blue circles indicate the outer contours of the CDVs. The dashed blue box denotes the selected VOI on the transaxial plane. The convex hull of the CDVs, in which complete data is obtained, is represented by the orange line.

Axial edge margin D_{em}

To find the maximum 'safe' edge margin D_{em}, we gradually increased D_{em} from 0 mm (reference scan) to 10.5 mm, 21 mm, 31.5 mm, 42 mm, 52.5 mm (as shown in Figure 3.3A which illustrates the two extreme cases). Oversampling in the region between the first and last sampling plane was always ensured by using a small D_{sp} of 21 mm and 16 bed positions in the transaxial plane, the same settings as used for the reference scan.

Axial separation between consecutive positions D_{sp}

The optimal axial separation was investigated by gradually increasing the value of D_{sp} from 21 mm up to 60 mm (the length of the CDV). To have a fair comparison among scans with different D_{sp}, a target slice was adopted, around which axial positions were placed symmetrically (see Figure 3.3B). Here the value of D_{sp} was set to be 21 mm, 30 mm, 39 mm, 48 mm and 57 mm (increasing at a multiple of 2×1.5 mm for the symmetric placement).The target slice was placed at the center of the thalamus, which contains rich perfusion patterns and involves multiple important subcortical structures (e.g. caudate, putamen). We regard this slice to be the most 'problematic' for all sequences since it locates exactly in between two sampling planes in all cases. Meanwhile, for all scans with different axial separations it was ensured that the axial length was sufficiently long. In principle, this could be accomplished by placing the first/last axial position at a common top/bottom edge margin (e.g. all at the 'safe edge' found in the previous step) and adding axial positions in between. However, this greatly limits the choice for D_{sp}. Therefore, in this study axial bed positions with a designated separation were added until at least the 'safe' edge margin (Figure 3.3B).

Transaxial positions N_{tr}

The findings in the aforementioned axial placement step were used as a starting point to further optimize sequence design in the transaxial plane. We kept D_{em} at the maximum 'safe' edge margin while making sure that D_{sp} was not larger than the 'safe' axial separation (see Figure 3.3C) and we gradually decreased the number of transaxial positions. The design of all transaxial bed sequences was based on the previously proposed protocol described in [27], which assumes that a VOI is selected in the transaxial plane based on the subject's head contour which could be done using the G-SPECT-I user interface (Figure 3.1B). A sequence was then designed based on the selected VOI and a transaxial data-completeness model which ensures sampling sufficiency in the convex hull surrounding the CDVs [27]. An illustration of the designed transaxial sequences for a G-SPECT-I brain perfusion scan based on this protocol is displayed in Figure 3.3C; from an oversampled sequence using 16 bed positions per transaxial plane, to sequences using 8, 6 and 4 bed positions per plane.

3.2.4. Noisy simulations

To place the sampling-induced deviations in the context of image variations due to statistical uncertainty caused by the limited number of detected photons, we additionally performed reconstructions with noisy projection data (for 20 Poisson noise realizations based on the noiseless projections). This was done for the reference sequence as well as for a selected number of sequences with reduced number of bed positions. These noisy simulations assumed a total of 50 MBq of ^{99m}Tc in the brain [88–90] and were representative for a scan time of 30 min.

3.2.5. Evaluation

Assessment of the simulated perfusion scans was performed by visual inspection and quantitative ROI analysis. The latter was achieved by calculating the BUR and the asymmetry index (AI) in selected ROIs. These two metrics are given by

$$BUR = \frac{C_{target}}{C_{background}} \tag{3.1}$$

$$AI = \frac{C_{R-target} - C_{L-target}}{C_{R-target} + C_{L-target}} \times 200\% \tag{3.2}$$

Here C_{target} and $C_{background}$ denote the mean uptake value in the target and background ROI, respectively. In this work the entire cerebellum (Figure 3.4F) directly segmented from the Zubal phantom was used as the background region. The mean uptake value $C_{R-target}$ is the measurement from the ROI in the right hemisphere while $C_{L-target}$ is that of the corresponding ROI in the left hemisphere.

Varied ways of target ROI definition are used for perfusion SPECT assessment across studies. One of the common approaches entails manually delineating ROIs in the four big lobes (i.e. frontal, temporal, parietal and occipital lobe), sub-regions of the lobes (e.g. inferior and superior frontal lobe, lateral and medial temporal lobe, etc), and/or in subcortical structures (e.g. cingulate, thalamus, etc) [91–95]. Besides, automated methods -which could reduce labor and variability compared to manual ROI placements- are often performed by registering subject scans to a template (e.g. an averaged scan from databases) or an atlas (e.g. Talairach atlas). However, this generally requires subject MR scans, templates with already segmented ROIs, etc, while displacement due to misregistration, possibly a few mm [96, 97], could bring bias/errors for quantification on the simulated high resolution images. In addition, some studies implement 'polar maps' to generate ROIs by simple image processing on subject SPECT scans. The polar map delineates regions along the periphery of the brain in the transaxial plane covering most of the grey matter, where manually drawn ROIs are often placed. The latter approach of ROI

definition was implemented in our work. Meanwhile, we also incorporated some ROIs from subcortical structures and in the coronal plane to make the measurement more comprehensive as they have also been used in literature [92, 95].

A total number of 51 target ROIs was used (see Figure 3.4), among which 36 ROIs were placed in three transaxial planes, 9 ROIs in two coronal planes and 6 subcortical ROIs (caudate, putamen and thalamus in both hemispheres) were directly segmented from the 3D Zubal phantom. For the transaxial slices, an inferior (Figure 3.4A) and a superior (Figure 3.4C) slice were placed at the center of the thalamus and tangential to the cingulate, respectively, as in [98, 99]. A middle slice (Figure 3.4B) was chosen to be the slice exactly in between the two. To generate the polar map regions on the transaxial slice, an annulus region was obtained by segmenting the brain outer boundary from the digital phantom and extending it from the outer boundary inwards for 15 mm, as in [100, 101]. This annulus was subsequently divided into 12 equal angular sectors. For ROIs in the coronal plane, the orbital and dorsolateral part of the frontal lobe and cingulate (Figure 3.4D), as well as the mesial and lateral part of the temporal lobe (Figure 3.4E) were considered, as in [99]. These transaxial and coronal ROIs have a size in the range of 0.4–1.0 cm^3 with a mean value of 0.8 cm^3. The subcortical ROIs (as displayed in Figure 3.4A on one transaxial slice) vary in size from 4.4–5.7 cm^3. Figure 3.4F illustrates the location of the selected transaxial and coronal planes as well as the cerebellum in the brain.

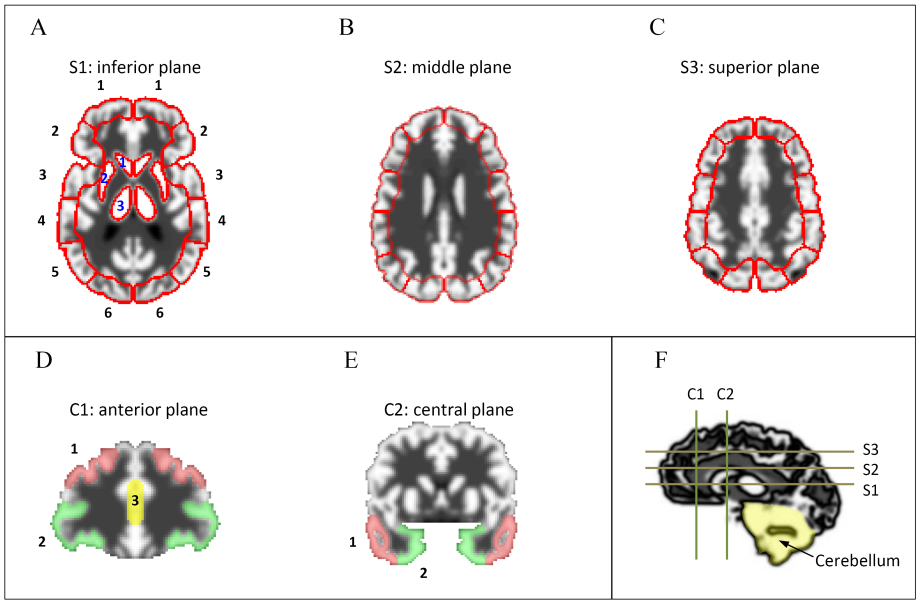

Figure 3.4: Illustration of the 51 target ROIs for quantitative analysis. Panels (A)–(C) show ROIs in three transaxial slices. Panels (D) and (E) display the ROIs in two coronal slices. Panel F indicates the location of the selected transaxial or coronal slices in the brain. In each transaxial slice, 12 peripheral ROIs are segmented symmetrically on the left and right hemisphere. The subcortical regions in the inferior plane are depicted in panel (A).

For each simulated scan, its BUR and AI values in all 51 ROIs were calculated and compared to those from the (noise-free) reference scan. We assessed the magnitude of the deviations from this reference scan when scanning with various bed sequences. These deviations are defined as:

$$DevBUR = \frac{\mid BUR - BUR_{ref} \mid}{BUR_{ref}} \times 100\% \tag{3.3}$$

$$DevAI = \mid AI - AI_{ref} \mid \tag{3.4}$$

Here Dev stand for the deviation from the reference scan, while BUR_{ref} and AI_{ref} are the BUR and AI values of the reference. The deviation of AI is calculated directly by subtracting the AI_{ref} , since AI is already a normalized index expressed in percentage. Note that the BURs are always positive (Equation 3.1) and AIs here could be either positive or negative (Equation 3.2).

For all images presented in this paper, the noise-free scans were post filtered with a 3D Gaussian filter of 4 mm full width at half maximum (FWHM) and displayed with a slice thickness of 1.5 mm. The noisy scans were 6 mm-FWHM Gaussian filtered and displayed with a larger slice thickness of 6 mm to suppress small local fluctuations due to noise. For quantitative analysis of all scans, measurements were performed on the unfiltered images to avoid any bias from filtering. Additionally, we included some quantitative results obtained from 6-mm-FWHM Gaussian filtered images for a selected number of scans, since quantification of clinical SPECT is commonly performed on filtered images.

3.3. Results

3.3.1. Noise-free simulations

Axial edge margin D_{em}

Figure 3.5(A) shows the sagittal view of simulated perfusion images with an increasing edge margin D_{em}. The red lines indicate the locations of the first/last axial bed positions while the dotted white lines denote the upper/bottom edge of the brain. Compared to the reference scan (with D_{em} = 0 mm), scans with a D_{em} up to 31.5 mm appear hardly degraded upon visual inspection while further increasing D_{em} to 42 mm or 52.5 mm results in some artefacts at the edges of the brain. For an additional check, a top and a bottom transaxial slice are selected and displayed in Figure 3.5B. Image profiles on these two transaxial slices are displayed in Figure 3.5C. Figure 3.5 confirms the sufficient coverage of the brain for scans with a maximum D_{em} of 31.5 mm as structures in the top or bottom transaxial slices are well preserved compared to the reference scan.

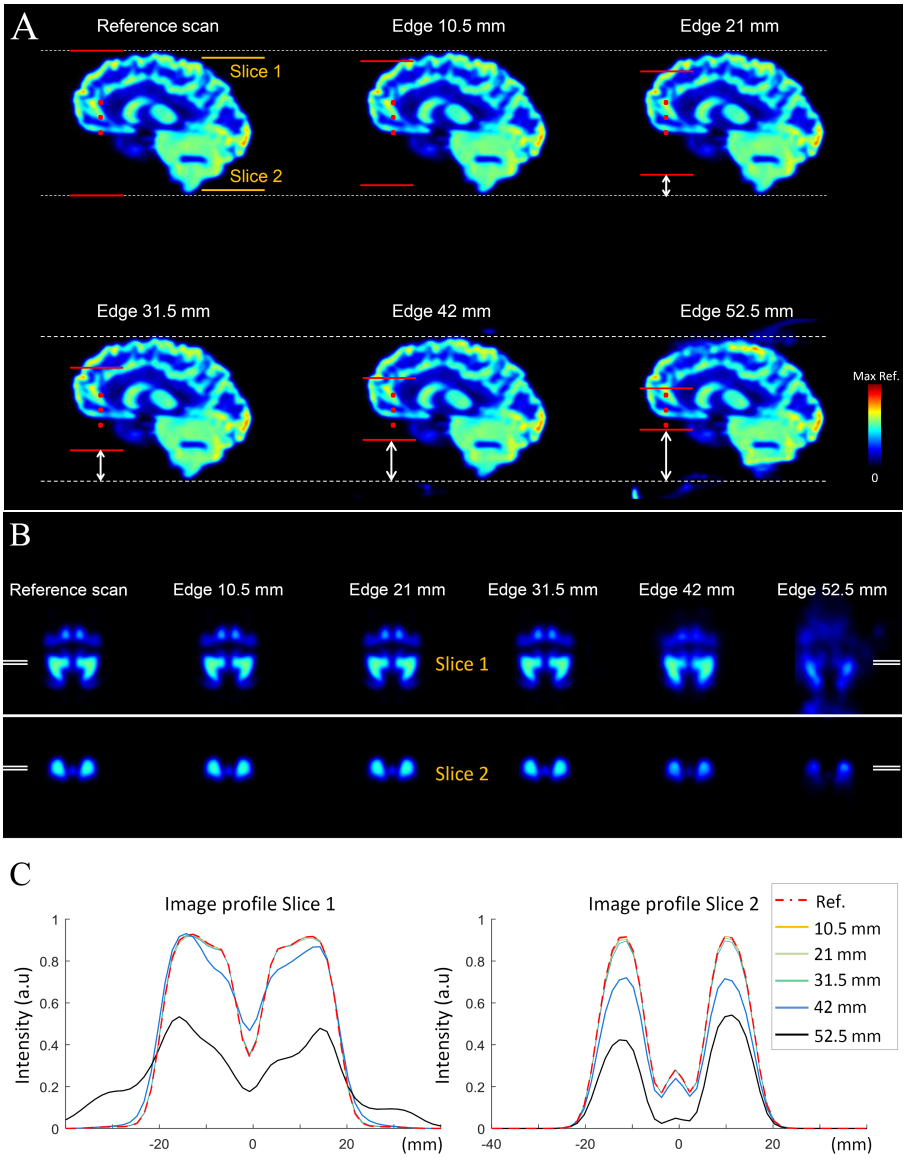

Figure 3.5: Comparison of scans with different edge margin D_{em}. (A) Simulated sagittal image slices are displayed. The red lines indicate the locations of the first/last axial bed positions and the dotted white lines denote the upper/bottom edge of the brain. The same colormap ranging from 0 to the maximum intensity of the reference scan is used for all simulated perfusion images in this paper. (B) A top and bottom transaxial slice are displayed. The locations of these two slices are indicated in panel (A). Image profiles through each transaxial slice are included and shown in panel (C). These profiles are taken from a line with a width and thickness of 4.5 mm.

Axial separation D_{sp} between consecutive sampling planes

To compare the scans with different D_{sp}, the target slice (which always locates exactly in between two sampling planes) as well as image profiles are shown in Figure 3.6 A and B, respectively for all sequences. Figure 3.6 shows that visual differences between the simulated images acquired with varied values of D_{sp} are small; patterns are well preserved with no obvious distortions even for a value of D_{sp} of 57 mm. This is further confirmed by the coronal view comparison in Figure 3.11 in the appendix.

To quantitatively assess the effect of increasing D_{sp}, we calculated brain uptake ratio BUR for the 12 polar map regions on the target slice (Figure 3.7A). Compared to the reference image, scanning with an increased value of D_{sp} up to 57 mm achieves comparable BUR measurements (maximal deviation of 6.0% from the reference) among all selected ROIs on the target slice.

Besides a direct comparison of the BURs on the target slice, deviations from the reference scan among all 51 ROIs in the entire brain are calculated and displayed in Figure 3.7B. Due to the large number of ROIs assessed, only the maximum and mean deviation from all ROIs are plotted. Figure 3.7B demonstrates that deviations from the reference for the tested scans acquired with different D_{sp} are all below 7%. For the scan with a D_{sp} of 48 mm, the BUR and AI deviate maximally 5.0% and 3.2%, respectively, while the mean deviations read only 1.3% and 0.8%. Based on these visual and quantitative results (Figure 3.6-3.7), a maximum axial separation D_{sp} of 48 mm is used for further transaxial sequence optimization.

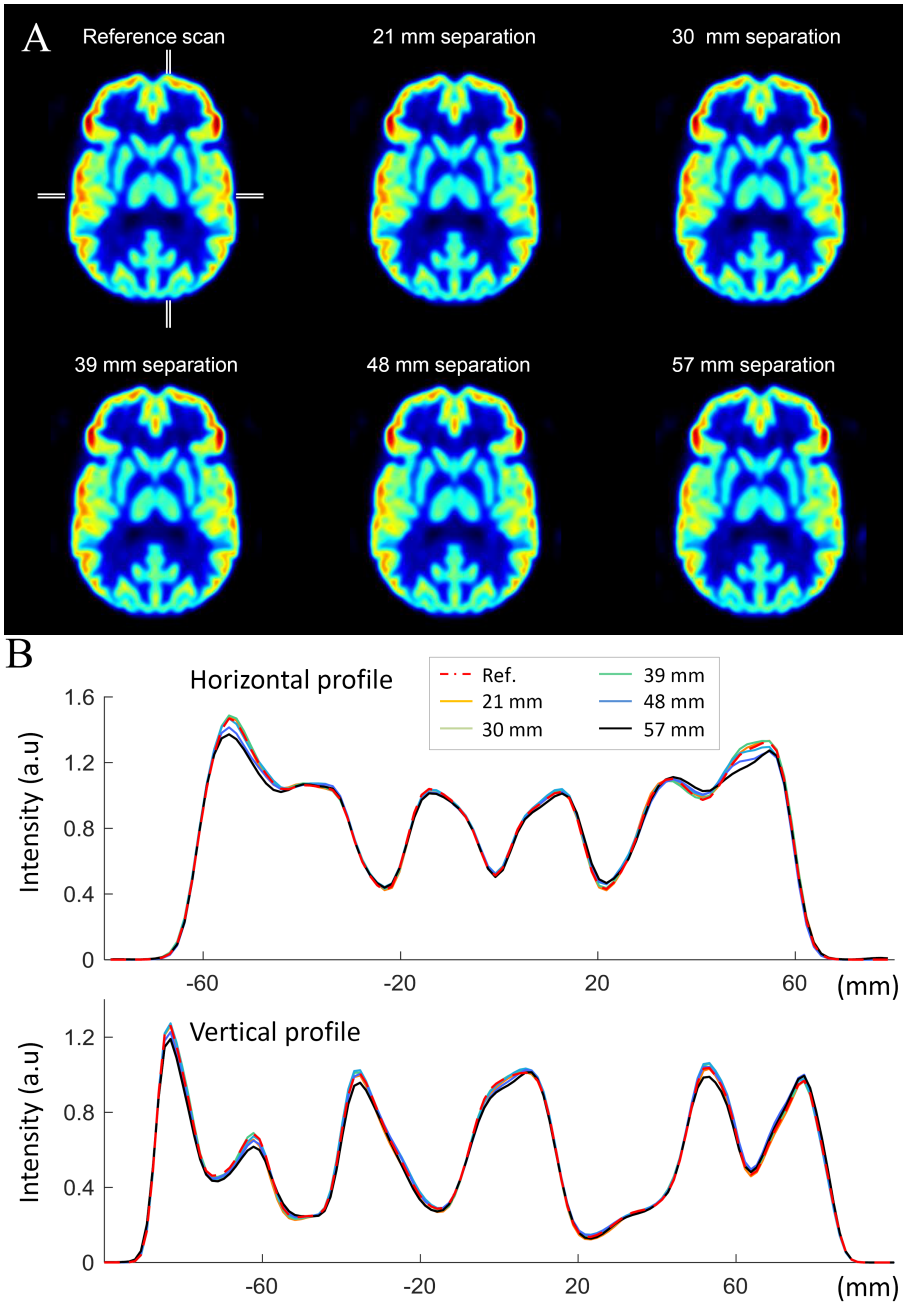

Figure 3.6: Comparison of the target slice for scans with different axial separations. (A) The target slice is displayed for different scan sequences. (B) A horizontal and a vertical image profile through the target slice are shown. These profiles are taken from a line with a width and thickness of 4.5 mm. Note that the reference scan is simulated using an axial separation of 21 mm and covers the entire brain using 8 axial positions (see Figure 3.3A), while the middle image on the first row of panel A (21 mm separation) is simulated with an axial separation of 21 mm and sufficient axial bed positions (5 in this case) are added to reach the safe edge margin of 31.5 mm.

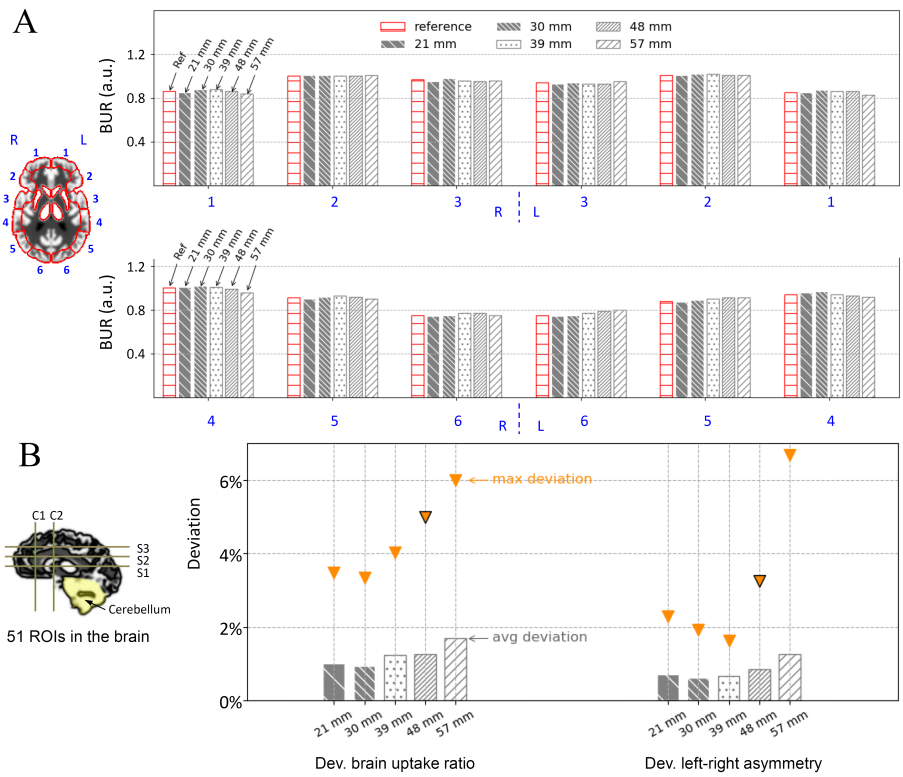

Figure 3.7: Comparison of the BUR and AI measurements between the reference and scans with an increased axial separation D_{sp}. (A) Direct comparison of the BURs for the tested sequences in ROIs on the target slice; (B) deviations from the reference of the BUR and AI among all 51 ROIs (see Figure 3.4) in the entire brain. The maximum and average deviation are shown with a triangle and a bar, respectively.

Transaxial sampling sequence

Figure 3.8 shows a comparison of scans with different numbers of transaxial bed positions N_{tr} . All scans (except the oversampled reference) use the same axial bed position placement (Figure 3.8A) based on the previous results (optimal D_{em} and D_{sp}) and adjusted to the size of Zubal phantom; we keep D_{em} to be 31.5 mm while adding axial positions such that D_{sp} is not larger than 48 mm (42 mm here). Figure 3.8A shows two transaxial slices which are both in between two sampling planes, while Figure 3.8B gives a comprehensive comparison of the transaxial images from the top to the bottom of the brain. Additionally, as other views are also important for perfusion scan assessment, we include more image comparisons for the coronal view in the appendix (Figure 3.12). Both the transaxial and coronal view results show that reducing the number of bed positions from the oversampled reference scan to 18 (3 axial positions combined with 6 transaxial positions) hardly has a visual effect on perfusion images. Further decreasing the number of transaxial bed positions to 4 leads to relatively larger deviations from the reference as well as a slightly degraded left–right symmetry.

A quantitative analysis is included in Figure 3.9 which shows a direct comparison of the BURs for the 12 polar map ROIs on the target slice (Figure 3.9A), as well as the maximum and average deviations in BUR and AI from the reference among all 51 ROIs (Figure 3.9B). For all the tested transaxial sequences, these deviations are below 9.8%. When using six transaxial positions with the proposed axial placement, the maximum deviation of the two measurements are 5.7% and 5.4% for BUR and AI, respectively, while the mean deviations read only 2.2% and 1.5%. Further decreasing the number of transaxial positions to 4 leads to a maximum deviation of 8.1% and 9.8% for the BUR and AI, respectively, and a mean deviation of 2.9% and 2.7%, respectively.

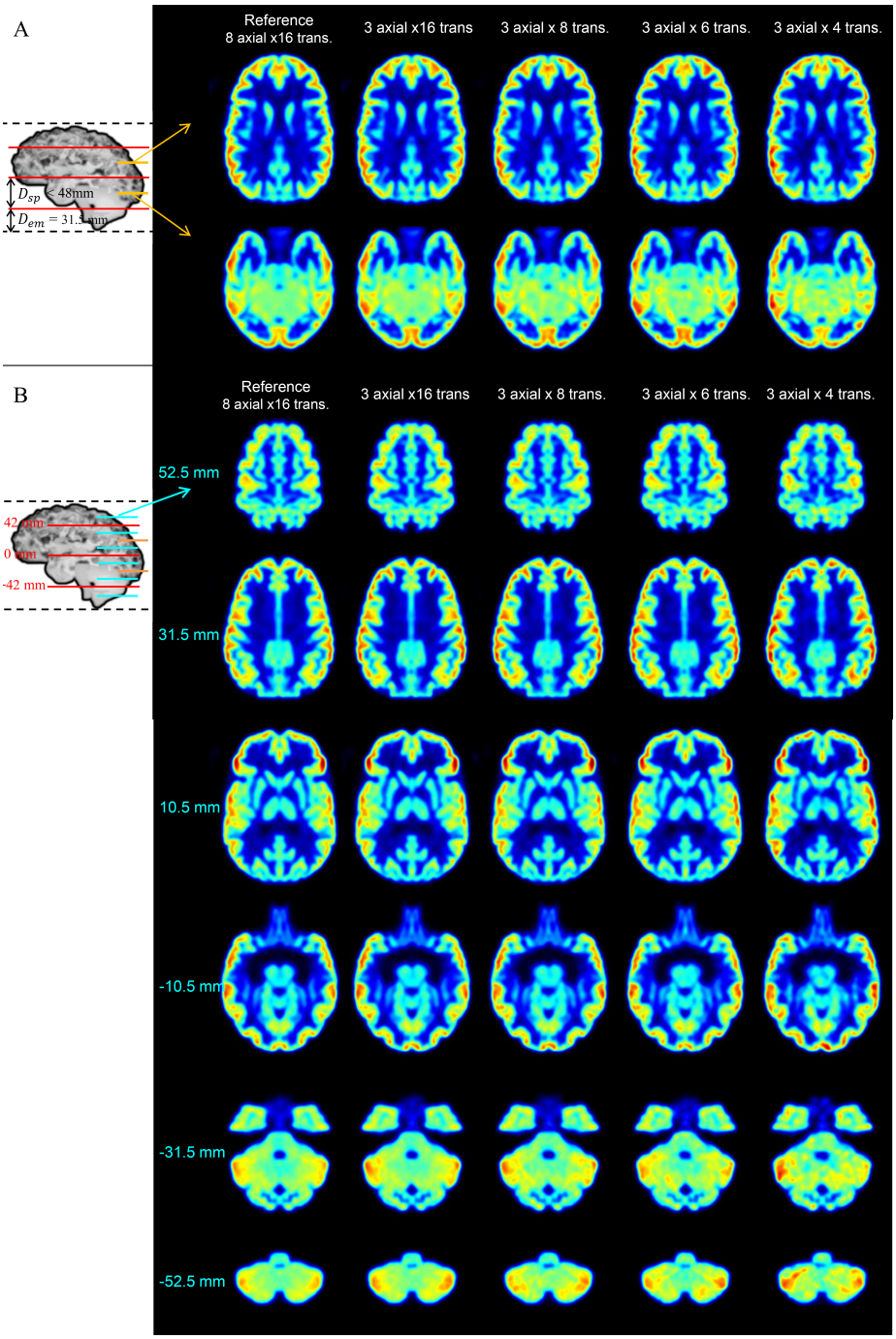

Figure 3.8: Comparison between the reference scan and scans with different transaxial bed positions. (A) Two transaxial slices which are both exactly in between two sampling planes; (B) transaxial slices from top to the bottom of the brain.

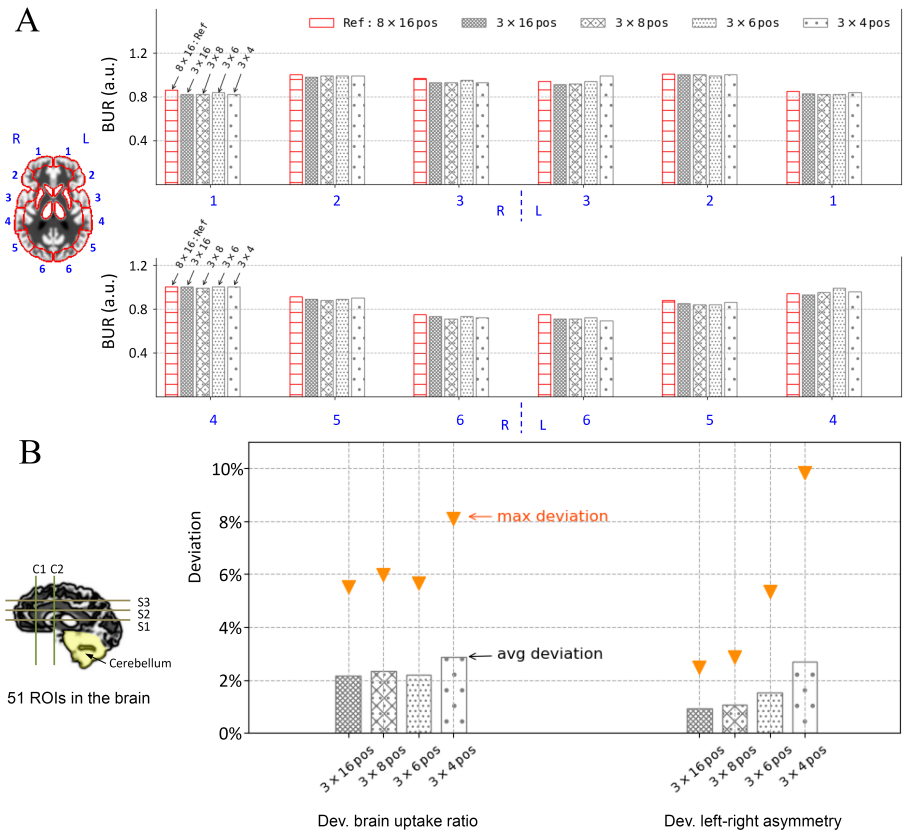

Figure 3.9: Comparison of the BUR and AI measurements between the reference and several scans each using 3 axial positions but with different numbers of transaxial bed position N_{tr}. (A) Direct comparison of the BURs for the tested sequences in ROIs on the target slice; (B) deviations from the reference of the BUR and AI among all 51 ROIs (see Figure 3.4) in the entire brain. The maximum and mean deviation are shown with a triangle and a bar respectively.

3.3.2. Noisy simulations

Noisy simulations were performed for the reference sequence (Noisy-ref) as well as for two selected sequences based on the results above, i.e. the sequence with 18 (Noisy-18: 3 × 6 positions) and 12 positions (Noisy-12: 3 × 4 positions). Examples of the simulated noisy images are shown in Figure 3.10A.

Quantitative assessment of the BUR and AI deviations from the (noise-free) reference scan are provided in Figure 3.10B. This figure shows that deviations due to Poisson noise are 3–4 times larger than those induced by sampling; for example, reducing the number of bed positions to 18 or 12 positions leads to a mean (BUR or AI) deviation from the reference in the range of only 1.5%–2.9% when assessed on unfiltered images, while these two mean deviations (BUR and AI) for Noisy-ref are 6.5% and 8.6%, respectively. Using a post filter (6-mm-FWHM Gaussian) either on noise-free or noisy scans could reduce the quantification error typically by a factor of 1.5–2. For example, the sampling induced BUR or AI deviations (with 18 or 12 positions) decrease to mean values of 0.7%–1.9% when images are filtered, while for the Noisy-ref scans the mean deviation decreases to 4.2% and 2.5% for BUR and AI, respectively.

Compared to Noisy-ref, Noisy-18 achieves a slightly better performance, which could be explained by the increased count yield (1.2 times higher for the more focused 18-position sequence than for the reference sequence). Noisy-12 obtains a similar quantitative accuracy as Noisy-ref for unfiltered images, but slightly larger deviations (0.7% and 0.6% larger mean deviations for BUR and AI, respectively) when assessed on the filtered scans.

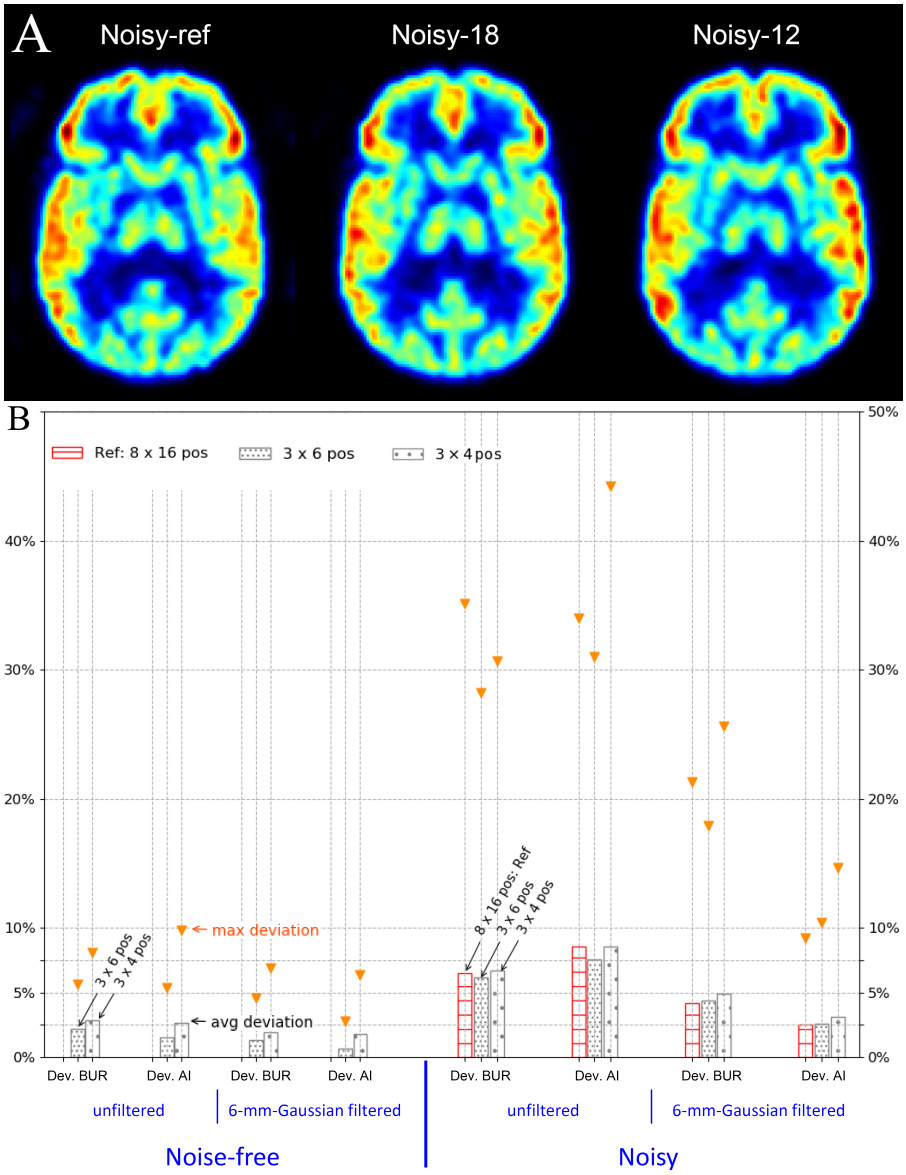

Figure 3.10: Comparison of the noisy simulations for the reference sequence (Noisy-ref) as well as for sequences with 18 (Noisy-18) and 12 positions (Noisy-12). Example of the simulated noisy scans are shown in panel A. Panel B shows the deviations from the (noise-free) reference scan for the noiseless and noisy unfiltered scans and for these scans applying a Gaussian filter of 6 mm FWHM. The maximum and mean deviation are shown with a triangle and a bar respectively. For the noisy simulations, the maximum and mean deviations were calculated from 51 ROIs and for all 20 noise realizations.

3.4. Discussion

A big challenge in clinical brain imaging is to achieve an excellent resolution-sensitivity tradeoff that allows for visualization of small lesions at a reasonable radiation dose, while fast (dynamic) capabilities that can be used in motion correction are advantageous as well. Previously we have demonstrated excellent resolution-sensitivity tradeoff of the G-SPECT-I scanner in physical phantom scans [10]. The current work presents G-SPECT-I acquisition using a limited number of bed translations that still allows artifact-free high resolution whole brain scanning. We estimated the total overhead time of 18 and 12 positions to be only 30 and 20 s, respectively (based on estimations involving the current G-SPECT-I prototype). This may enable fast dynamic studies and multi-frame scans for motion correction.

Note that with G-SPECT-I, overhead time is introduced by the bed translations required to scan volumes larger than the CDV, while for traditional SPECT overhead time is associated with the need to rotate the heads. For traditional scanners with step-and-shoot mode, 64 or 128 views are generally required for sufficient angular sampling (even for a small scanning volume), which results in more than 20 detector stops even for a triple-head system leading to an overhead time of 40–80 s assuming 2–4 s movement time per view, as reported in [102, 103]. Instead, the G-SPECT-I design with stationary detectors offers the flexibility of performing focused scans where only few bed translations are required while also allowing for extended volume scans.

Effects of attenuation were included in the simulation to make results more realistic. No attenuation correction was performed in the reconstruction for multiple reasons. Firstly, we have not yet determined the attenuation correction method (e.g. transmission imaging based, MR based using deep learning, solely SPECT based, etc) to be applied in future G-SPECT-I studies. This is currently under development [104] , however further testing and validation is necessary. Besides, there are clinicians do not use it [105], possibly because it can be prone to errors due to small shifts between SPECT and CT [106, 107] or because of the limited accuracy of a contour based uniform attenuation. Therefore we felt it was better to prevent mixing of the sampling issues with attenuation correction inaccuracies due to the use of a not fully validated approach for G-SPECT-I at this stage.

In this paper, we firstly performed noise-free simulations to constrain the analysis to sampling problems associated with different sequences, while later noisy simulations were included to investigate the utility of the optimized sequences in realistic noisy situations. The former step demonstrated that reconstructed images were barely affected (both visually and quantitatively) when the number of bed translations was decreased from 128 down to 18; when further decreasing the number of translations to 12, a somewhat larger deterioration from the reference scan (maximum deviation of 9.8%, see Figure 3.9) and some visual deviations (see Figure 3.8) were observed. This maximum deviation with the use of a 12-position sequence decreases to 6.9% when quantifications

were done on 6-mm-FWHM Gaussian filtered scans (Figure 3.10B). In addition, the noisy simulations showed that in the presence of noise, the deviations due to using 18-position or 12-position sequences are almost negligible (3–4 times smaller) compare to those induced by noise. Note that in the noisy simulations bed movement overhead time was neglected as it highly depends on the number of frames in data acquisition and the bed in use. Thus in practical SPECT scans when overhead time is playing a role, especially in multi-frames studies, one would expect a relatively larger benefit when using sequences with 18 and 12 positions than what is provided in Figure 3.10.

For focused scans when only a part of the brain is of interest, the number of bed translations can be further reduced without sacrificing image quality by axially restricting the scan length to just cover the target volume. An example of such an implementation was demonstrated in [27] which presented brain dopamine system imaging with only 4 bed translations. Besides, even for whole brain scans which require very high temporal resolutions, as in brain pharmacokinetic studies [108–111], utilizing less than 12 positions remains possible, for example by applying an axial separation D_{sp} larger than the currently used value of 48 mm. For such fast scans, the effects of noise would be much more prominent than what was shown in figure 10 such that the compromised accuracy due to sampling may be negligible. This could enable imaging tracers with a very short (biological or physical) half-life, such as ^{133}Xe (biological half-life of about 40 s), for which scanning with a confined axial length, e.g. 71 mm [112] is often already done.

Aspects which have not yet been studied here could enable even faster dynamic SPECT imaging. We have assumed the same number of transaxial positions at each axial position; in future work one could study using fewer transaxial positions when scanning parts of the brain with smaller dimensions, e.g. the brain's top and bottom. Besides, strategies that enable a continuous bed motion acquisition would be beneficial as in that case counts would constantly be recorded during the entire scan. Such methods have been proposed for PET imaging with bed translations only in axial direction [113–115]. For G-SPECT imaging this requires additional investigations. Moreover, collimators that offer a larger CDV are currently under design in our institute. With these developments, one can expect that less or even no bed translations are required, which may help to achieve extremely fast SPECT scans.

3.5. Conclusion

We have designed and evaluated different bed position sequences for total brain perfusion imaging with a stationary focusing multi-pinhole SPECT system. We found that decreasing the number of bed positions from 128 representing an oversampled scan down to a small number of 18 or 12 positions has minimal effects on image quantification compared to those induced by noise, while the respective overhead times were estimated to be only 30 and 20 s in total. This is important information for developing protocols for

fast dynamic brain SPECT and multi-frame scans for motion correction.

Appendix

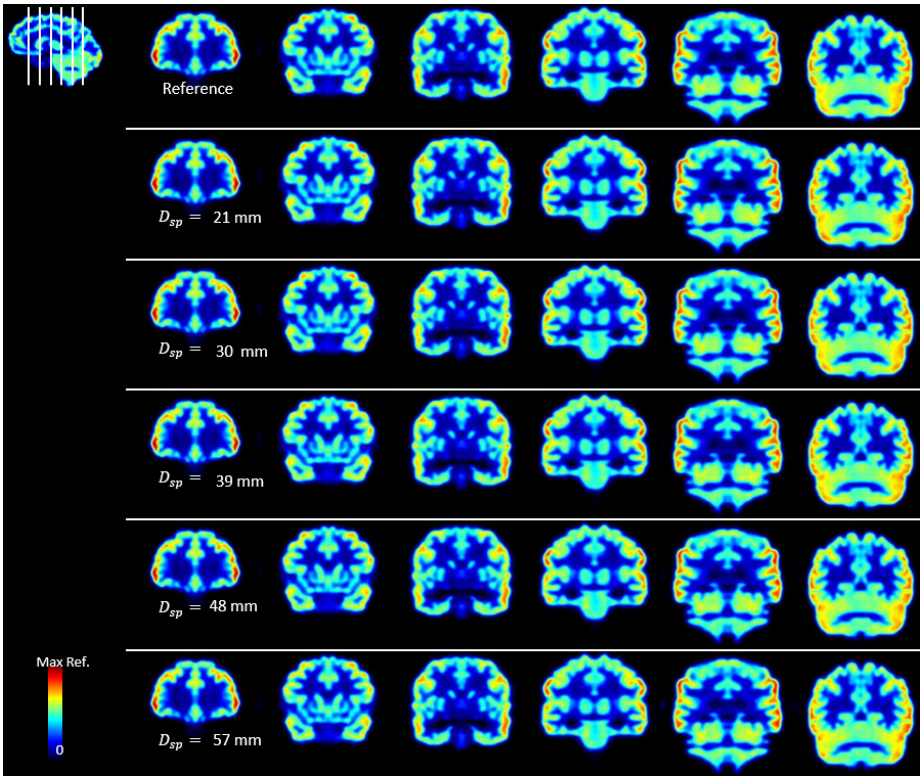

Figure 3.11: Comparison of simulated perfusion images with the reference image when increasing the axial separation between consecutive sampling planes D_{sp} images are shown in the coronal view. Each row corresponds to one simulated scan, with the D_{sp} increasing from 21 mm to 57 mm from the 2nd row to the bottom row. Images from left to right shows the coronal slices from the anterior of the brain to the posterior. The locations of the slices are indicated in the top left image.

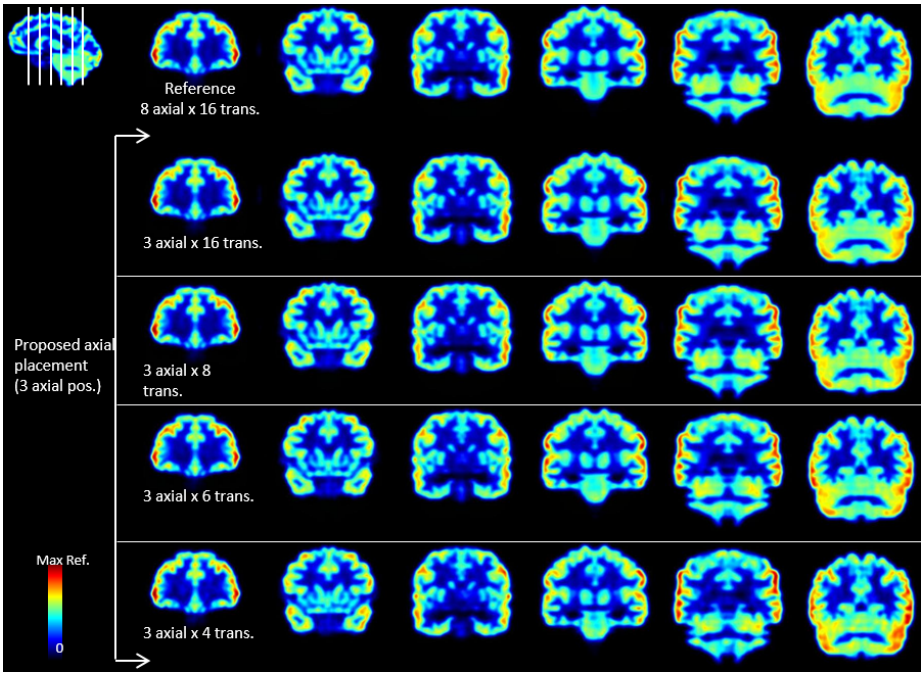

Figure 3.12: Comparison of simulated perfusion images with the reference image when using the proposed axial position placement but reducing the number of transaxial bed positions N_{tr}. Each row corresponds to one simulated scan, with the N_{tr} decreasing from 16 to 4 positions per plane from the 2nd row to the bottom row. Images from left to right shows the coronal slices from the anterior of the brain to the posterior. The locations of the slices are indicated in the top left image.

4

Automatic attenuation map estimation from SPECT data only for brain perfusion scans using convolutional neural networks

This chapter is adapted from:
Yuan Chen, Marlies C. Goorden Freek J. Beekman. *Automatic attenuation map estimation from SPECT data only for brain perfusion scans using convolutional neural networks*, Phys. Med. Biol. **66** (2021), 065006 [104]

In clinical brain SPECT, correction for photon attenuation in the patient is essential to obtain images which provide quantitative information on the regional activity concentration per unit volume (kBq.ml^{-1}). This correction generally requires an attenuation map (μ map) denoting the attenuation coefficient at each voxel which is often derived from a CT or MRI scan. However, such an additional scan is not always available and the method may suffer from registration errors. Therefore, we propose a SPECT-only-based strategy for μ map estimation that we apply to a stationary multi-pinhole clinical SPECT system (G-SPECT-I) for ^{99m}Tc-HMPAO brain perfusion imaging. The method is based on the use of a convolutional neural network (CNN) and was validated with Monte Carlo simulated scans. Data acquired in list mode was used to employ the energy information of both primary and scattered photons to obtain information about the tissue attenuation as much as possible. Multiple SPECT reconstructions were performed from different energy windows over a large energy range. Locally extracted 4D SPECT patches (three spatial plus one energy dimension) were used as input for the CNN which was trained to predict the attenuation coefficient of the corresponding central voxel of the patch. Results show that Attenuation Correction using the Ground Truth μ maps (GT-AC) or using the CNN estimated μ maps (CNN-AC) achieve comparable accuracy. This was confirmed by a visual assessment as well as a quantitative comparison; the mean deviation from the GT-AC when using the CNN-AC is within 1.8% for the standardized uptake values in all brain regions. Therefore, our results indicate that a CNN-based method can be an automatic and accurate tool for SPECT attenuation correction that is independent of attenuation data from other imaging modalities or human interpretations about head contours.

4.1. Introduction

In SPECT, attenuation of photons in tissue hampers quantitative analysis of regional tracer uptake and may lead to image artefacts. Attenuation correction (AC) is thus required to improve the diagnostic value and quantitative accuracy of reconstructed images. Besides, quantitative SPECT (i.e. SPECT that provides a precise estimate of the activity level in kBq.ml^{-1}) is also important for dosimetry planning [116].

Correction for photon attenuation is commonly based on a 3D map (attenuation map or μ map) that quantifies the amount of attenuation in each voxel within the patient at the given photon energy. Today, these μ maps are often derived from an additional CT or MRI scan. However, such an additional scan may not be available, can add radiation dose in case of CT, and is prone to registration errors [117–119]. Besides the use of additional CT or MRI scans, simple methods based solely on emission data that delineate the object contour and assume a uniform attenuation within the contour are used. Currently, manual placement of an ellipse approximating the head contour is still the most widely implemented approach for brain studies with commercial SPECT systems [120]. Such a method however can be highly subjective and suffer from limited accuracy due to the operator dependency, coarse approximation of the skull contour and lack of internal head

anatomy.

In clinical SPECT, photon-interactions in biological tissues are dominated by Compton scatter while photoelectric absorption is almost negligible. For example, for photons at 140 keV traveling through brain, only 1% (a linear coefficient of 0.0015 cm^{-1}) of the total attenuation (0.1461 cm^{-1}) is due to photoelectric effects. Therefore, one might expect that the detected scattered photons contain essential information about attenuation maps. Conventionally, the use of SPECT images reconstructed from scattered photons or projections in scatter windows for μ map generation has been investigated in the 90s for brain [121] and body (cardiac and liver) SPECT [122–124], yet in most cases solely a contour was estimated from a single scatter window while a uniform attenuation coefficient was assigned to the volume within the contour. This approach is seldom applied clinically, possibly due to the increased complexity in light of the limited improvement of accuracy compared to the ellipse method. With the advance of SPECT instruments, list mode acquisition –in which case the estimated interaction position as well as the energy are recorded simultaneously for every detected event- is gaining popularity. In the work of [125], the authors studied the information content in SPECT list mode data and proposed a MLEM approach using scattered photons from the observed list mode data to jointly reconstruct the attenuation and activity map. This, however, remains a theoretical study due to the complexity of the approach. Similarly, jointly reconstructing the attenuation and activity map using both the photopeak and scattered projections was also proposed in a newly published work for PET scans without time of flight information [126].

Recently, deep learning with convolutional neural networks (CNNs) has been widely investigated in medical image restoration and analysis, e.g. for tissue segmentation, image de-noising, and image transformation (e.g. MRI to CT) [19, 21, 23, 127–130]. These networks can capture relevant information inherent in data and establish highly nonlinear mapping from input to output. This enables the extraction of energy-spatial information from the scatter- and primary-window reconstructed SPECT images for μ map estimation. Successful implementations of this deep learning based strategy have been demonstrated in [23] for ^{99m}Tc-tetrofosmin SPECT scans, and in [22, 131] for ^{18}F-FDG brain PET scans. Specifically in [23], the authors performed image reconstructions from two energy windows (primary and one scatter window) of ^{99m}Tc-tetrofosmin myocardial SPECT; a generative adversarial network was used to transform 4D SPECT image patches (3D SPECT over two energy windows) to 3D attenuation map patches. Results were validated on clinical myocardial scans acquired from a GE dual-head parallel-hole SPECT/CT 850 system.

The aim of the present work is to develop and validate a CNN approach for estimating μ maps of ^{99m}Tc-HMPAO brain perfusion scanning with a full ring stationary SPECT system (G-SPECT-I, [10]). The full emission data including both primary and scattered photons over a broad energy range was utilized via multiple image reconstructions at different energy windows. A patch-based CNN approach was implemented in the present work.

Such an approach is often applied in medical image restoration and analysis [19, 127, 132, 133] due to the reduced number of parameters and increased amount of training data that is required compared to the full-image to full-image approaches e.g. U-Net [134]. In the present study, a large number of 4D (i.e. XYZE dimensions) SPECT patches (sub-volumes of 21 × 21 × 21 voxels × 5 energies) were used as input for the CNN to estimate the attenuation coefficient of the corresponding central voxel of the patch. Our proposed method was tested on Monte Carlo (MC) simulated ^{99m}Tc-HMPAO SPECT scans based on the G-SPECT-I geometry.

4.2. Methods

4.2.1. G-SPECT-I system

The G-SPECT-I is a multi-pinhole system with stationary detectors that demonstrates excellent resolution down to 2.5 mm (resolved rod size for Derenzo hot rod phantom) and a central sensitivity of 415 cps/MBq when using a dedicated brain collimator with 3-mm-diameter pinholes [10]. This system (see Fig. 4.1) consists of nine large-area NaI detectors, an interchangeable collimator and a precisely controlled *xyz*-stage used for bed translation. The collimator assumed in this paper was developed for high sensitivity brain and pediatric imaging and has a total of 54 pinholes with a pinhole diameter of 4.5 mm. The G-SPECT-I has a focused geometry design, similar to that of its preclinical predecessors, i.e. various versions of U-SPECT/CT and VECTor/CT scanners that are now in use by many labs worldwide [7, 39, 57, 64]. Such focused geometries entail that all pinholes simultaneously 'view' a central volume in which a very high sensitivity and complete data (without bed movement) is obtained. This central volume is termed the complete data volume (CDV). This CDV has a transaxial diameter and axial length of 100 mm and 60 mm respectively (see Fig. 4.1). For a scan of an object larger than the CDV, the bed is translated to extend the volume in which sufficient sampling is obtained for optimal image reconstruction. In the present paper, for a whole brain perfusion scan, 18 bed translations with overlapping CDVs are used for sufficient sampling of the entire scan volume based on findings in [70]. All pinhole projections from all bed positions together are used simultaneously for image reconstruction using the so called scanning focus method [49]. Other details concerning G-SPECT-I are described in [27].

4.2.2. SPECT data simulations

The CNN estimation of the μ maps is based entirely on MC simulated SPECT list-mode data for the G-SPECT-I geometry using head phantoms. As the presence of noise in the MC simulated realistic brain images may hamper visualization of AC effects when evaluating the μ maps, we additionally performed a voxelized ray tracing (VRT) simulation [17, 68] to generate noise-free images, such that the accuracy of AC and thus the quality

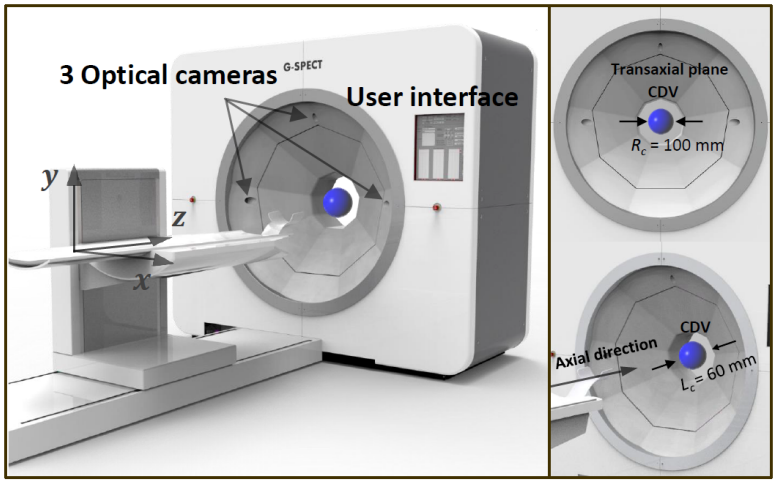

Figure 4.1: Illustration of the G-SPECT-I scanner. The G-SPECT-I system has three optical cameras and a user interface for volume of interest (VOI) selection. Based on the selected VOI, G-SPECT-I software automatically adjusts parameters for optimal imaging of the VOI. The CDV is the volume "seen" by all pinholes; it has a transaxial diameter R_c of 100 mm and an axial length L_c of 60 mm.

of the μ maps could be studied on noisy as well as on noiseless images. These simulations are described in detail below (see also Fig. 4.2).

4.2.3. Digital phantoms for simulation

The publicly available Brainweb database with digital phantoms generated based on normal subjects [135] were used to simulate ^{99m}Tc-HMPAO brain perfusion scans. This type of scan was chosen given the wide application of perfusion SPECT in the diagnosis of cerebrovascular (e.g. stroke), neurological (e.g. epilepsy) and psychiatric disorders (e.g. post-traumatic stress disorder) [71, 72, 79]. A total of six phantoms (the first six phantoms when ordered by subject number) were used in this work, with five used for training and one for testing in a leave-one-out cross validation manner.

For each phantom, the activity map was generated by assigning tracer concentrations to grey matter, white matter and background regions (e.g. skin, skeletal muscle) with a mean ratio of 80:20:5 [85–87] to mimic a realistic blood flow. This ratio was introduced with a random variation (normally distributed) with a standard deviation of 10% for each number to make the activity distribution variable among phantoms. Besides, a total activity of 50 MBq in average was set in the head (resembling an injected dose of 25 mCi as in [88–90]. This number was induced with a standard deviation of 10% (normally distributed) for each phantom. Simulations assumed a scan time of 30 min.

The attenuation map was obtained by segmenting the phantom into different regions. For MC simulations, the maps with each region assigned with a material (e.g. water)

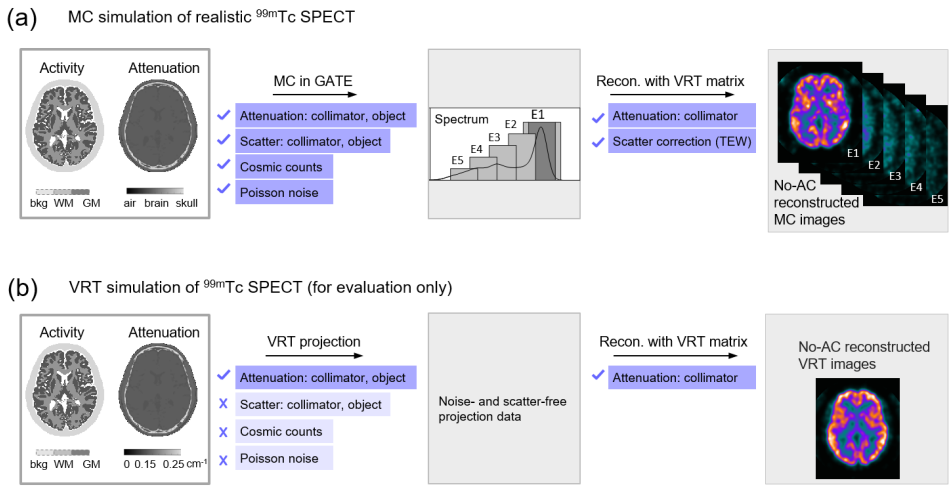

Figure 4.2: Illustration of SPECT data simulation. (a) MC simulations of the head phantoms; for each phantom, an activity and attenuation map were generated and were used for MC simulation. Background counts due to cosmic radiation were added to the MC simulated projection data. Five SPECT reconstructions were performed from different energy windows. (b) VRT simulations to generate noise-free images on which the effects of attenuation correction with different μ maps were studied. In the figure, "bkg" stands for background, "WM" is the white matter and "GM" is the grey matter.

were used (see Fig. 4.2a), while for VRT simulations, the maps with each region assigned with an attenuation coefficient were used (subject to the different requirements of both simulators). A total of eight different regions were segmented, i.e. skull, skin, blood, muscle, brain, water, fat and air, with a corresponding coefficient of 0.248, 0.155, 0.149, 0.147, 0.146, 0.142, 0.128 and 0 cm^{-1} respectively. These values were calculated based on the chemical component of each tissue and the mass attenuation coefficient given in NIST (National Institute of Standards Technology [136]) for photons at 140 keV. The map with given attenuation coefficient is also the ground truth (GT) μ map that was used in the cross-validation step for training and for evaluation of the network predicted μ maps. All phantoms for simulations were down-sampled with trilinear interpolation to have a voxel size of $1 \times 1 \times 1$ mm^3 from its original voxel size of $0.5 \times 0.5 \times 0.5$ mm^3.

Noisy MC simulations

The software used for MC simulations was the Geant4 Application for Tomographic Emission (GATE) [137], with Geant4 v10 and GATE v8.0 installed on a CentOS 6.6 cluster. The long scanning time (30 min) simulation was divided into multiple simulations with shorter time intervals (randomly seeded) that were executed in parallel on a computer cluster.

The system geometry in GATE was designed to closely represent the actual G-SPECT-I design, namely, the computer-aided design (CAD) drawing of the G-SPECT-I collimator was put into GATE. Additionally, nine NaI-scintillators were created natively by defining

a $497 \times 410 \times 9.5$ mm^3 box and replicating it with a ring repeater with a collimator center to detector distance of 757 mm (same as in the G-SPECT-I prototype). The full emission spectrum of ^{99m}Tc was used in the simulations. Physics processes modelled were photoelectric effect, Compton and Rayleigh scattering for gamma photons; bremsstrahlung and multiple scattering for electrons. Within the scintillators, the interaction time, total deposited energy, and energy-weighted average interaction location for each gamma photon were recorded. The uncertainty of the scintillation process and light collection is not fully modelled in the MC simulations, but rather accounted for by taking random samples from a Gaussian distribution in both the spatial and energy domain for each photon recorded on the detector. This is to accelerate the simulation process. The full width at half max (FWHM) of the Gaussians were set according to findings in [138]: for photons at 140 keV, the respective spatial and energy blurring were 3.5 mm and 10% FWHM (based on measurements of detectors at our institute); for photons at other energies these two values were calculated based on models from literature [138].

Background counts due to cosmic radiation were emulated to make the simulation more realistic. This was done by acquiring a long void scan (10 h scan without radioactivity) with the G-SPECT-I prototype, followed by count scaling (by dividing the count numbers by 360 to emulate a 100 sec scan at one bed position) and Poisson statistics generation. This process was performed for all 18 bed positions to emulate a total acquisition time of 30 min. Finally, the background counts at each bed position were added to the corresponding projections obtained with the MC simulation.

Noise-free VRT simulations

The VRT simulator takes the system geometry (i.e. the precise pinhole and detector positions and detector orientations) as input and models the collimator and detector crystal penetration but ignores scattering [17, 68]. For these noise-free VRT scan simulations, the same scanner geometry and the same acquisition parameters (e.g. the same 18 bed positions) as in the MC simulation were assumed. Cosmic radiation counts were not added in the VRT simulations. Effects of patient attenuation were included in the VRT simulated projection data.

4.2.4. Image reconstruction

For the MC simulated projection data, five SPECT reconstructions were performed (see Fig. 4.2a); one used the photons detected in the photopeak window combined with a triple energy window (TEW) scatter correction (28 keV width centered at 140 keV for the photopeak window and 5.6 keV width at each side for scatter correction) and four additional reconstructions were done from different scatter windows (28 keV width centered at 120, 100, 80 and 60 keV respectively). For the VRT simulated projection data, only primary photons were simulated and could thus be reconstructed, resulting in noise- and

scatter-free SPECT scans (see Fig. 4.2b).

All image reconstructions were performed on a 1.5 mm grid, larger than the voxel size of the digital phantoms, to mimic a continuous activity distribution reconstructed on a discrete grid. The system matrix for reconstruction was calculated using the VRT simulator for photons at 140 keV and excludes effects of object scatter. This system matrix was used in image reconstruction for all energy windows. No attenuation correction was performed during reconstruction. Similarity regulated OSEM [18] with 8 subsets and 10 iterations was implemented for image reconstruction.

4.2.5. Attenuation map (μ map) estimation

SPECT image preprocessing

Before being used as input to the CNN to estimate μ maps, the reconstructed MC simulated SPECT images were preprocessed (see also Fig. 4.3). Firstly, the reconstructed noisy MC simulated SPECT images (from all energy windows) were masked to remove artefacts outside the head (Fig. 4.3a). The mask used was a cylinder with a relatively large diameter of 240 mm to safely preserve the brain/head structures. Secondly, intensity normalization was performed to compensate for variance of reconstructed image intensity among phantoms (Fig. 4.3a). Here for each phantom, the maximum intensity from the photopeak reconstructed image was firstly calculated. To reduce the effects of noise and/or any strong edge artefacts (which might appear at the edge slices of the reconstructed volume), this maximum value was obtained from slightly filtered SPECT scans (with a 6-mm-FWHM Gaussian) and from the central 36-mm-thick slices of the reconstructed volume (the reconstructable length even with one bed position in the axial direction of G-SPECT-I, see Fig. 4.1). Subsequently, all five reconstructions from different energy windows were normalized by division by this maximum value such that the images from different phantoms that are used as input to CNN have a similar dynamic range.

The MC SPECT images were down-sampled (tri-linearly) to a voxel size of $3 \times 3 \times 3$ mm^3 from an original voxel size of $1.5 \times 1.5 \times 1.5$ mm^3 before being fed into the neural network. This is to speed up the training process with a relatively larger image voxel size.

CNN regression

The neural network takes 4D (XYZ and energy) patches centered at each voxel as input and was trained to predict the attenuation coefficient of the corresponding central voxel in object space (Fig. 4.3b). The patch size used was $21 \times 21 \times 21$ voxels $\times$ 5 energies. The voxel size of the patch images is $3 \times 3 \times 3$ mm^3. We used a typical CNN architecture that consists of multiple stages of convolution, batch normalization, ReLU activation and max pooling, followed by a fully connected layer with a sigmoid for voxel regression (see Fig. 4.3b). The network that takes in total five energy windows as input is termed CNN5E. In

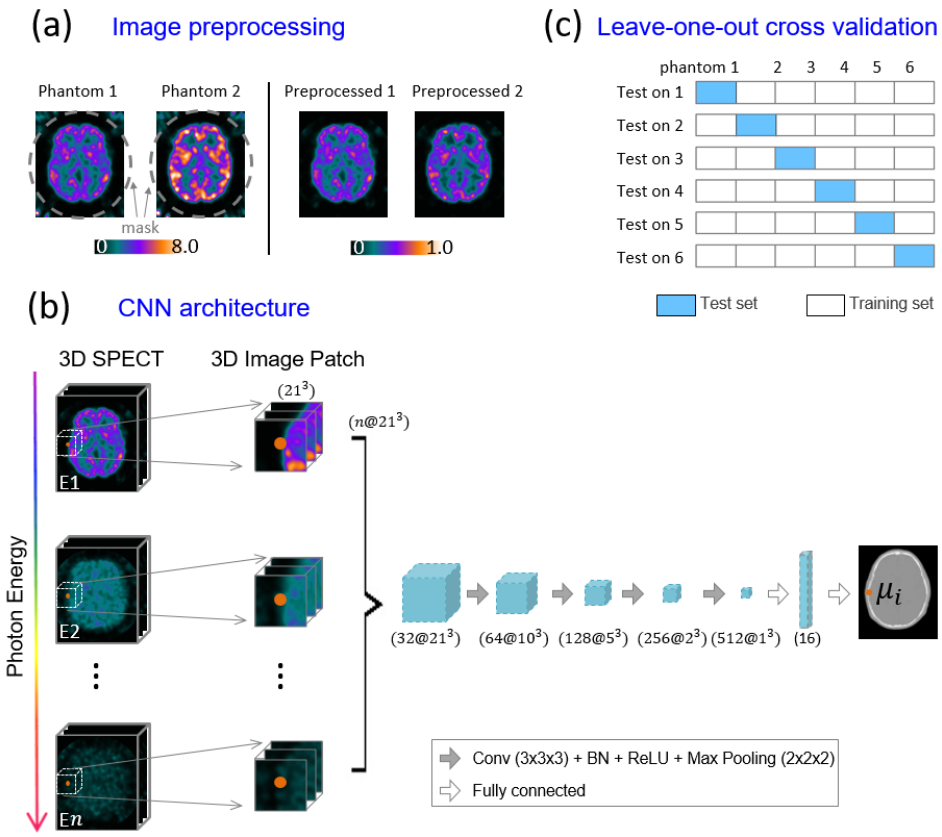

Figure 4.3: Illustration of attenuation map estimation. (a) SPECT image preprocessing; (b) architecture of the CNN; n is the number of energy windows. Three networks were tested. The network that takes five, three or one energy window as input is termed CNN5E, CNN3E and CNN1E respectively. "Conv" and "BN" are short for convolution and batch normalization respectively. The number of the filters is 32, 64, 128, 256 and 512 as shown in the figure. (c) Leave-one-out cross validation with six phantoms; for testing on each phantom, the other five phantoms are used for training.

addition, we included two networks using less energy windows to investigate the effect of energy range of scattered photons on μ map estimation. These two networks are termed CNN3E and CNN1E respectively, with three energy windows (one photopeak window and the two high-energy scatter windows, see Fig. 4.2a) and only the photopeak window involved respectively. Convolution was performed with a kernel size of $3 \times 3 \times 3$. The number of the filters is 32, 64, 128, 256 and 512 as indicated in the figure. Pooling was done with a grid of $2 \times 2 \times 2$.

Leave-one-out cross validation was performed using five phantoms in training and one for testing (see Fig. 4.3c). Each network was trained with a balanced set containing 5k samples (4D patches) randomly selected from each of the three main tissue classes ($0 \leq \mu$

< 0.07/cm for air voxels, 0.07 ≤ μ <0.20/cm for water-like voxels and 0.20 ≤ μ < 0.25/cm for bone voxels; thus 15k samples in total). Meanwhile, for each epoch during training, a new selection of 15k samples was made in order to feed the network with as many samples as possible, similar as in [139]. The network used in this study was trained to minimize the mean square error between the predicted attenuation coefficient μ and the GT μ map (see description in section 4.2.3 for definition).

The proposed network was implemented using TensorFlow. The Adam optimizer [140] with default settings (learning rate = 0.001, β_1 = 0.9, β_2 = 0.999) was used to train the network. A mini-batch of 15 4D patches was used. No validation set was used to determine the optimal epoch due to the limited number of phantoms in this study. The model was trained for 200 epochs for convergence.

4

4.2.6. Attenuation correction with estimated maps

As the aim is to use the μ maps to realize quantitative SPECT, attenuation correction was implemented using the estimated maps. Correction was done using an adapted first-order Chang's method (Chang 1978). In Chang's method with traditional parallel-hole collimation, the transmission along every projection line from a given voxel is calculated, and the transmission fraction (TF) for that voxel is defined as the average transmission value among all projection lines (Eq. 4.1).

$$TF = \frac{1}{M}\sum_{m=1}^{M} \exp\Big(-\int_{L_m} \mu(l)dl\Big) \tag{4.1}$$

Here M is the number of projections involved in data acquisition for a certain voxel, L_m is the mth projection path of gamma photons and μ is the attenuation coefficient along the projection line L_m.

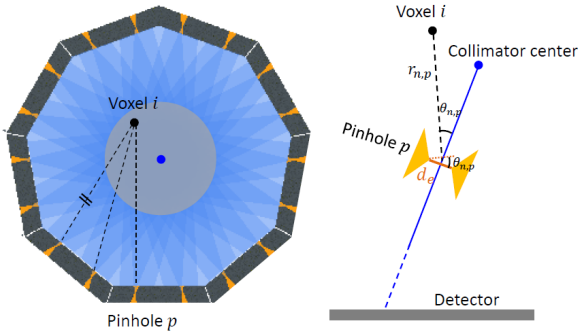

Figure 4.4: Illustration of the adapted first-order Chang's method used in this study. With G-SPECT-I, for a given voxel at a given bed position, only photons that travel toward some distinct directions will be captured by one of the pinholes, as shown in the figure.

Due to the (multi-pinhole multi-bed-position) characteristic of G-SPECT-I, for a given voxel at a given bed position, only photons that travel toward some distinct directions will be captured by one of the pinholes (see Fig. 4.4). Thus, here we implemented an adapted multi-pinhole Chang's method. This was done by first checking –at every bed position– if a voxel is seen by a pinhole. If yes, the transmission along this projection line (from that voxel center to the pinhole center) is counted, and weighted by the pinhole's sensitivity for that voxel (see Eq. 4.2-4.4). The parameters used in the adapted multi-pinhole Chang's method (Eq. 4.2-4.4) are summarized in table 4.1.

$$TF = \frac{1}{\sum_{n=1}^{N}\sum_{p=1}^{P} S_{n,p}} \sum_{n=1}^{N}\sum_{p=1}^{P}\left(S_{n,p}\exp\Big(-\int_{L_{n,p}} \mu(l)dl\Big)\right) \tag{4.2}$$

$$S_{n,p} = \frac{{d_e}^2}{16{r_{n,p}}^2}\cos\theta_{n,p} \tag{4.3}$$

$$d_e = \sqrt{d^2 + \frac{2}{\mu_0} d\tan\left(\frac{\alpha}{2}\right) + \frac{2}{{u_0}^2} d\tan^2\left(\frac{\alpha}{2}\right)} \tag{4.4}$$

Table 4.1: Parameters used in the adapted multi-pinhole Chang's method.

Symbol	Description
N	Number of bed positions in data acquisition
P	Number of pinholes "seeing" the voxel
$S_{n,p}$	Sensitivity of the given voxel corresponding to pinhole p at bed position n [141]
μ	Attenuation coefficient along the line $L_{n,p}$ from voxel to pinhole p center at bed position n
$r_{n,p}$	Voxel-to-pinhole distance, given pinhole p and bed position n
$\theta_{n,p}$	Angle between the line of voxel to pinhole center and the line of collimator center to pinhole center, given pinhole p and bed position n (see Fig. 4.4)
d_e	Equivalent pinhole diameter
d	Actual pinhole diameter (4.5 mm here)
μ_0	Attenuation coefficient (24.3 cm^{-1}, measured experimentally) for pinholes made of hard lead (antimonial lead, containing a mixture of Pb and S_n)
α	Pinhole opening angle (27 ° here)

4.2.7. Evaluation

Visual inspection

The network estimated μ maps were compared to the ground truth μ maps. Besides, attenuation corrected SPECT images using the three CNN estimated μ maps (CNN5E-AC, CNN3E-AC and CNN1E-AC) were compared to the ground-truth-AC (GT-AC) images which use the ground truth μ maps for correction.

Quantitative analysis

4.2.7.2.1 Standard uptake value (SUV) As often used in absolute quantification for PET and SPECT, the standardized uptake values SUVs were calculated in a number of regions of interest (ROIs). The SUV (in units of g/ml) is the mean concentration in a region C_{ROI} (Bq/ml) normalized by the injected dose per patient weight (Bq/g), as shown in Eq. 4.5. In this work a clinically injected dose of 25 mCi and a body weight of 70 kg were assumed for brain perfusion scans for all phantoms. To define the ROIs, a template phantom based on the "Colin 27 Average Brain" [142] provided by the Brainweb database was registered to subject phantoms. ROIs were generated by warping the automated anatomical labeling (AAL v3) template [143] to subject space using the same transformation. A total of 166 regions were defined in the AAL template. These localized regions have a size in the 0.07-41.15 ml range with a median value of 3.75 ml (mean of 6.40 ml) respectively (across all phantoms).

The capability to achieve quantitative SPECT was assessed by comparing the SUVs calculated from the attenuation corrected SPECT images to those of the digital phantom image. This direct comparison of the SUVs was performed in eight big structures as in [21, 144], including four big lobes (temporal, occipital, parietal and frontal lobe), three subcortical structures (thalamus, putamen and caudate nucleus) and the cerebellum. Here in our work these eight structures were further separated into 16 ROIs by hemispheres (e.g. thalamus in the left hemisphere and in the right).

$$SUV(g/ml) = \frac{C_{ROI}}{Dose/Weight} \tag{4.5}$$

4.2.7.2.2 Difference from GT-AC Differences in units of SUV ($DIFF$) when using the CNN estimated μ maps for attenuation correction compared to that of the GT μ maps were evaluated (see Eq. 4.6). The distribution of the differences were presented in Bland-Altman plots as in [144]. Differences (in percentage) from the GT-AC images, which is termed deviations (DEV) here, were calculated as in Eq. 4.7. Statistical significance of the deviations was assessed using paired t tests ($p < 0.05$ is considered as statistically significant) as in [22, 144].

$$DIFF(SUV) = SUV - SUV_{GT-AC} \tag{4.6}$$

$$DEV_{SUV}(\%) = \left| \frac{SUV - SUV_{GT-AC}}{SUV_{GT-AC}} \right| \times 100\% \tag{4.7}$$

For all SPECT images shown in this paper, a 3D Gaussian post filter with 6 mm FWHM was applied. For quantitative analysis, measurements were performed on the unfiltered SPECT images to avoid any bias from filtering.

4.3. Results

4.3.1. Visual inspection

Figure 4.5 shows a comparison of the CNN estimated and the ground truth μ maps. Five slices obtained from one of the phantoms (indicated by the solid black lines) are displayed. A full comparison of results for all six phantoms is included in the appendix (Fig. 4.9). Figure 4.5 shows that compared to the ground truth, μ maps can be well estimated with CNN5E and CNN3E in which cases scatter windows (besides the photopeak window) were involved as input to the CNN; in these cases, the shape and size of the heads are well retrieved. The improvement by including two additional low-energy scatter windows from CNN3E to CNN5E is small.

CNN1E has inferior performance compared to CNN5E and CNN3E; the head size can be inaccurately predicted with CNN1E as in the example shown in Fig. 4.5 where the predicted μ maps appear incorrectly large. Besides, an insufficient estimation of the air and bone structures was observed for CNN1E as demonstrated in figure A1 (phantom number 5). This might be due to the fact that input to CNN1E includes only the photopeak window which represents solely the activity distribution. Information to correctly determine the air and bone voxels where there is barely any tracer accumulation is thus insufficient.

Figure 4.6 shows a comparison of the SPECT images as well as the image profiles when using the ground truth or CNN μ maps for attenuation correction. SPECT images presented in this figure are the noiseless scans from VRT simulations to better visualize the effects of attenuation correction. Results of corrections performed on the realistic MC simulated scans are included in the appendix (Fig. 4.11). Figure 4.6 shows that the image and image profile differences from the ground-truth-AC are small for CNN5E-AC and CNN3E-AC images, while CNN1E-AC images deviate more from the ground-truth-AC.

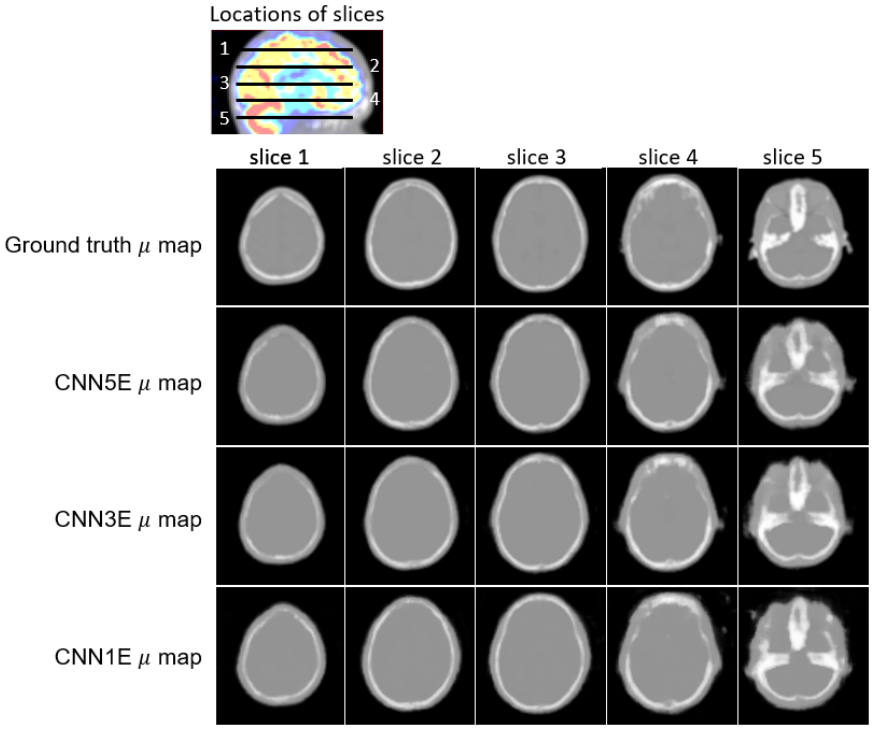

Figure 4.5: Comparison of the ground truth and CNN estimated μ maps. Five slices (equally distributed with 25.5 mm separation) obtained from one of the phantoms are displayed. Locations of the slices are indicated by the solid lines. The predicted μ maps of CNN1E appear incorrectly large.

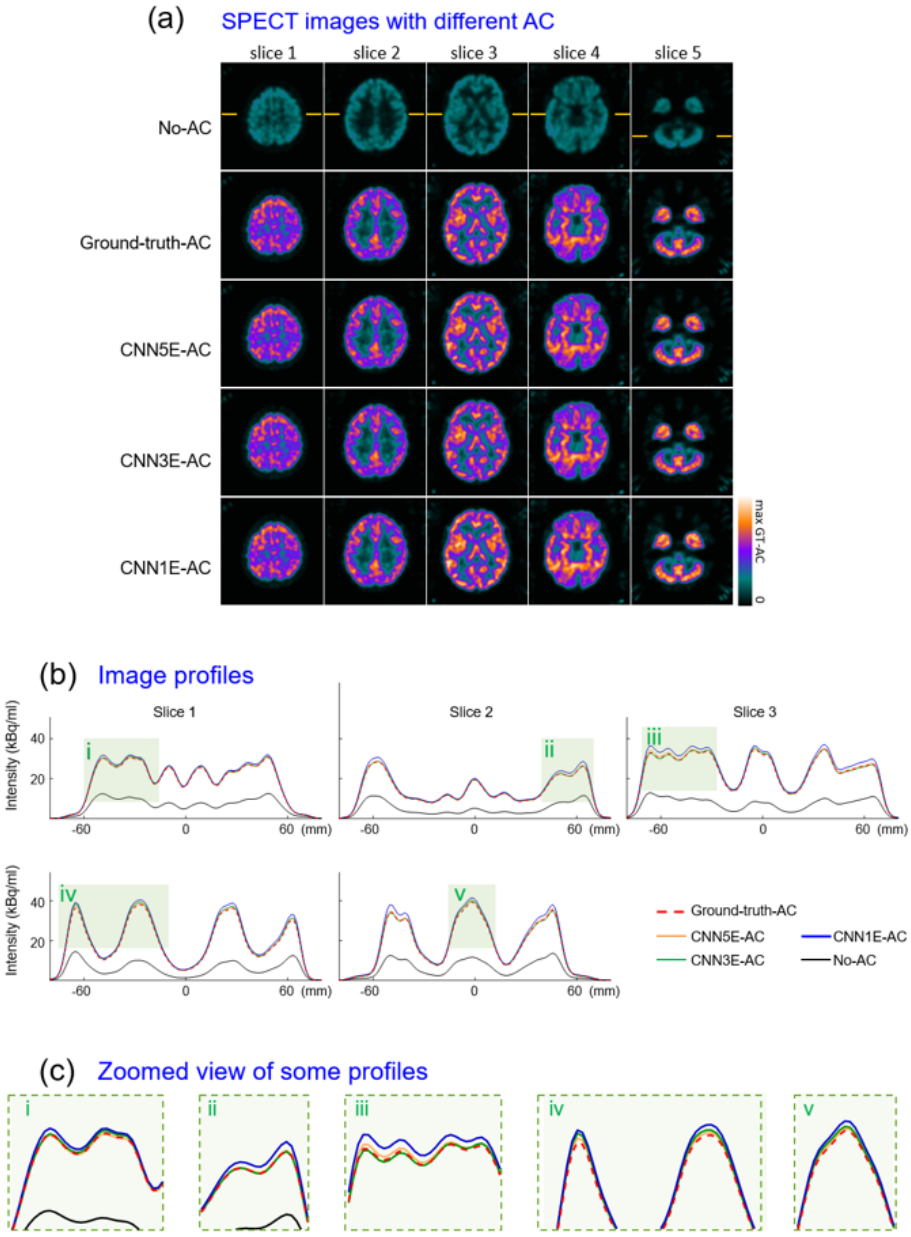

Figure 4.6: Comparison of the attenuation corrected SPECT images using different μ maps. (a) Attenuation corrected SPECT images; image profiles through each slice are included and shown in panel (b). These profiles are taken from a line with a width and thickness of 4.5 mm. A zoomed view of some parts of the profiles are displayed in panel (c).

4.3.2. Quantitative analysis

SUV

The absolute quantification results when using the ground-truth-AC and CNN-AC are shown in figure 4.7. The SUVs in the 16 merged ROIs (8 structures × 2 hemispheres) are plotted. Figure 4.7 shows that attenuation correction is essential to achieve accurate quantification; without correction, an underestimation of about 70% for the SUVs is observed. Compared to the digital phantom, the ground-truth-AC, CNN5E-AC and CNN3E-AC images suffer from slight underestimation of the SUVs, which could be due to the partial volume effects given the finite system resolution (~ 3.5 mm) or the imperfect attenuation correction method.

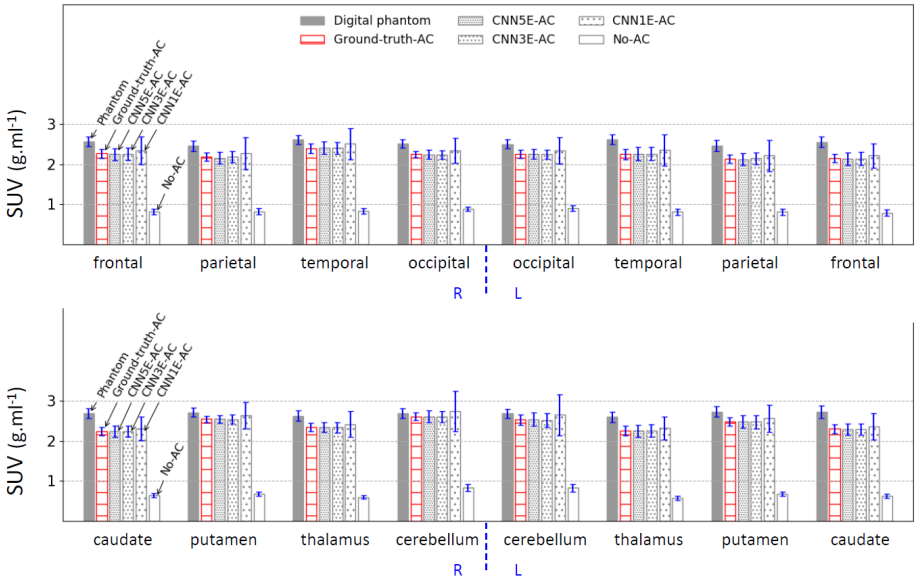

Figure 4.7: Comparison of the SUV values when using various AC methods in 16 regions (8 structures × 2 hemispheres). The mean and standard deviation from all 6 phantoms are displayed for each region.

Difference from GT-AC

In the Bland-Altman plot (Fig. 4.8), the distribution of the SUV differences is assessed. Fig. 4.8a plots the distribution for measurements taken from the merged 16 × 6 regions while those from the localized 166 × 6 regions over the entire brain are given in Fig. 4.8b. In Fig. 4.8, differences from the ground-truth-AC are small (close to the zero line) for both the CNN5E-AC and CNN3E-AC. Among these two methods, CNN3E-AC shows a slightly more diverging distribution and thus a larger difference. A deviation from the ground-truth-AC of 10% is highlighted by the semi-transparent grey region. For CNN5E-AC, all measurements are within 10% deviation across all regions.

The mean value of the deviations for measurements among all ROIs is summarized in table

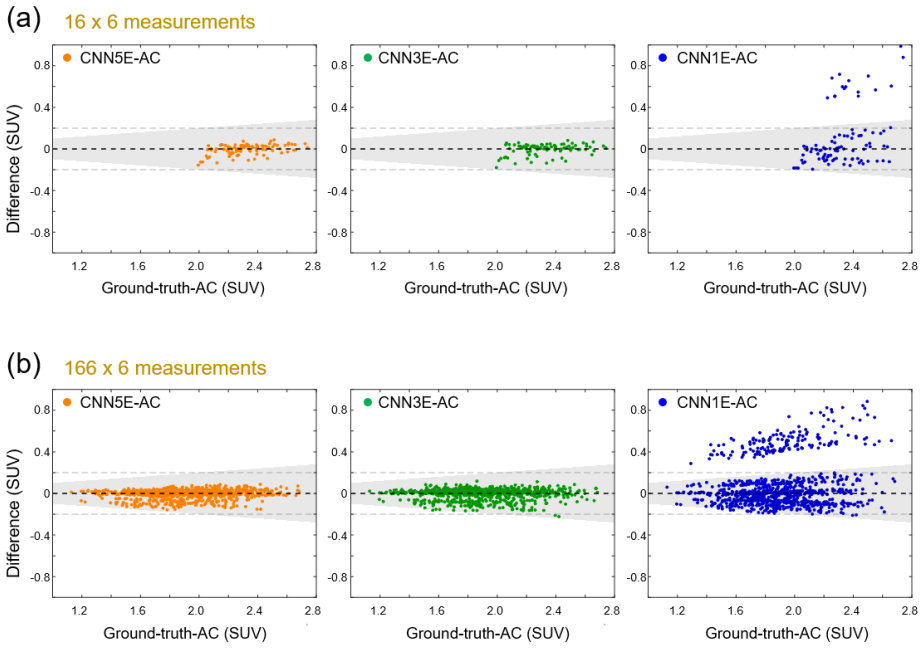

Figure 4.8: Bland-Altman plots when using different CNN-AC methods. Measurements taken from the merged 16 × 6 regions are plotted in (a) while those from the localized 166 × 6 regions are given in (b).

4.2 for different CNN-AC methods. For CNN5E-AC and CNN3E-AC, the mean deviations across 16 × 6 regions are within 1.60% and are statistically insignificant ($p > 0.05$), while for assessments across 166 × 6 localized regions, the mean deviations are within 1.82% ($p < 0.05$).

Table 4.2: SUV deviation (mean ± standard deviation) from the ground-truth-AC across 16 merged ROIs and 166 small localized ROIs for all six phantoms. $P < 0.05$ is defined as the significance level.

16 × 6 regions	CNN5E-AC	CNN3E-AC	CNN1E-AC	No-AC
DEV_{SUV}(%)	1.60 ±1.53	1.59 ±1.68	7.35 ±8.91	67.50 ±5.30
P	0.368	0.616	0.002	<0.001

166 × 6 regions	CNN5E-AC	CNN3E-AC	CNN1E-AC	No-AC
DEV_{AI}(%)	1.63 ±1.66	1.82 ±1.90	7.53 ±8.80	69.25 ±4.40
P	<0.001	0.016	<0.001	<0.001

4.3.3. Counts from each energy window

Table 4.3 provides the number of counts detected in each energy window. An example of the energy spectrum from one phantom is shown in figure 4.2a. Table 4.3 shows that

i) the detected counts from tracer emission decreases for energy windows going from E1 to E5, and ii) contribution of cosmic radiation to the total increases (from 5% to 15%) for energy window going from E1 to E5.

Table 4.3: Comparison of the count number from different energy windows (keV). The mean counts across all phantoms are given. 'M' stands for the unit million. The first row gives the mean counts detected from tracer emission based on Monte Carlo simulations. The second row gives the background counts from cosmic radiation based on a long void scan (10 hours scan without radioactivity) with the G-SPECT-I prototype. Note that these two types of counts were added in projections for image reconstruction.

Mean counts	Photopeak E1 (126-154)	E2 (106-134)	E3 (86-114)	E4 (66-94)	E4 (46-74)
From tracer	7.50 M	4.20 M	3.59 M	3.29 M	2.19 M
From cosmic	0.45 M	0.44 M	0.45 M	0.54 M	0.35 M
Cosmic/tracer	6.0%	10.5%	12.5%	16.4%	16.0%

4.4. Discussion

The current work shows the feasibility of estimating attenuation maps by using SPECT data only without additional (radiation) scans or the need to draw head contours. This could facilitate SPECT imaging with minimal ionizing radiation or user interactions, enabling quantitative brain perfusion SPECT to be independent from data from other scanners, thereby avoiding registration issues between modalities as well.

Figures 4.5-4.7 and figure 4.9 show that despite of the inadequate μ map estimation of CNN1E, a reasonable quantification accuracy could still be obtained with this method. This might explain the broad use of an ellipsoidal region for attenuation correction in clinical routine given its benefit of simplicity and decent effectiveness (i.e. the improved accuracy compared to that of not performing a correction at all). While various contour-based methods have been proposed to attain a uniform μ map, devising one here that is suitable for our work is beyond the scope of this paper. Alternatively, a ground-truth-uniform (GT-uniform) μ map, which can be regarded as the best achievable μ map using the contour-based method, was generated by replacing all tissues in the GT μ map with the attenuation coefficient of brain tissue (μ = 0.146/cm). This part of the results is included in the appendix (figure 4.10 and table 4.4). GT-uniform-AC suffers from underestimation of the SUVs compared to the GT-AC since all bone voxels are replaced by brain. The Bland-Altman plot of GT-uniform-AC shows a more diverging distribution of the SUV differences compared to those of the CNN5E-AC and CNN3E-AC. The mean deviation from GT-AC is within 3.78%, which is also larger than CNN5E-AC (1.63%) and CNN3E-AC (1.82%). Note that the GT-uniform μ map is the ideal μ map one could get using the contour-based method. In reality, obtaining such a contour generally requires image processing steps, which involve a set of parameters (e.g. smoothing and threshold) that are sensitive to tracer distribution and noise in image. On the other hand, with

the proposed CNN method, an optimal mapping with a large number of parameters is generated automatically. Here our results show that, even though the tracer distribution and the amount of activity were variable for each phantom, CNN could still accurately estimate the attenuation map when trained on a small set with five phantoms.

Three neural networks (CNN5E, CNN3E and CNN1E) were tested in this work, where we found that compared to the use of only the photopeak window (CNN1E), the involvement of scatter windows as done in CNN3E and CNN5E improves the performance. The use of five energy windows (CNN5E) instead of three (CNN3E) only has a limited effect on results. This might be due to i) the intrinsic weak correlation between the multi-order scattered photons and the attenuation coefficients and ii) the relatively low scatter signal compared to the level of noise in the additional two low-energy scatter windows of CNN5E (see table 4.3). The results also indicate that investigating the utilization of photons from high-energy scatter windows close to the photopeak might be beneficial. In this paper, energy windows used all have an equal width of 28 keV and are already slightly overlapping (see figure 4.2a), thus adding additional high-energy scatter windows may not lead to improvements. Given better energy resolution, the incorporation of more energy windows may be possible by narrowing the width of each window. This could provide the network with photons with more precise energy-spatial information. However, the exact effect on CNN estimation of μ maps requires additional studies.

In this paper, evaluation of attenuation correction with the CNN estimated μ maps was performed on the noise-free VRT simulated scans (for better visualization of the AC effects when using different μ maps). Results of correction performed on the realistic MC simulated scans are included in the appendix (figure 4.11). These results show that visually the differences of using GT-AC, GT-uniform-AC, CNN5E-AC and CNN3E-AC are small on the MC simulated scans. Besides, comparing the realistic MC simulated SPECT images to the noiseless VRT scans (figure 4.6a), one could see that the effects on image quality due to, e.g. noise and imperfect scatter correction as in the former scans can be larger than effects caused by using different CNN-AC methods (e.g. CNN5E-AC and CNN3E-AC). This is not surprising as noise generally plays a critical role in SPECT. While we aim to estimate the attenuation map using deep learning for automatic and accurate attenuation correction, future development that could achieve SPECT denoising can be beneficial, and using deep learning techniques for this task is also being actively investigated [145–147].

As a feasibility study based on Monte Carlo simulated data, limitations of this work include a validation using experimental scans which is required to bring the method closer to clinical applicability. For implementation on experimental data, we expect that the network may be trained on physical scans with CT ground truth attenuation maps acquired from only a few patients, as it was shown that the proposed CNN needed only a limited number of training samples. Besides, the effect of subtle differences of attenuation correction when using a CNN instead of a CT μ map needs to be evaluated on real

patient data by human readers with a specific clinical task to ultimately prove the merit of the proposed CNN approach. Additionally, we used discretized maps consisting of a limited number of tissue classes (eight classes) as the ground truth attenuation map. For brain scans with relatively simple attenuation maps, this approximation could be acceptable. For other applications especially those involving fine structures, e.g. myocardium imaging, more complex attenuation maps with more tissue classes or with continuous attenuation coefficients would be preferable. Furthermore, the proposed method was tested on a G-SPECT-I geometry as it is an ultra-high resolution system we are developing at our institute. Given the validity of the proposed approach on G-SPECT-I, it would be worthy to try it for other standalone SPECT devices as well. Moreover, the proposed methodology was validated only for brain perfusions scans with ^{99m}Tc-HMPAO in the present work. We expect that the approach may be applicable to other types of scans when the CNN is trained on that specific scan, yet the accuracy and effectivity have to be validated.

4.5. Conclusion

We have implemented and validated a neural network approach to generate attenuation maps solely from SPECT emission data for ^{99m}Tc-HMPAO brain perfusion scans. This could enable quantitative SPECT imaging with minimal ionizing radiation and make SPECT independent of data from other imaging modalities, while the fully automated approach could reduce the subjectivity due to intra- or inter-observer variability.

Appendix

Comparison of the ground truth GT and CNN estimated μ maps for all six phantoms are given in figure 4.9. Five slices with an equal separation of 25.5 mm are displayed for each phantom. Figure 4.10 and table 4.4 provide the quantitative analysis results of GT-uniform-AC. The results from CNN5E-AC are shown together here as a comparison. Figure 4.11 displays the MC simulated realistic SPECT scans after attenuation correction with different μ maps. Quantitative analysis on these MC simulated scans of the deviations from the GT-AC for various CNN-AC methods are not included. These deviations are the same as those given in table 4.2 where assessments are performed on the noiseless VRT scans as the deviations depend only on the transmission fraction of the μ maps (see Eq. 4.2).

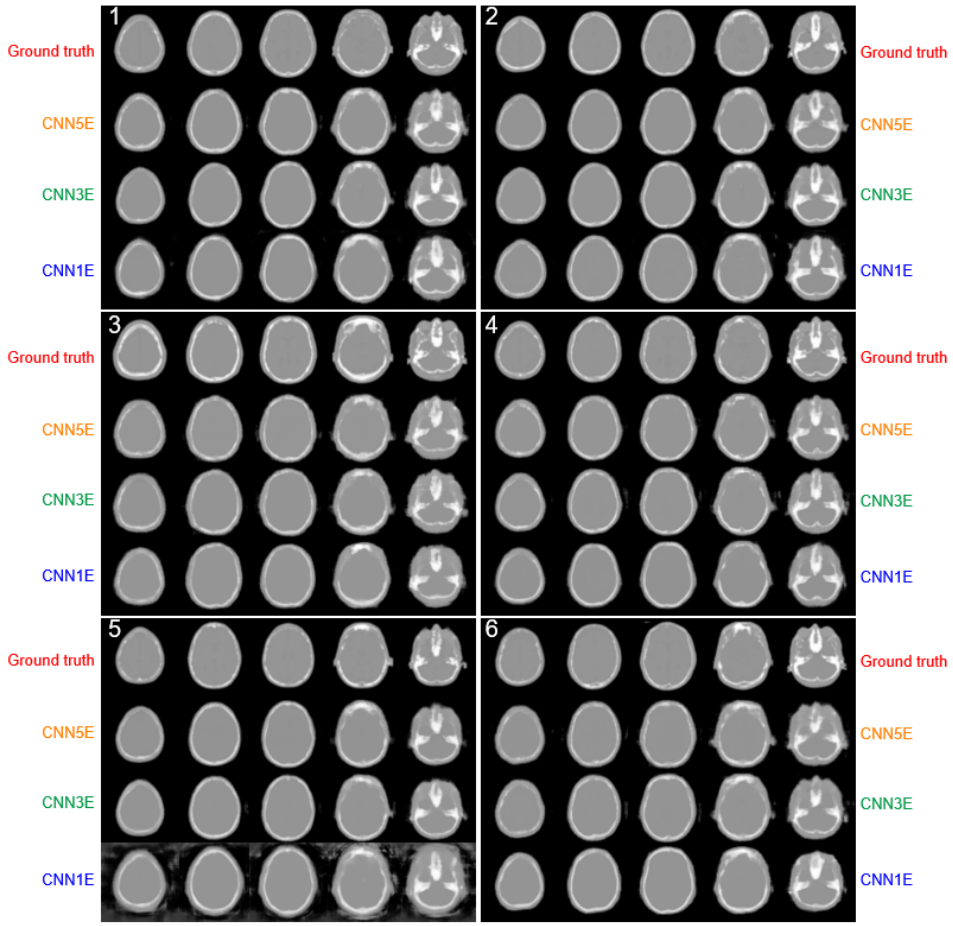

Figure 4.9: Comparison of the ground truth GT and the CNN estimated μ maps for all six phantoms. Five slices from the top to the bottom of the head (equally distributed with 25.5 mm separation) are displayed.

Table 4.4: SUV deviation (mean ±standard deviation) from the ground-truth-AC for ground-truth-uniform-AC when assessed on the VRT simulated SPECT images. The results from CNN5E-AC are also given here as a comparison. $P< 0.05$ is defined as the significance level.

	16 × 6 regions		166 × 6 regions	
	CNN5E-AC	Ground-truth-uniform-AC	CNN5E-AC	Ground-truth-uniform-AC
DEV_{SUV}(%)	1.60±1.53	3.72±1.58	1.63±1.66	3.78±1.65
P(%)	0.368	<0.001	<0.001	<0.001

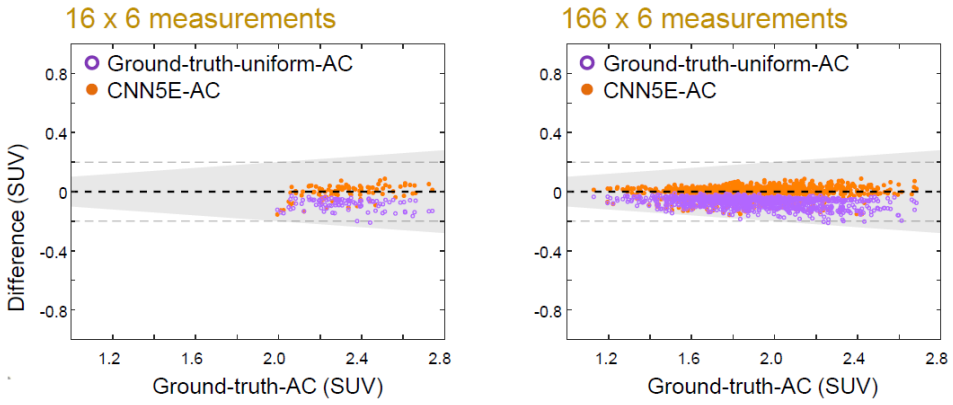

Figure 4.10: Bland-Altman plots for SUVs calculated from the noiseless VRT simulated SPECT images when using ground-truth-uniform-AC. The results from CNN5E-AC are also plotted as a comparison. The difference for ground-truth-uniform-AC are negative since all bone voxels are replaced by the attenuation coefficient of brain tissue.

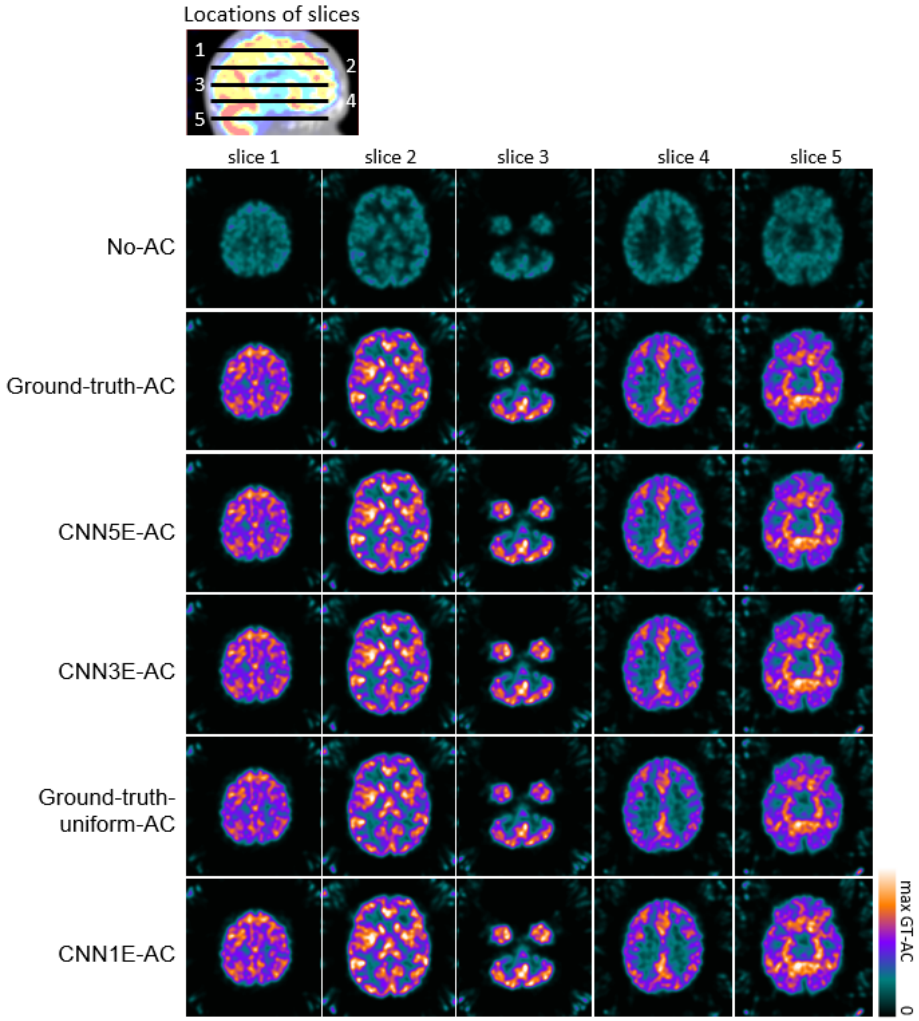

Figure 4.11: Comparison of the attenuation corrected images when using different μ maps for Monte Carlo simulated realistic SPECT scans. Five slices equally distributed with 25.5 mm separation are displayed (as in Fig. 4.5–4.6). Locations of the three slices shown at the left panel are indicated by the solid lines and those at the right panel are highlighted by the dashed lines.

5

Convolutional neural network based attenuation correction for SPECT DaTscans with focused striatum imaging

This chapter is adapted from:
Yuan Chen, Marlies C. Goorden, Freek J. Beekman. *Convolutional neural network based attenuation correction for SPECT DaTscans with focused striatum imaging*, Physics in Medicine and Biology **under revision** (2021).

SPECT imaging with ^{123}I-ioflupane (DaTscan) can be used for diagnosis of neurodegenerative disorders like Parkinson's disease. Attenuation correction (AC) may improve quantitative analysis of DaTscans. Ideally, AC would be performed based on attenuation maps (μ-maps) derived from perfectly registered CT scans. Such μ-maps, however, are most times not available and possible errors in image registration can induce quantitative inaccuracies in AC corrected SPECT images. Earlier, we showed that a convolutional neural network (CNN) based approach allows to estimate SPECT-aligned μ-maps for full brain perfusion imaging using only emission data. Here we verify if a similar CNN method could be applied to axially focused DaTscans, which is challenging as only a low activity level is present outside the central region of the brain. The work is tested on a high-resolution multi-pinhole prototype clinical SPECT system in a Monte Carlo simulation study. Three CNNs that estimate μ-maps in a voxel-wise, patch-wise and image-wise manner were investigated. The impact of AC on DaTscans using the ground truth μ-maps (GT-AC), CNN estimated μ-maps (CNN-AC) was evaluated and compared with the case when no AC was done (No-AC). Results show that the effect of using GT-AC versus CNN-AC or No-AC on striatal shape and symmetry is minimal. Specific binding ratios (SBRs) from localized regions shows a deviation from GT-AC ≤2.0% for all three CNN-ACs while No-AC systematically underestimates SBRs by 10.9%. Strong correlation was observed between GT-AC based SBRs and SBRs from CNN-ACs (R^2 ≥0.98) and No-AC (R^2 = 0.99). Absolute quantification of standardized uptake value (SUV) shows a deviation from GT-AC ≤2.4% for all three CNN-ACs and of 71.7% for No-AC. To conclude, all three CNNs show comparable performance in accurate μ-map estimation and DaTscan quantification. Thus, CNN estimated μ-map could be a promising substitute for a CT-based μ-map.

5.1. Introduction

SPECT with ^{123}I-ioflupane (DaTscan) can be used for visualization of the dopamine transporter (DaT) distribution in the brain. This enables assessment of parkinsonian syndromes, particularly for differentiation of Parkinson's disease from essential tremor and for differentiation of dementia with Lewy Body from Alzheimer disease [28, 30]. Current clinical assessment of DaTscans relies mainly on a visual inspection of the extent of DaT reduction in the striatum, the striatal shape and its symmetry [32, 148]. Relative quantification by calculating the regional striatal uptake ratios could reduce inter- and intra-observer variability and may enable longitudinal studies to monitor disease progression [149] 2017) and therapeutic effects (Parkinson Study Group 2002). For accurate relative quantification, correction for photon attenuation in the patient head is recommended by guidelines [148, 150]. Ideally, attenuation correction (AC) would be performed based on an attenuation map (μ-map) derived from a perfectly registered CT scan. This μ-map provides the tissue attenuation coefficient at each voxel in the patient. However, such a CT scan is often not available, may lead to increased radiation dose. Moreover, possible errors in image registration can induce quantitative inaccuracies in SPECT images [118, 151, 152]. Besides the CT based approach, manually drawing an ellipse around

the head contour and assuming uniform attenuation within the ellipse is widely used for attenuation map approximation in brain SPECT studies [44, 153]. This ellipse method, however, suffers from observer subjectivity and insufficient estimation of the head contour and internal head anatomy.

Apart from the use of an additional CT scan or a simple ellipse, automatic approaches based only on SPECT data have been investigated, which can be mainly classified into two categories. The first category contains sophisticated methods using SPECT photopeak projections to estimate the attenuation map and activity map either simultaneously by means of joint reconstruction [154–156] or independently by applying data consistency conditions [157–160]. This approach however has limited utility in clinical routine due to cross-talk artefacts, instability and the computational complexity. The second category consists of contour-based methods that assume uniform attenuation within the contour. Such a contour can be obtained by automatic edge-detection in projection space or on non-corrected SPECT images [121, 123, 124, 161]. Automatic contour detection techniques are not commonly applied clinically, possibly due to the increased complexity given the minimal improvement of accuracy compared to the manual drawn ellipse approach. Interestingly, the value of SPECT images reconstructed from a scatter window has been emphasized in these contour detection studies for edge determination [121–124]. This is justifiable as Compton scatter is the dominant photon-tissue interaction for clinical SPECT, and the probability of Compton scatter is proportional to the tissue density (with a maximal probability at skull and almost zero outside the body). Thus, the tissue density information embedded in scattered data could be helpful to highlight the tissue boundaries.

Lately, deep learning with neural networks has been applied to estimate μ-maps using SPECT-data-only for clinical [23] and simulated [162] ^{99m}Tc-tetrofosmin myocardial scans and PET-data-only for clinical ^{18}F-FDG brain PET scans [22, 131]. Our group has recently also demonstrated a convolutional neural network (CNN) approach to estimate μ-maps for ^{99m}Tc-HMPAO full brain perfusion scans [104] based on a Monte Carlo study assuming a multi-pinhole clinical SPECT geometry (G-SPECT-I [10]). In this study, both the primary and scattered photons from SPECT emission data were used via multiple image reconstructions from different energy windows to obtain as much attenuation information as possible. Using these multi-energy SPECT images, a patch-voxel CNN with an encoder architecture was implemented to transform a 4D SPECT patch (3D SPECT plus one energy dimension) to a single attenuation coefficient for the central voxel of the patch. Such a patch-voxel approach was used due to its advantage of requiring a reduced number of parameters and providing an increased amount of training data compared to the full-image to full-image approaches e.g. U-Net [134]. Accurate attenuation maps were obtained with the proposed CNN approach for the ^{99m}Tc-HMPAO full brain perfusion scans.

For a DaTscan, direct implementation of the previously investigated CNN method may be

challenging. Firstly, a DaTscan has a more localized activity distribution due to the high affinity of the tracer (^{123}I-ioflupane) to the dopamine transporters in the small striatum while the rest of the brain expresses only non-specific binding leading to a low background activity level. Secondly, a DaTscan has an overall low tracer uptake in the brain (with a standard injection dose of 185 MBq) compared to that of a brain perfusion scan (standard injection dose of 925 MBq), resulting in a limited number of primary and scatter events being captured and potentially utilized. Lastly, the clinical assessment of a DaTscan often uses only a few transaxial slices around the striatum (e.g. 20 mm thick slices [149]) rather than the full axial length of the brain. Previously, we demonstrated with a simulation study that for DaTscans, focused striatum imaging with a confined axial length can maximize the count yield without sacrificing image quality [27]. Such a focused imaging strategy was evaluated for the multi-pinhole prototype clinical G-SPECT-I scanner and may enable G-SPECT-I to become a new clinical platform for high-resolution and low dose DaTscan imaging. Hence, in case only a few SPECT slices are scanned, μ-maps that could be beneficial for DaTscan attenuation correction may not be fully estimated.

The aim of this paper is to develop and validate a deep-learning based approach for μ-map estimation using only emission data for DaTscan imaging. To this end, SPECT data were acquired with a protocol aimed at imaging a few slices centered at the striatum based on the G-SPECT-I geometry. Besides the patch-voxel CNN that was implemented in our previous work, we also tested two other networks that have been used in relevant recent studies which estimate μ-maps with a patch-patch or image-image based method [22, 23, 130]. The proposed strategy was evaluated using Monte Carlo simulations based on the G-SPECT-I geometry. Quantitative accuracy of the CNN approach was assessed on the network estimated μ-maps and on attenuation corrected SPECT images.

5.2. Methods

5.2.1. G-SPECT-I system

The G-SPECT-I [10] consists of nine large-area NaI stationary detectors, a multi-pinhole collimator and a precisely controlled xyz-stage used for bed translation (see Fig. 5.1). All pinholes are simultaneously 'viewing' a central volume from which complete data is obtained without any bed movement. This central volume is thus referred to as the complete data volume (CDV, see see Fig. 5.1). For a scan of an object larger than the CDV, the bed is translated to extend the scanning region with sufficient sampling. In this work, a total number of 8 bed translations (2 axial translations combined with 4 transaxial translations) was used based on findings in [27] for an optimal focused striatum scan to maximize the count yield. This bed translation trajectory ensures an axial scanning length of about 57 mm which is long enough to cover the entire striatum (35 mm). All pinhole projections

from all bed positions together were used simultaneously for image reconstruction using the so-called scanning focus method [49]. Other details concerning G-SPECT-I are described in [27].

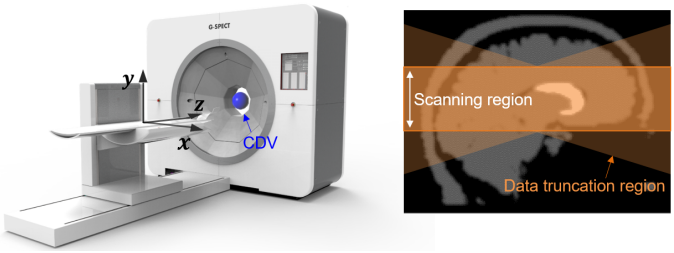

Figure 5.1: Illustration of the G-SPECT-I scanner (the left image) when a small-bore collimator dedicated for brain imaging was mounted, and the focused striatum imaging strategy (the right image). The CDV is the volume "seen" by all pinholes; it has a transaxial diameter of 100 mm and an axial length of 60 mm. The patient bed can be shifted in xyz directions to position different parts of the patient head into the CDV and thus extend the scanning region with sufficient sampling. With the focused striatum imaging strategy, the scanning region is confined in axial direction to maximize the count yield from the striatum. The data truncation region is 'seen' by only part of the pinholes and thus sampling is not complete.

5.2.2. Simulated SPECT scans

To mimic realistic SPECT scans, full system Monte Carlo (MC) simulations were performed. These MC simulated scans were used as input to the CNN for μ-maps estimation. Attenuation correction accuracies based on these μ-maps were evaluated subsequently; this evaluation was done on MC simulated realistic images but was also performed on noise-free simulated SPECT images. The latter noise-free images were involved to better visualize and quantify attenuation correction with different μ-maps. These noise-free scans were obtained with a voxelized ray tracer simulator (VRT) and assumed the same system geometry and the same acquisition parameter as the MC simulations but eliminated noise and scatter. Both simulation methods are summarized in Fig. 5.2 and are described in more detail below.

Digital phantoms

The publicly available Brainweb dataset containing 20 phantoms generated from normal subject scans was used. For each phantom, an activity distribution map and an attenuation map were generated (see Fig. 5.2). The activity map was obtained by assigning ^{123}I-ioflupane (159 keV) to the striatum and the background (which is the rest of the brain and the skin) with a mean concentration ratio of 8:1 [54, 163, 164]. This ratio was set slightly differently for each phantom with a standard deviation σ of 10% (normally distributed) for both the striatum and background uptake. A total activity of 7.4 MBq in average was put in the phantom (resembling an injected dose of 185 MBq and a brain uptake of 4% at the time of imaging [165]). Similarly, we assumed a variation of the total activity for each

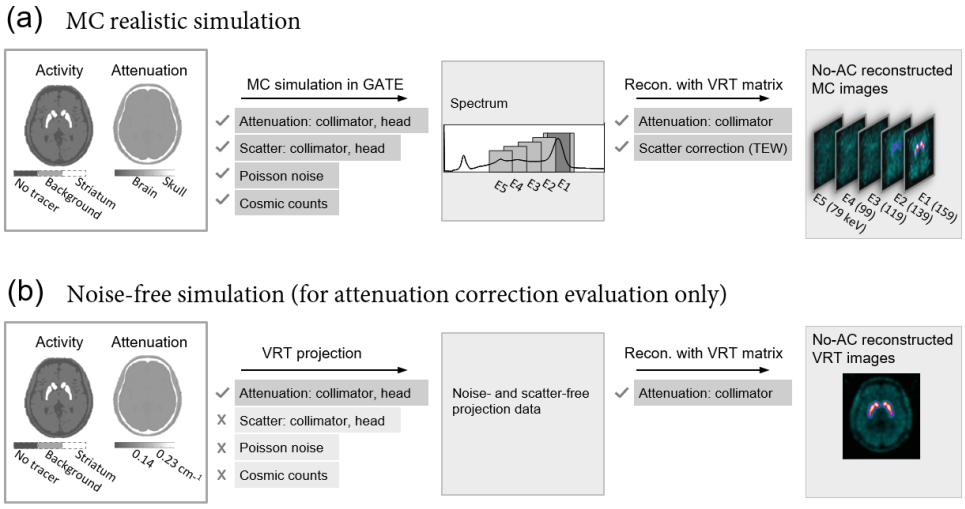

Figure 5.2: Illustration of SPECT data simulation. (a) MC simulations for realistic DaTscans; for each phantom, an activity and attenuation map were generated and were used for MC simulation. Background counts due to cosmic radiation were emulated and added to the MC simulated projection data to make the simulation more realistic. Five SPECT reconstructions were performed from different energy windows. (b) Noise-free simulated images on which the effects of attenuation correction with different μ-maps were studied. The MC simulation uses the attenuation map with each region assigned with a material (skull or brain), while for noise-free simulations, the maps with each region assigned with an attenuation coefficient were used (subject to the different requirements of both simulators).

phantom by sampling from a normal distribution (σ = 10%).

The attenuation map was obtained by tissue segmentation. Regions of skull, skin, blood, muscle, brain, water, fat and air structures were segmented. These regions were assigned with a respective attenuation coefficient of 0.232, 0.148, 0.143, 0.141, 0.140, 0.135, 0.123 and 0 cm^{-1}. This map with designated coefficients was considered to be the ground truth (GT) μ-map that was later used for training of the neural networks. Phantoms were randomly rotated (-20° to 20°) and translated (-10 to 10 mm) to make the dataset more variable. All phantoms were down-sampled using trilinear interpolation to a voxel size of 1.0 × 1.0 × 1.0 mm^3 from their original voxel size of 0.5 × 0.5 × 0.5 mm^3.

MC simulated realistic projections

MC simulations of the 20 phantoms were performed with Geant4 Application for Tomographic Emission (GATE) [137] with geometry based on G-SPECT-I. The MC simulation assumes a total scan time of 30 min. Besides, cosmic background counts were added to the MC projections to make the simulation more realistic. More details of the MC simulation in GATE and the cosmic background counts emulation with the G-SPECT-I system were described in [104].

Noise-free simulated projections

For all 20 phantoms, noise-free forward projections were generated with the VRT simulator. This simulator takes the system geometry (i.e. the precise pinhole and detector positions and detector orientations) as input and models the collimator and patient attenuation but ignores scatter [17, 68], as shown in figure 5.2. No noise or cosmic radiation counts were modelled in the VRT simulated projections.

Image reconstruction

A system matrix calculated based on the VRT simulator was used for image reconstruction of the MC simulated projections and the noise-free simulated projections (see figure 5.2). No patient attenuation correction was performed during reconstruction. All image reconstructions were performed on a 1.5 mm grid, larger than the voxel size of the digital phantoms, to mimic a continuous activity distribution reconstructed on a discrete grid. Similarity regulated OSEM [18] with 8 subsets and 10 iterations was implemented for image reconstruction.

As demonstrated in our previous study [104], accurate estimation of the μ-maps can be obtained when photopeak as well as scatter window reconstructed images were used as input to CNN. Therefore, five SPECT reconstructions were conducted from different energy windows to obtain tissue attenuation information as much as possible (see Fig. 5.2). One reconstruction used the photons detected in the photopeak window combined with a triple energy window scatter correction (32 keV width centered at 159 keV for the photopeak window and 6.4 keV width at each side for scatter correction) and four additional reconstructions were done from different windows (32 keV width centered at 139, 119, 99 and 79 keV respectively). For the VRT simulated projection data, only primary photons were simulated and could thus be reconstructed, resulting in noise- and scatter-free SPECT scans (see Fig. 5.2).

5.2.3. Attenuation map estimation

Image preprocessing

Before being used as input to the neural networks, the MC simulated SPECT images were pre-processed. This includes a step of cylindrical masking (diameter 240 mm) to remove artefacts outside the head and a step of intensity-normalization to ensure a similar dynamic range for scans from different phantoms, as in [104]. Besides, the input SPECT images were down-sampled (tri-linearly) to a voxel size of $3 \times 3 \times 3$ mm^3 from an original voxel size of $1.5 \times 1.5 \times 1.5$ mm^3 before being fed into the neural network to speed up the training process with a relative larger image voxel size.

CNN architectures

The patch-voxel CNN that estimates μ-maps voxel-wise with an encoder architecture as implemented in our previous work was used [104]. Additionally, two networks with an encoder-decoder architecture that estimate μ-maps in a patch-wise or image-wise manner were tested. Such an encoder-decoder architecture has the advantage of preserving neighborhood information in the output space. For the three networks, 2D patches in the spatial domain (xy plane) were used as input. This is to avoid inter-slice interference particularly for slices close to the edge of the scanning region where neighboring slices might suffer from data truncation artefacts (note that there are only a limited number of slices in the scanning region due to the focused striatum imaging strategy). Each 2D patch underwent multiple stages of 2D convolutions and pooling (see Fig. 5.3). These three networks are explained in detail below.

1. Patch-voxel CNN: this network takes SPECT image patches centered at each voxel as input to predict the corresponding attenuation coefficient of the central voxel from each patch as output (see Fig. 5.3). The input image patch has a dimension of 21 × 21 voxels taken from the 2D transaxial slices × 5 energies, while the output has a dimension of 1 voxel.
2. Patch-patch CNN: this network takes SPECT image patches as input to predict the corresponding attenuation map patches at the same location in image space (see Fig. 5.3). The input SPECT patch dimensions were set to have an even dimension due to the down-sampling up-sampling operations with U-Net architecture. Thus, a dimension of 20 × 20 voxels × 5 energies was used as input with an output size of 20 × 20 voxels. In the testing phase, the entire 2D image slice was used in the network for prediction. Thus, the attenuation coefficient of each voxel was the mean value among predictions from all patches covering that voxel (20 × 20 patches).
3. Image-image CNN: this network has a U-Net architecture as in the patch-patch CNN, while here each slice (72 × 80 voxels × 5 energies) was used as input to predict the attenuation map for the corresponding slice (72 × 80 voxels).

Model training

Training was done on five randomly selected phantoms while testing was performed on the remaining 15 phantoms. All CNNs were trained with 15k samples randomly selected with replacement in each epoch. For the patch-voxel and patch-patch CNN, a balanced selection of the patches was ensured for the three main tissue classes (air, soft tissue and bone). Data augmentation was performed with random rotation (-20° to 20°) and translation (-10 to 10 mm). The networks were trained to minimize the mean square error between the predicted and the GT μ-map. The Adam optimizer [140] with default settings and a batch size of 15 was used in the training. No validation set was used to determine the optimal epoch. The network was trained for 200 epochs for convergence.

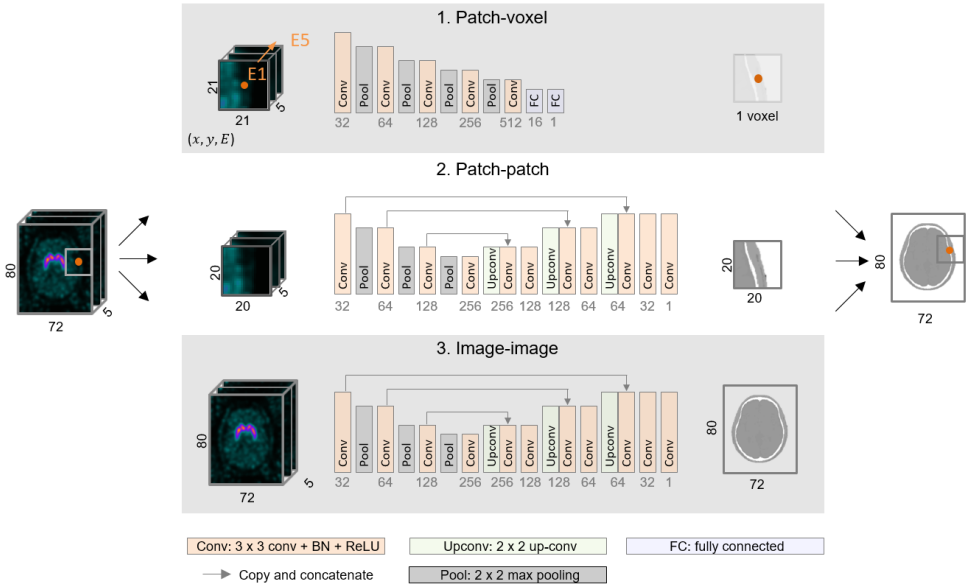

Figure 5.3: Network architecture of the patch-voxel, patch-patch and image-image CNN (Conv: 3 × 3 convolution; Pool: 2 × 2 max pooling; FC: fully connected; Upconv: 2 × 2 up-sampling). Every convolutional layer was followed with a layer of batch normalization and a layer of ReLU activation. Each fully connected layer was followed by a sigmoid activation. The number of filters is indicated in the figure below the layers.

This work was implemented using TensorFlow.

5.2.4. Correction using the μ-maps

Attenuation correction with the μ-maps was done using an adapted multi-pinhole first-order Chang's method [104]. This method first checks –at every bed position– if a voxel is seen by a pinhole. If yes, the transmission along the corresponding projection line (from that voxel center to the pinhole center) is counted and weighted by the pinhole's sensitivity for that voxel. The transmission fraction for the corresponding voxel is then the average transmission value among all projection lines that are counted.

5.2.5. Evaluation

Attenuation maps

The accuracy of the CNN estimated μ-map was evaluated by calculating the root mean square error (RMSE) defined in equation 5.1 and the normalized mean absolute difference (NMAE) given by equation 5.2 as in [23]. In the equations, n is number of voxels involved in the calculation for each scan. Only voxels in the head (i.e., soft tissue or bone) are taken into account. The symbols μ^{GT}_{max} and μ^{GT}_{min} are the respective maximum (μ = 0.232

for bone) and minimum intensities (μ = 0) of the ground truth μ-map.

$$RMSE\text{-}\mu = \sqrt{\frac{1}{n}\sum_{j=1}^{n}\left(\mu_j^{CNN} - \mu_j^{GT}\right)^2} \tag{5.1}$$

$$NMAE\text{-}\mu = \frac{1}{n \times (\mu_{max}^{GT} - \mu_{min}^{GT})}\sum_{j=1}^{n}|\mu_j^{CNN} - \mu_j^{GT}| \tag{5.2}$$

Attenuation corrected SPECT images

5.2.5.2.1 Visual inspection SPECT images that are corrected using the CNN estimated μ-maps (CNN-AC) were compared to the ground-truth-AC (GT-AC) image that uses the GT μ-maps for correction. All SPECT images shown in this paper for visual comparisons were smoothed using a 3D Gaussian post filter with 6 mm FWHM.

5.2.5.2.2 Relative quantification Relative quantification is done by calculating the regional striatal uptake ratios in localized regions of interest (ROIs). The specific binding ratio (SBR) and the asymmetry index (AI) were calculated as defined by

$$SBR = \frac{C_{target} - C_{bkg}}{C_{bkg}} \tag{5.3}$$

$$AI = 2 \times \frac{SBR_R - SBR_L}{SBR_R + SBR_L} \times 100\% \tag{5.4}$$

Here C_{target} and C_{bkg} are the mean DaT image intensity in the target ROI and the reference ROI respectively, while SBR_R and SBR_L refers to the SBR of a target ROI in the right and left hemisphere respectively. Eight localized sub-regions of the striatum were defined as the target ROI (see Fig. 5.4). These localized ROIs in the striatum were drawn with a diameter of 10.5 mm in the transaxial plane and were placed over 9 mm slices in the axial direction (thus each has a volume of 1 ml). The reference region was obtained using the Southampton method [69] (see Fig. 5.4).

The deviation for the SBRs and AIs calculated from the CNN-AC images were compared to those of GT-AC as in equation 5.5-5.6. In the equations, DEV_{SBR} and DEV_{AI} denote the SBR and AI deviations from the GT-AC image. The deviation of AI is calculated directly by subtracting the AI_{GT-AC} since AI is already a normalized index expressed in percentage.

$$DEV_{SBR}(\%) = \frac{|SBR_{CNN-AC} - SBR_{GT-AC}|}{SBR_{GT-AC}} \times 100\% \tag{5.5}$$

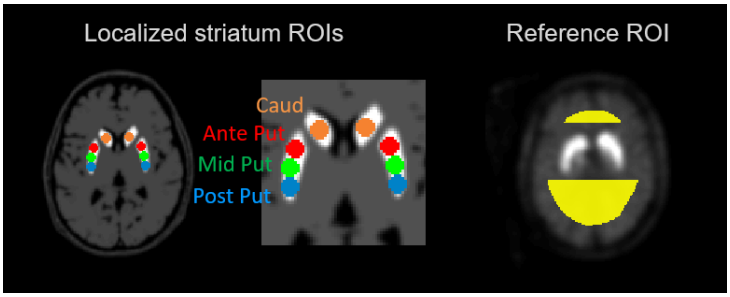

Figure 5.4: Illustration of the eight localizied regions and the reference ROI for quantitative analysis. Regions of caudate, anterior putamen, middle putamen and posterior putamen in the left and right hemisphere are depicted. Each region has a diameter of 10.5 mm and an axial length of 9 mm (thus a volume of about 1 ml). Caud: caudate; Ante Put: anterior putamen; Mid Put: middle putamen; Post Put: posterior putamen. The reference ROI was generated using the Southamoton method.

$$DEV_{AI}(\%) = |AI_{CNN-AC} - AI_{GT-AC}| \tag{5.6}$$

Besides evaluating the deviations, correlations between SBRs derived from images with different AC methods and those of the GT-AC were investigated. This is done by linear regression and comparison of the coefficient of determination (R^2) as in [166]. P values were computed using paired t tests to measure the statistical significance ($p < 0.05$ were considered statistically significant).

5.2.5.2.3 Absolute quantification Compared to relative quantification, absolute quantification assesses regional tracer concentrations rather than uptake ratio between regions. Absolute quantification is currently rarely implemented for DaTscans. Applications on PET and SPECT studies [167, 168] show potential value of such an assessment, thus we include it in the present work. Here, the standardized uptake values (SUVs) as often used for absolute quantitative analysis were calculated as shown in equation 5.7. The SUV (in units of g/ml) is the mean concentration (kBq/ml) from a ROI normalized by the injected dose per patient weight (kBq/g). The deviation for the SUVs calculated from the CNN-AC images were compared to those of GT-AC according to equation 5.8.

$$SUV = \frac{C_{target}}{Dose/weight} \tag{5.7}$$

$$DEV_{SUV}(\%) = \frac{|SUV_{CNN-AC} - SUV_{GT-AC}|}{SUV_{GT-AC}} \times 100\% \tag{5.8}$$

For both relative quantification and absolute quantitative analysis, measurements were performed on the unfiltered SPECT images to avoid any bias from filtering.

5.3. Results

5.3.1. Attenuation maps

Figure 5.5 gives a comparison of the CNN estimated and the GT μ-maps. Slices within an axial length of 48 mm that are essential for DaTscan inspection and quantification are displayed. The center of the striatum in axial direction is defined to be at 0 mm. Figure 5.5 shows that μ-maps can be accurately estimated with all the networks. Among the three CNNs, the patch-voxel CNN gives slightly more 'noisy' μ-maps. This (i.e., the 'noise' on the μ-map) is circumvented in the patch-patch and image-image CNNs where neighborhood information is preserved in the output space with an encoder-decoder framework.

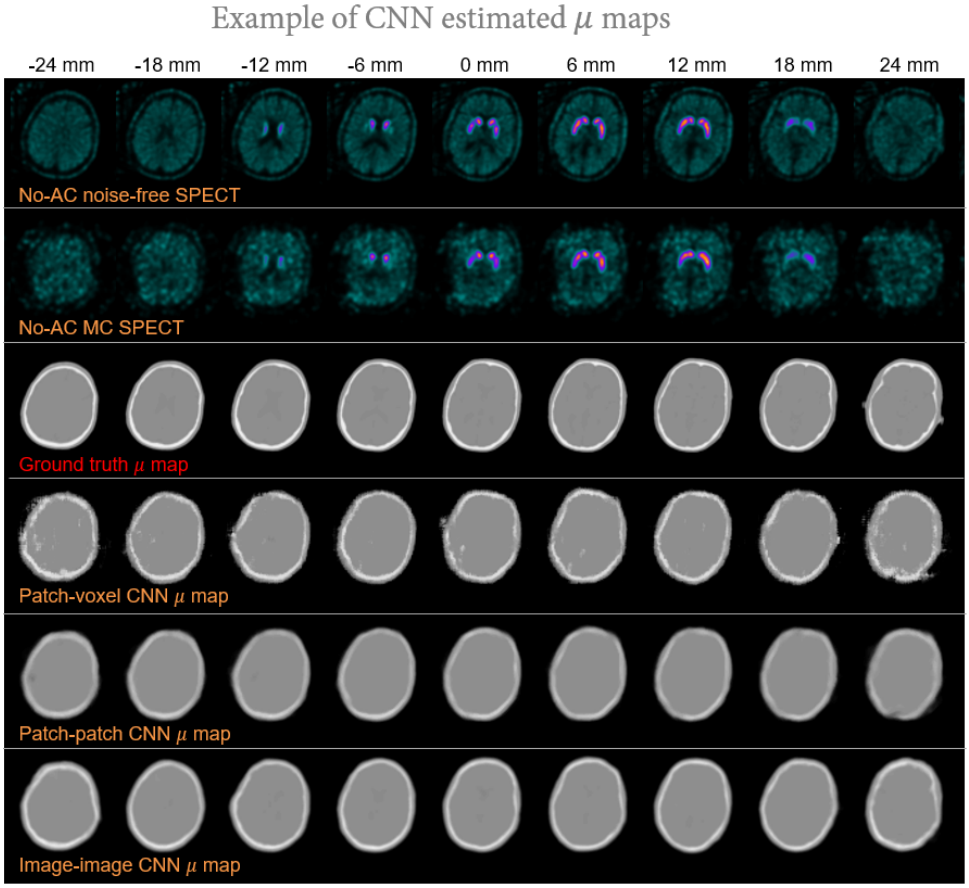

Figure 5.5: Comparison of the μ-maps obtained using different CNNs. Slices within an axial length of 48 mm that are essential for a DaTscan are shown.

Table 5.1 provides the NMAE and the RMSE results for the different CNN estimated μ-maps. Voxels for slices within the 48 mm axial range were used for the calculation. This table shows that NMAE and RMSE of the μ-map are small and comparable for the three

networks.

Table 5.1: Mean and standard deviations of NMAE and RMSE for the μ-maps obtained with various CNN methods. The errors were calculated from the slices within an axial length of 48 mm that are essential for DaTscan.

	NMAE-μ (%)	NMAE-μ ($\times 10^{-2} cm^{-1}$)
Patch-voxel CNN μ-map	4.53 ± 0.82	2.25 ± 0.40
Patch-patch CNN μ-map	4.16 ± 0.85	2.01 ± 0.40
Image-image CNN μ-map	4.07 ± 0.65	2.01 ± 0.31

5.3.2. Attenuation corrected SPECT images

Visual inspection

Figure 5.6 provides a visual comparison of the attenuation corrected SPECT images. To avoid the dominating effect of noise, SPECT images presented in the figure are the noise-free simulated scans which allows to focus on attenuation effects. Results of corrections performed on the realistic MC simulated scans are included in the appendix (Fig. 5.10).

Figure 5.6 shows that the striatum structure looks similar for all AC methods including No-AC. Compared to the GT-AC, the No-AC gives an increased activity distribution at the periphery and outside of the brain.

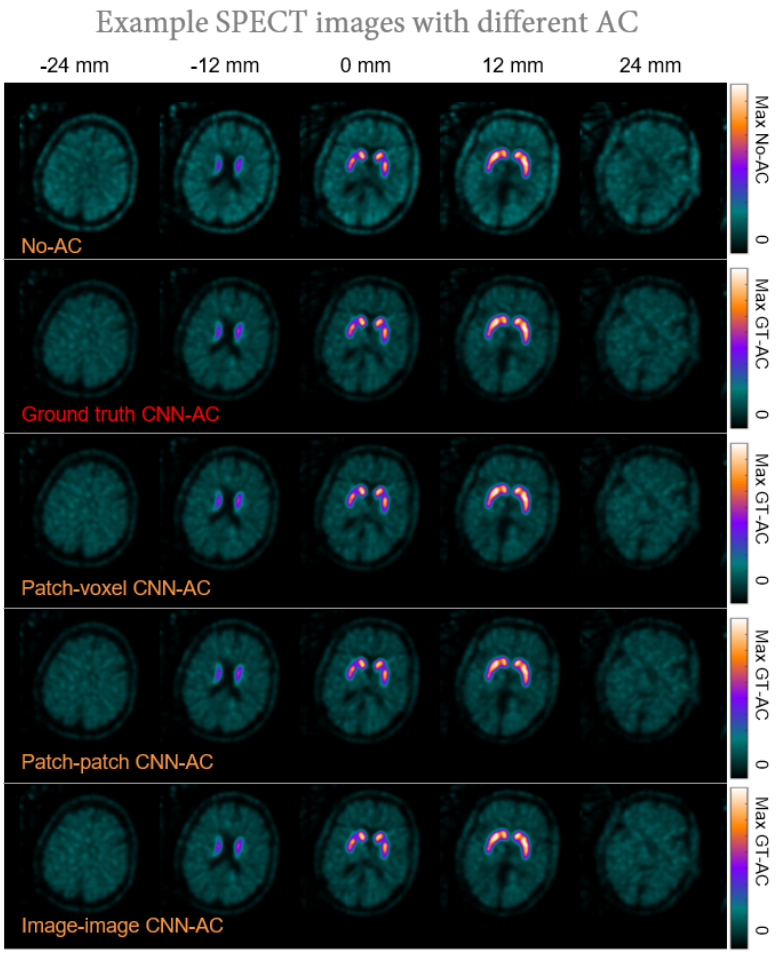

Figure 5.6: Comparison of the attenuation corrected SPECT images.

Relative quantification

Figure 5.7 gives Bland-Altman plots of the SBR differences from the GT-AC image across 120 regions (eight sub-regions for all 15 test subjects). The deviations in percentage for the SBRs and AIs are summarized in the figure. Figure 5.8 gives the scatter plot of the SBRs for correlation analysis.

Figure 5.7 shows the small differences between the three CNN-ACs and GT-AC for the SBRs (differences are close to the zero line). Among the three CNN methods, the patch-voxel CNN-AC shows a slightly more diverging distribution and thus a larger difference of the SBRs from GT-AC. The deviation from the GT-AC is ≤ 2.0% for all three CNN-ACs. No-AC underestimates SBRs by 10.9% systematically, as shown by the strong linear correlation (R^2 = 0.99, p < 0.001) between the GT-AC based SBRs and the values obtained

with No-AC in figure 5.8. The impact of different CNN-AC methods or No-AC on asymmetry index is small (within 3.2%).

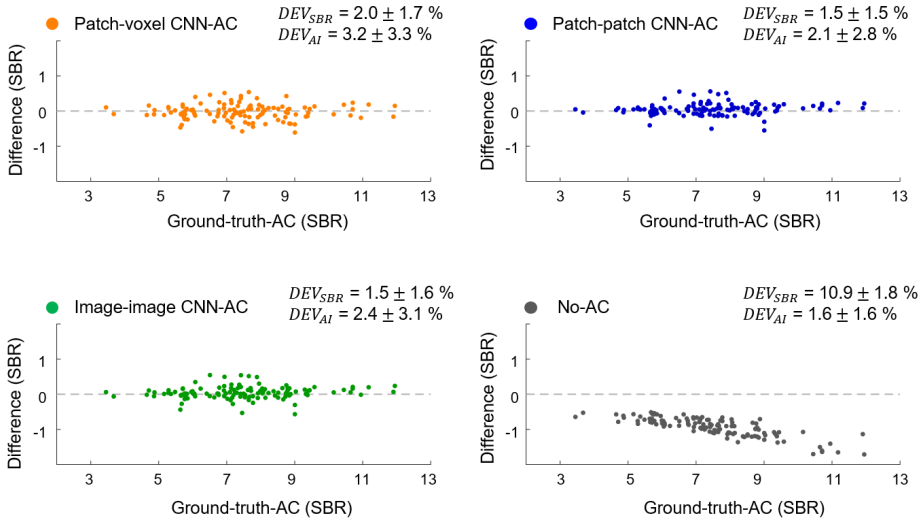

Figure 5.7: Bland-Altman plots when using different AC methods. Measurements taken from all 15 × 8 regions are plotted.

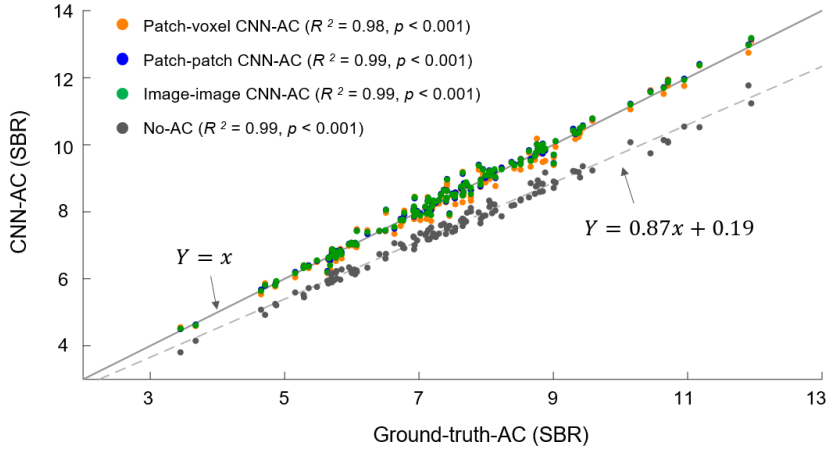

Figure 5.8: Correlation between GT-AC and CNN-ACs, as well as between GT-AC and No-AC for the SBRs; strong correlation ($R^2 > 0.98$, $p < 0.001$) are observed.

Absolute quantification

The capability to obtain accurate regional uptake values with different AC methods is shown in figure 5.9. The SUVs calculated from the phantoms are included as a reference. Figure 5.9 shows that compared to the digital phantom, the ground-truth-AC suffers from slight inaccurate estimation of the SUVs. This might be due to the partial volume effects or the imperfect attenuation correction method. Besides, the three CNN-AC methods achieve comparable SUV accuracies as the GT-AC. The deviation from the GT-AC was summarized in table 5.2, which shows a mean deviations of within 2.4% for all three CNN-ACs.

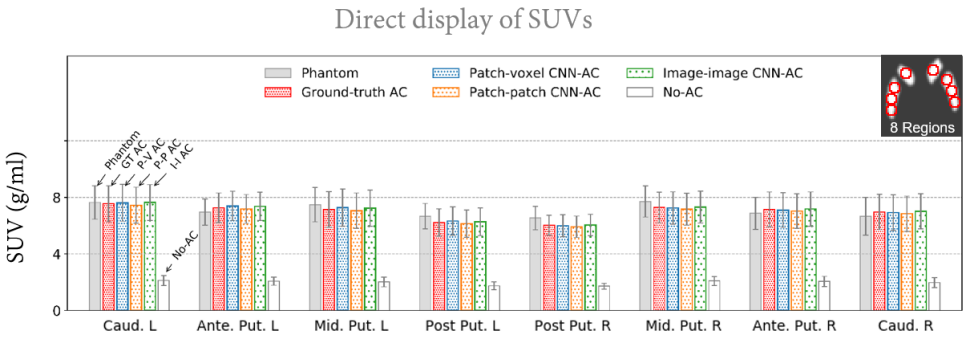

Figure 5.9: Comparison of the SUV measurements when using different AC methods in the eight sub-regions of the striatum. The mean and standard deviation across 15 test subjects are displayed for each region. Caud: caudate; Ante Put: anterior putamen; Mid Put: middle putamen; Post Put: posterior putamen.

Table 5.2: Deviation (mean ± standard deviation) of the SUVs from the GT-AC across 120 regions (8 sub-regions for all 15 subjects). The term 'PV', 'PP' and 'II' denotes patch-voxel, patch-patch and image-image respectively.

DEV_{SUV}(%)	Caudate		Ante. Put.		Mid. Put.		Post. Put.		**Mean**
	L	R	L	R	L	R	L	R	
PV CNN-AC	1.6 ± 1.5	1.4 ± 1.4	2.6 ± 2.9	1.9 ± 1.9	2.7 ± 3.0	2.0 ± 2.2	2.6 ± 2.8	2.0 ± 2.5	2.1 ± 1.3
PP CNN-AC	1.8 ± 1.5	2.3 ± 1.2	2.1 ± 1.2	2.8 ± 1.6	2.1 ± 1.2	2.9 ± 1.9	2.0 ± 1.2	3.1 ± 2.1	2.4 ± 1.5
II CNN-AC	1.7 ± 2.0	1.3 ± 1.3	2.2 ± 2.8	1.3 ± 2.0	2.2 ± 2.7	1.4 ± 2.3	2.0 ± 1.3	1.5 ± 2.5	1.7 ± 2.3
No-AC	72.1 ± 0.7	72.0 ± 0.6	71.7 ± 0.9	71.3 ± 0.7	71.9± 0.9	71.3 ± 0.7	71.9 ± 0.6	71.3 ± 0.7	71.7 ± 0.8

5.3.3. Computation

The training took about 1.8 h, 1.9 h and 1.2 h for the patch-voxel, patch-patch and image-image CNN respectively, when running on a single NVIDIA 2080 Ti graphics processing unit with 11 GB of memory. Testing was done in 28.4 s and 60.0 s and 1.3 s for the respective network to generate the attenuation map for each patient scan.

5.4. Discussion

In the present work, we demonstrated the feasibility of CNN based approaches for μ-map estimation using only SPECT data from axially focused DaTscans. The approaches were tested on a focusing multi-pinhole system in a Monte Carlo simulation study.

Our visual results show that AC does not affect the shape and symmetry of the striatum much. The main visual effect of AC is that the activity distribution at the periphery and outside of the brain can be well estimated, which may otherwise be incorrectly enhanced (as the No-AC images show). For relative quantification of the SBRs, deviations from the GT-AC were within 2.0% for CNN-AC. No-AC systematically underestimates SBRs by 10.9%. A highly linear correlation was observed between the GT-AC obtained SBRs and the values obtained with CNN-AC ($R^2 \geq 0.98$, $p < 0.001$) and No-AC ($R^2 = 0.99$, $p < 0.001$). Absolute quantification in terms of the SUV has a deviation from GT-AC of within 2.4% for CNN-AC and of 71.7% for No-AC.

Currently, the clinical value of AC for DaTscans is debated [54, 166]. Based on our results, the impact of AC is likely insignificant for diagnostic purposes when assessment is based on visual inspection of the striatum. This is aligned with previous findings [54, 169]. Likewise, omitting AC may not be an issue for relative quantification when DaTscans at a single clinical site are processed using the same protocols (e.g., all without AC), given the strong correlation between the GT-AC obtained SBRs and those of No-AC. However, in case that AC is a step in a standardized protocol or a precise measurement of the SBR is helpful (e.g., for multicenter studies where AC is already performed), AC can be performed. This is certainly true when absolute quantification is preferred. Absolute quantification (for which AC is required) is presently rarely applied on DaTscans. A recent study suggests that it can be helpful for differentiation of normal and pathological DaTscans [170]. In these cases, using the CNN estimated μ-map allows to obtain accurate results, without suffering from possible image registration errors and eliminating the need of manually drawing an ellipse. Apart from DaTscans, in other applications where a low activity level is present in the majority of the head, e.g., for tumor therapy imaging with ^{131}I-labeled 81C6 [171], a CNN may also be applied to estimate μ-maps for precise quantification of the tracer uptake.

In the present work, three CNN frameworks that estimate μ-map in a voxel-wise, patch-wise and image-wise way were tested for the task of interest. We found that incorporating neighboring information in the output space as with the patch-patch and image-image CNN could reduce noise of the μ-maps, which (i.e., the noise) appears with the patch-voxel CNN that estimates μ-maps voxel-wise. Among the three frameworks, the image-image architecture attained a slightly better performance in terms of NMAE and RMSE of the μ-maps and DEV_{SUV} and additionally has the advantage of fast computation in training and testing. The image-image CNN treats the image transformation problem (from multi-energy SPECT images to attenuation map) from a global view. In contrast, the

patch-voxel and patch-patch CNN take local regions and thus focus more on details. For DaTscans, the μ-maps essential for interpretation and quantification are 'oval-shaped' with rather simple structures. This might favor the use of a method as image-image CNN that ensures a global consistency. Nevertheless, the differences of quantification accuracy was small with the use of different CNN frameworks.

Our work shows that the CNNs can accurately estimate μ-maps even when only a few scans are used for training. This could make the method easily applicable in clinical practice, as a large number of training data are generally not readily available. However, a limitation of the present work lies in a lack of validation using patient scans. For a clinical implementation of the proposed method, we expect that the network may be trained on patient scans with CT attenuation maps acquired from a few subjects.

We used the noise-free VRT simulated scans to evaluate the effects of attenuation correction using different μ-maps (these μ-map themselves were all estimated based on the Monte Carlo data). Results of correction performed on the realistic MC simulated images are shown in the appendix (figure 5.10). For these realistically simulated scans in figure 5.10, noise has a large effect on image quality. Differences of using various CNN-AC methods are small and hardly noticeable.

5.5. Conclusion

We have demonstrated the feasibility of a CNN based approach to generate μ-maps using only SPECT data from ^{123}I-ioflupane DaTscans with a focused striatum scan strategy. Our results based on a Monte Carlo simulation study show that the impact of GT-AC versus CNN-AC or No-AC on striatal shape and symmetry is minimal. A strong correlation is observed between the GT-AC based SBRs and the values obtained with CNN-AC and No-AC. While SBRs and SUVs are underestimated by No-AC, they can be precisely quantified with CNN-AC. Thus, CNN estimated μ-map could be a promising substitute for CT μ-map, while further validation with patient scans in clinical cohorts is needed.

Appendix

Figure 5.10 displays the MC simulated realistic SPECT scans after attenuation correction with different μ-map. Quantitative analysis of the SUV deviations from the GT-AC for various CNN-AC methods are not performed on these MC simulated scans. These deviations read the same as those given in figure 5.7 where assessments were done on the noiseless VRT scans as the deviations depend only on the μ-map with the multi-pinhole Chang's attenuation correction method.

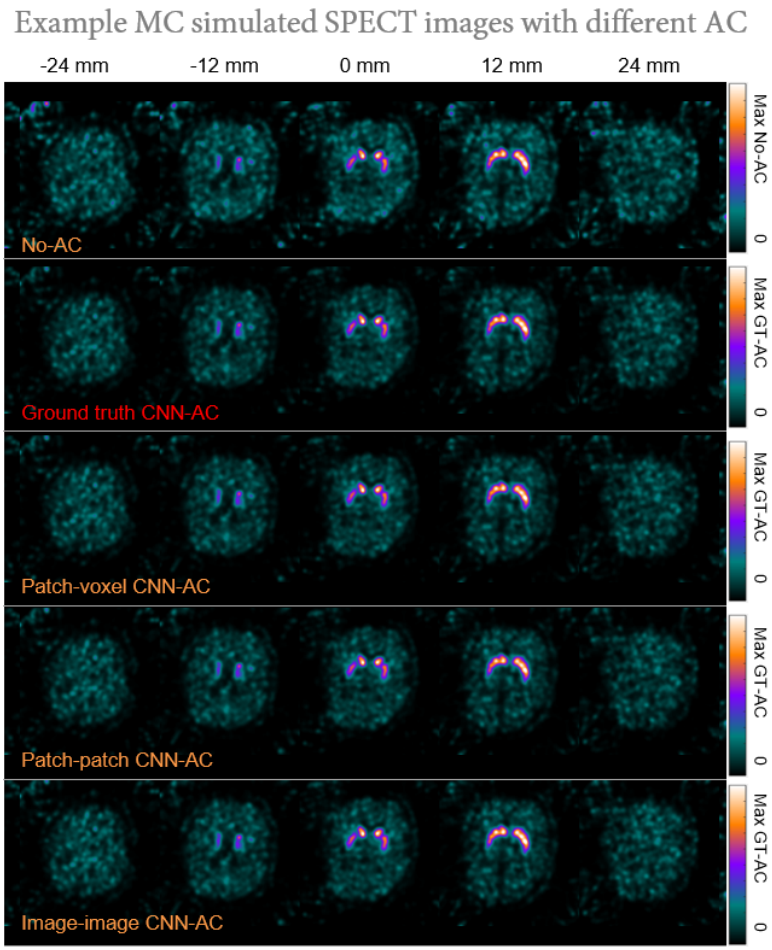

Figure 5.10: Comparison of the attenuation corrected images when using different μ-map for Monte Carlo simulated realistic SPECT scans. Slices within an axial length of 48 mm that are essential for DaTscan are displayed. Images were applied with a Gaussian filter of 6 mm FWHM.

6

Conclusion

Conventional dual-head SPECT with parallel-hole collimators suffers from limited spatial and temporal resolution, and limited sensitivity. Our group initially developed various multi-pinhole SPECT systems for preclinical purposes that are nowadays in use by hundreds of researchers worldwide. These systems are based on a full ring with stationary detectors applying multi-pinhole collimation. Lately this technology was translated in a prototype system named G-SPECT-I for clinical purposes. G-SPECT-I has demonstrated unprecedented resolutions in physical phantom scans when using a small-bore collimator dedicated to brain scanning. This thesis focuses on image acquisition optimization and attenuation map estimation for fast dynamic scanning and quantitatively accurate brain imaging. Meanwhile, we focus on DaTscan and brain perfusion imaging in this thesis as they are the two important brain SPECT applications.

The focusing multi-pinhole G-SPECT-I system scans an extended volume by gently translating the patient bed through the collimator to obtain sufficient sampling of the entire volume. A large number of bed translations could better warrant sampling sufficiency however at the cost of an increased overhead time needed for bed movement, which hampers fast dynamic studies. In Chapter 2, we developed a sampling strategy that employs a minimal number of bed translations for G-SPECT-I DaTscan imaging. Specifically, the scan region was confined in axial direction for partial brain imaging, while transaxially, we focused the bed positions in the brain and limited the number of transaxial bed positions while always ensuring sufficient sampling. Optimization of image acquisition with the use of different bed trajectories was performed with a simulation study. We found that structures essential for DaTscan assessment were barely affected even when using a very low number of bed translations (i.e., 4). We conclude that the proposed ac-

quisition plan could enable protocols for extremely fast dynamic SPECT DaTscans with less than half-minute time frames, which can be useful for efficient head motion correction.

While Chapter 2 presented optimized bed translation trajectories for focused partial brain imaging, Chapter 3 concentrated on whole brain imaging which is the common procedure for brain perfusion imaging. To this end, a series of scans using a reduced number of bed positions were simulated and compared to an oversampled reference scan acquired with a large number of bed translation (128 translations). We showed that the full brain perfusion images were barely affected by decreasing the number of bed positions from 128 down to 18. This bed trajectory entails a total overhead for bed movement of only half a minute, which may open up possibilities for fast dynamic whole brain SPECT and efficient motion correction.

Chapter 4 and 5 attempt to estimate attenuation maps which could be used for SPECT attenuation correction. In Chapter 4, we proposed a strategy to estimate attenuation maps using only SPECT data based on a convolutional neural network (CNN). We validated the proposed approach using Monte Carlo simulated brain perfusion scans with G-SPECT-I. Multiple image reconstructions were performed from different energy windows. Locally extracted 4D SPECT patches (three spatial plus one energy dimension) were used as input to the CNN which was trained to predict the attenuation coefficient of the corresponding central voxel of the patch. We showed that attenuation maps can be accurately estimated with the patch-voxel CNN method.

The promising results in Chapter 4 motivated us to apply a similar CNN approach for attenuation map estimation on the more challenging case of axially focused DaTscans in which only a low activity level is present outside the central region of the brain. The corresponding work was described in Chapter 5. In this Chapter, Monte Carlo simulation of DaTscans was performed using a protocol aimed at imaging a few slices centered at the striatum as proposed in Chapter 2. Apart from the patch-voxel CNN as implemented in Chapter 4, we also applied a patch-patch and image-image CNN that have been used in relevant recent studies to estimate attenuation maps. We concluded that all three CNNs can accurately estimate the attenuation maps for DaTscans , even though data was acquired with the focused striatum scanning strategy.

In this thesis, we optimized image acquisition and enabled accurate attenuation map estimation for a multi-pinhole SPECT system. This may, for the first time, allow for dynamic organ-specific clinical SPECT imaging at high spatial and temporal resolution. Additionally, the proposed sampling strategies, which were tested on G-SPECT-I brain scans, can be implemented for other future G-SPECT-I applications (e.g., pediatric imaging) or for other systems with a similar full ring multi-pinhole geometry (e.g., various preclinical systems of U-SPECT-II, VECTor, etc.). Similarly, the presented CNN based attenuation map estimation methods can essentially be applied on all other SPECT systems that have

list mode acquisition (the exact accuracy has yet to be assessed). A limitation of this thesis is a lack of evaluation using experimental scans. Also, further validation in clinical cohorts would be necessary to ultimately prove the benefit of the proposed method.

References

[1] Dicardiology, *https://www.dicardiology.com/article/spect-scanner-vs-pet-which-best/*, (2021), [last access: 24 March 2021].

[2] Stirrup, J. E. and Underwood, S. R., *Pet should not replace routine spect mps for the assessment of patients with known or suspected cad*, Journal of Nuclear Cardiology **24**, 1960 (2017).

[3] Gambhir, S. S., Berman, D. S., Ziffer, J., *et al.*, *A novel high-sensitivity rapid-acquisition single-photon cardiac imaging camera*, Journal of Nuclear Medicine **50**, 635 (2009).

[4] *Medical isotopes, global importance and opportunities for the netherlands*, .

[5] Cuocolo, A., Pappatà, S., Zampella, E., and Assante, R., *Advances in spect methodology*, International review of neurobiology **141**, 77 (2018).

[6] Kumar, A. and Chugani, H. T., *The role of radionuclide imaging in epilepsy, part 1: sporadic temporal and extratemporal lobe epilepsy*, Journal of Nuclear Medicine **54**, 1775 (2013).

[7] Ivashchenko, O., van der Have, F., Villena, J. L., *et al.*, *Quarter-millimeter-resolution molecular mouse imaging with u-spect+*, Molecular imaging **14**, 7290 (2015).

[8] Nguyen, M. P., Ramakers, R. M., Kamphuis, C., *et al.*, *Exirad-3d: Fast automated three-dimensional autoradiography*, Nuclear Medicine and Biology **86**, 59 (2020).

[9] Ozsahin, I., Chen, L., Könik, A., *et al.*, *The clinical utilities of multi-pinhole single photon emission computed tomography*, Quantitative Imaging in Medicine and Surgery **10**, 2006 (2020).

[10] Beekman, F. J., Van der Have, F., Goorden, M. C., *et al.*, *G-spect-i: a full ring high sensitivity and ultra-fast clinical molecular imaging system with <3 mm resolution [abstract]*, Eur J Nucl Med Mol Imaging (Suppl 1) **42**, S209 (2015).

[11] Klein, W., Barrett, H. H., Pang, I., *et al.*, *Fastspect: electrical and mechanical design of a high-resolution dynamic spect imager*, in *1995 IEEE Nuclear Science Symposium and Medical Imaging Conference Record*, Vol. 2 (IEEE, 1995) pp. 931–933.

[12] Van Audenhaege, K., Van Holen, R., Deprez, K., *et al.*, *Design of a static full-ring multi-pinhole collimator for brain spect*, in *2011 IEEE Nuclear Science Symposium Conference Record* (IEEE, 2011) pp. 4393–4397.

[13] Van Audenhaege, K., Vandenberghe, S., Deprez, K., Vandeghinste, B., and Van Holen, R., *Design and simulation of a full-ring multi-lofthole collimator for brain spect*, Physics in Medicine & Biology **58**, 6317 (2013).

[14] Vaissier, P. E., Goorden, M. C., Vastenhouw, B., *et al.*, *Fast spiral spect with stationary γ-cameras and focusing pinholes*, Journal of Nuclear Medicine **53**, 1292 (2012).

[15] Hutton, B. F., Buvat, I., and Beekman, F. J., *Review and current status of spect scatter correction*, Physics in Medicine & Biology **56**, R85 (2011).

[16] Ogawa, K., Harata, Y., Ichihara, T., Kubo, A., and Hashimoto, S., *A practical method for position-*

dependent compton-scatter correction in single photon emission ct, IEEE transactions on medical imaging **10**, 408 (1991).

[17] Goorden, M. C., van Roosmalen, J., van der Have, F., and Beekman, F. J., *Optimizing modelling in iterative image reconstruction for preclinical pinhole pet*, Physics in Medicine & Biology **61**, 3712 (2016).

[18] Vaissier, P., Beekman, F., and Goorden, M., *Similarity-regulation of os-em for accelerated spect reconstruction*, Physics in Medicine & Biology **61**, 4300 (2016).

[19] Beekman, F., *Restoration of computer-tomographic images with neural networks*, (WO/1993/006560, 1993).

[20] Zhang, W., Li, R., Deng, H., *et al.*, *Deep convolutional neural networks for multi-modality isointense infant brain image segmentation*, NeuroImage **108**, 214 (2015).

[21] Gong, K., Yang, J., Kim, K., *et al.*, *Attenuation correction for brain pet imaging using deep neural network based on dixon and zte mr images*, Physics in Medicine & Biology **63**, 125011 (2018).

[22] Liu, F., Jang, H., Kijowski, R., *et al.*, *A deep learning approach for 18 f-fdg pet attenuation correction*, EJNMMI physics **5**, 1 (2018).

[23] Shi, L., Onofrey, J. A., Liu, H., Liu, Y.-H., and Liu, C., *Deep learning-based attenuation map generation for myocardial perfusion spect*, European Journal of Nuclear Medicine and Molecular Imaging , 1 (2020).

[24] Yang, J., Shi, L., Wang, R., *et al.*, *Direct attenuation correction using deep learning for cardiac spect: A feasibility study*, Journal of Nuclear Medicine (2021).

[25] Gong, K., Guan, J., Liu, C.-C., and Qi, J., *Pet image denoising using a deep neural network through fine tuning*, IEEE Transactions on Radiation and Plasma Medical Sciences **3**, 153 (2018).

[26] Li, T., Zhang, M., Qi, W., Asma, E., and Qi, J., *Motion correction of respiratory-gated pet images using deep learning based image registration framework*, Physics in Medicine & Biology **65**, 155003 (2020).

[27] Chen, Y., Vastenhouw, B., Wu, C., Goorden, M. C., and Beekman, F. J., *Optimized image acquisition for dopamine transporter imaging with ultra-high resolution clinical pinhole spect*, Physics in Medicine & Biology **63**, 225002 (2018).

[28] Catafau, A. M. and Tolosa, E., *Impact of dopamine transporter spect using 123i-ioflupane on diagnosis and management of patients with clinically uncertain parkinsonian syndromes*, Movement disorders: official journal of the Movement Disorder Society **19**, 1175 (2004).

[29] O'Brien, J. T., Colloby, S., Fenwick, J., *et al.*, *Dopamine transporter loss visualized with fp-cit spect in the differential diagnosis of dementia with lewy bodies*, Archives of neurology **61**, 919 (2004).

[30] Hauser, R. A. and Grosset, D. G., *[123i] fp-cit (datscan) spect brain imaging in patients with suspected parkinsonian syndromes*, Journal of Neuroimaging **22**, 225 (2012).

[31] Bajaj, N., Hauser, R. A., and Grachev, I. D., *Clinical utility of dopamine transporter single photon emission ct (dat-spect) with (123i) ioflupane in diagnosis of parkinsonian syndromes*, Journal of Neurology, Neurosurgery & Psychiatry **84**, 1288 (2013).

[32] Park, E., *A new era of clinical dopamine transporter imaging using 123i-fp-cit*, Journal of nuclear medicine technology **40**, 222 (2012).

[33] Marzullo, P. and Mariani, G., *From Basic Cardiac Imaging to Image Fusion: Core Competencies*

Versus Technological Progress (Springer Science & Business Media, 2013).

[34] Lee, T.-C., Ellin, J. R., Huang, Q., *et al.*, *Multipinhole collimator with 20 apertures for a brain spect application*, Medical physics **41**, 112501 (2014).

[35] Kouris, K., Clarke, G. A., Jarritt, P. H., Townsend, C. E., and Thomas, S. N., *Physical performance evaluation of the toshiba gca-9300a triple-headed system*, Journal of Nuclear Medicine **34**, 1778 (1993).

[36] Kawamura, Y., Ashizaki, M., Saida, S., and Sugimoto, H., *Usefulness of rate of increase in spect counts in one-day method of n-isopropyl-4-iodoamphetamine [123 i] spect studies at rest and after acetazolamide challenge using a method for estimating time-dependent distribution at rest*, Annals of nuclear medicine **22**, 457 (2008).

[37] Deyn, P. P., A *textbook of: SPECT in neurology and psychiatry* (John Libbey Eurotext, 1997) p. p128.

[38] Bombardieri, E., Buscombe, J., Lucignani, G., and Schober, O., *Advances in nuclear oncology: diagnosis and therapy* (CRC Press, 2007) p. p472.

[39] Goorden, M., Rentmeester, M., and Beekman, F., *Theoretical analysis of full-ring multi-pinhole brain spect*, Physics in Medicine & Biology **54**, 6593 (2009).

[40] Van Audenhaege, K., Van Holen, R., Vanhove, C., and Vandenberghe, S., *Collimator design for a multipinhole brain spect insert for mri*, Medical physics **42**, 6679 (2015).

[41] Stoddart, H. and Stoddart, H., *New multidimensional reconstructions for the 12-detector, scanned focal point, single-photon tomograph*, Physics in Medicine & Biology **37**, 579 (1992).

[42] van de Giessen, E. and Booij, J., *The spect tracer [123 i] adam binds selectively to serotonin transporters: a double-blind, placebo-controlled study in healthy young men*, European journal of nuclear medicine and molecular imaging **37**, 1507 (2010).

[43] Sensakovic, W. F., Hough, M. C., and Kimbley, E. A., *Acr testing of a dedicated head spect unit*, Journal of applied clinical medical physics **15**, 1 (2014).

[44] Tavares, A., Batis, J., Barret, O., *et al.*, *In vivo evaluation of [(123) i] mni-420: a novel single photon emission computed tomography radiotracer for imaging of adenosine 2a receptors in brain.* Nuclear medicine and biology **40**, 403 (2013).

[45] Dierckx, R. A., Otte, A., De Vries, E. F., Van Waarde, A., and Luiten, P. G., *PET and SPECT of Neurobiological Systems* (Springer, 2014) p. p238.

[46] Mukherjee, J. M., Dey, J., and King, M. A., *Image reconstruction methods for i-123 datscan imaging using a multi-pinhole and fan collimator dual-headed spect system*, in *2014 IEEE Nuclear Science Symposium and Medical Imaging Conference (NSS/MIC)* (IEEE, 2014) pp. 1–3.

[47] King, M. A., Mukherjee, J. M., Könik, A., *et al.*, *Design of a multi-pinhole collimator for i-123 datscan imaging on dual-headed spect systems in combination with a fan-beam collimator*, IEEE transactions on nuclear science **63**, 90 (2016).

[48] Chen, L., Tsui, B. M., and Mok, G. S., *Design and evaluation of two multi-pinhole collimators for brain spect*, Annals of nuclear medicine **31**, 636 (2017).

[49] Vastenhouw, B. and Beekman, F., *Submillimeter total-body murine imaging with u-spect-i*, Journal of Nuclear Medicine **48**, 487 (2007).

[50] Ivashchenko, O., van der Have, F., Goorden, M. C., Ramakers, R. M., and Beekman, F. J., *Ultra-high-sensitivity submillimeter mouse spect*, Journal of Nuclear Medicine **56**, 470 (2015).

[51] Hammers, A., Allom, R., Koepp, M. J., *et al.*, *Three-dimensional maximum probability atlas of the human brain, with particular reference to the temporal lobe*, Human brain mapping **19**, 224 (2003).

[52] Koch, W., Radau, P. E., Hamann, C., and Tatsch, K., *Clinical testing of an optimized software solution for an automated, observer-independent evaluation of dopamine transporter spect studies*, Journal of Nuclear Medicine **46**, 1109 (2005).

[53] Acton, P. D., Newberg, A., Plössl, K., and Mozley, P. D., *Comparison of region-of-interest analysis and human observers in the diagnosis of parkinson's disease using [99mtc] trodat-1 and spect*, Physics in Medicine & Biology **51**, 575 (2006).

[54] Lange, C., Seese, A., Schwarzenböck, S., *et al.*, *Ct-based attenuation correction in i-123-ioflupane spect*, PloS one **9**, e108328 (2014).

[55] Augimeri, A., Cherubini, A., Cascini, G. L., *et al.*, *Cada—computer-aided datscan analysis*, EJNMMI physics **3**, 1 (2016).

[56] Branderhorst, W., Vastenhouw, B., Van Der Have, F., *et al.*, *Targeted multi-pinhole spect*, European journal of nuclear medicine and molecular imaging **38**, 552 (2011).

[57] Van Der Have, F., Vastenhouw, B., Ramakers, R. M., *et al.*, *U-spect-ii: an ultra-high-resolution device for molecular small-animal imaging*, Journal of Nuclear Medicine **50**, 599 (2009).

[58] Noo, F., Defrise, M., Clackdoyle, R., and Kudo, H., *Image reconstruction from fan-beam projections on less than a short scan*, Physics in medicine & biology **47**, 2525 (2002).

[59] Noo, F., Defrise, M., Pack, J. D., and Clackdoyle, R., *Image reconstruction from truncated data in single-photon emission computed tomography with uniform attenuation*, Inverse Problems **23**, 645 (2007).

[60] Chan, C., Dey, J., Grobshtein, Y., *et al.*, *The impact of system matrix dimension on small fov spect reconstruction with truncated projections*, Medical physics **43**, 213 (2016).

[61] Hodge, M. R., Horton, W., Brown, T., *et al.*, *Connectomedb—sharing human brain connectivity data*, Neuroimage **124**, 1102 (2016).

[62] Schneider, C. A., Rasband, W. S., and Eliceiri, K. W., *Nih image to imagej: 25 years of image analysis*, Nature methods **9**, 671 (2012).

[63] van der Have, F., Vastenhouw, B., Rentmeester, M., and Beekman, F. J., *System calibration and statistical image reconstruction for ultra-high resolution stationary pinhole spect*, IEEE transactions on medical imaging **27**, 960 (2008).

[64] Beekman, F. J., van der Have, F., Vastenhouw, B., *et al.*, *U-spect-i: a novel system for submillimeter-resolution tomography with radiolabeled molecules in mice*, Journal of Nuclear Medicine **46**, 1194 (2005).

[65] Goorden, M. C., van der Have, F., Kreuger, R., *et al.*, *Vector: a preclinical imaging system for simultaneous submillimeter spect and pet*, Journal of Nuclear Medicine **54**, 306 (2013).

[66] van der Have, F., Ivashchenko, O., Goorden, M. C., Ramakers, R. M., and Beekman, F. J., *High-resolution clustered pinhole 131iodine spect imaging in mice*, Nuclear medicine and biology **43**, 506 (2016).

[67] Siddon, R. L., *Fast calculation of the exact radiological path for a three-dimensional ct array*, Medical physics **12**, 252 (1985).

[68] Wang, B., van Roosmalen, J., Piët, L., *et al.*, *Voxelized ray-tracing simulation dedicated to multi-*

pinhole molecular breast tomosynthesis, Biomedical Physics & Engineering Express **3**, 045021 (2017).

[69] Tossici-Bolt, L., Hoffmann, S. M., Kemp, P. M., Mehta, R. L., and Fleming, J. S., *Quantification of [123 i] fp-cit spect brain images: an accurate technique for measurement of the specific binding ratio*, European journal of nuclear medicine and molecular imaging **33**, 1491 (2006).

[70] Chen, Y., Goorden, M. C., Vastenhouw, B., and Beekman, F. J., *Optimized sampling for high resolution multi-pinhole brain spect with stationary detectors*, Physics in Medicine & Biology **65**, 015002 (2020).

[71] Catafau, A. M., *Brain spect in clinical practice. part i: perfusion*, Journal of Nuclear Medicine **42**, 259 (2001).

[72] Juni, J. E., Waxman, A. D., Devous, M. D., *et al.*, *Procedure guideline for brain perfusion spect using 99mtc radiopharmaceuticals* 3.0, Journal of nuclear medicine technology **37**, 191 (2009).

[73] Knowlton, R. C., *The role of fdg-pet, ictal spect, and meg in the epilepsy surgery evaluation*, Epilepsy & Behavior **8**, 91 (2006).

[74] Kim, S. and Mountz, J. M., *Spect imaging of epilepsy: an overview and comparison with f-18 fdg pet*, International journal of molecular imaging **2011** (2011).

[75] Camargo, E. E., *Brain spect in neurology and psychiatry*, Journal of Nuclear Medicine **42**, 611 (2001).

[76] Amen, D. G., Trujillo, M., Newberg, A., *et al.*, *Brain spect imaging in complex psychiatric cases: an evidence-based, underutilized tool*, The open neuroimaging journal **5**, 40 (2011).

[77] Santra, A. and Kumar, R., *Brain perfusion single photon emission computed tomography in major psychiatric disorders: From basics to clinical practice*, Indian journal of nuclear medicine: IJNM: the official journal of the Society of Nuclear Medicine, India **29**, 210 (2014).

[78] Amen, D. G., Prunella, J. R., Fallon, J. H., Amen, B., and Hanks, C., *A comparative analysis of completed suicide using high resolution brain spect imaging*, The Journal of neuropsychiatry and clinical neurosciences **21**, 430 (2009).

[79] Amen, D. G., *Change Your Brain, Change Your Life (Revised and Expanded): The Breakthrough Program for Conquering Anxiety, Depression, Obsessiveness, Lack of Focus, Anger, and Memory Problems* (Harmony, 2015).

[80] Fakhri, G. E., Ouyang, J., Zimmerman, R. E., Fischman, A. J., and Kijewski, M. F., *Performance of a novel collimator for high-sensitivity brain spect*, Medical physics **33**, 209 (2006).

[81] Stam, M., Verwer, E., Booij, J., *et al.*, *Performance evaluation of a novel brain-dedicated spect system*, EJNMMI physics **5**, 1 (2018).

[82] Befera, N. T., Badea, C. T., and Johnson, G. A., *Comparison of 4d-microspect and microct for murine cardiac function*, Molecular imaging and biology **16**, 235 (2014).

[83] Beekman, F., *Gamma radiation imaging apparatus*, (US Patents US9168014B2, 2013).

[84] Zubal, I. G., Harrell, C. R., Smith, E. O., *et al.*, *Computerized three-dimensional segmented human anatomy*, Medical physics **21**, 299 (1994).

[85] Glick, S. J. and Soares, E. J., *Noise characteristics of mlem spect reconstruction with a mismatched projector-backprojector pair*, in *1997 IEEE Nuclear Science Symposium Conference Record*, Vol. 2 (IEEE, 1997) pp. 1518–1522.

[86] Stodilka, R. Z., Kemp, B. J., Prato, F. S., *et al.*, *Scatter and attenuation correction for brain spect*

using attenuation distributions inferred from a head atlas, Journal of Nuclear Medicine **41**, 1569 (2000).

[87] Pato, L. R., Vandenberghe, S., Zedda, T., and Van Holen, R., *Parallel-hole collimator concept for stationary spect imaging*, Physics in Medicine & Biology **60**, 8791 (2015).

[88] Van Laere, K., Koole, M., Kauppinen, T., *et al.*, *Nonuniform transmission in brain spect using 201tl, 153gd, and 99mtc static line sources: anthropomorphic dosimetry studies and influence on brain quantification*, Journal of Nuclear Medicine **41**, 2051 (2000).

[89] Nobili, F., Koulibaly, M., Vitali, P., *et al.*, *Brain perfusion follow-up in alzheimer's patients during treatment with acetylcholinesterase inhibitors*, Journal of Nuclear Medicine **43**, 983 (2002).

[90] Bowen, J. D., Huang, Q., Gullberg, G. T., and Seo, Y., *Phantom measurements and simulations of cardiac and brain studies using a multipinhole collimator with 20 apertures*, in *2011 IEEE Nuclear Science Symposium Conference Record* (IEEE, 2011) pp. 3417–3421.

[91] Charpentier, P., Lavenu, I., Defebvre, L., *et al.*, *Alzheimer's disease and frontotemporal dementia are differentiated by discriminant analysis applied to 99mtc hmpao spect data*, Journal of Neurology, Neurosurgery & Psychiatry **69**, 661 (2000).

[92] Tsolaki, M., Sakka, V., Gerasimou, G., *et al.*, *Correlation of rcbf (spect), csf tau, and congnitive function in patients with dementia of the alzheimer's type, other types of dementia, and congrol subjects*, American Journal of Alzheimer's Disease & Other Dementias® **16**, 21 (2001).

[93] Staffen, W., Schönauer, U., Zauner, H., *et al.*, *Brain perfusion spect in patients with mild cognitive impairment and alzheimer's disease: comparison of a semiquantitative and a visual evaluation*, Journal of neural transmission **113**, 195 (2006).

[94] McNeill, R., Sare, G., Manoharan, M., *et al.*, *Accuracy of single-photon emission computed tomography in differentiating frontotemporal dementia from alzheimer's disease*, Journal of Neurology, Neurosurgery & Psychiatry **78**, 350 (2007).

[95] Colloby, S. J., Taylor, J. P., Firbank, M. J., *et al.*, *Covariance 99mtc-exametazime spect patterns in alzheimer's disease and dementia with lewy bodies: utility in differential diagnosis*, Journal of geriatric psychiatry and neurology **23**, 54 (2010).

[96] Grova, C., Biraben, A., Scarabin, J.-M., *et al.*, *A methodology to validate mri/spect registration methods using realistic simulated spect data*, in *International Conference on Medical Image Computing and Computer-Assisted Intervention* (Springer, 2001) pp. 275–282.

[97] Radau, P. E., Slomka, P. J., Julin, P., Svensson, L., and Wahlund, L.-O., *Evaluation of linear registration algorithms for brain spect and the errors due to hypoperfusion lesions*, Medical Physics **28**, 1660 (2001).

[98] Cutolo, M., Nobili, F., Sulli, A., *et al.*, *Evidence of cerebral hypoperfusion in scleroderma patients*, Rheumatology **39**, 1366 (2000).

[99] Chiu, N.-T., Chang, Y.-C., Lee, B.-F., Huang, C.-C., and Wang, S.-T., *Differences in 99m tc-hmpao brain spet perfusion imaging between tourette's syndrome and chronic tic disorder in children*, European journal of nuclear medicine **28**, 183 (2001).

[100] Mountz, J. M., Bradley, L. A., Modell, J. G., *et al.*, *Fibromyalgia in women*, Arthritis & Rheumatism: Official Journal of the American College of Rheumatology **38**, 926 (1995).

[101] Deutsch, G., Mountz, J. M., Katholi, C. R., Liu, H.-G., and Harrell, L. E., *Regional stability of cerebral blood flow measured by repeated technetium-99m-hmpao spect: implications for the*

study of state-dependent change, Journal of Nuclear Medicine **38**, 6 (1997).

[102] Cao, Z., Maunoury, C., Chen, C. C., and Holder, L. E., *Comparison of continuous step-and-shoot versus step-and-shoot acquisition spect*, Journal of Nuclear Medicine **37**, 2037 (1996).

[103] Mohseni, M., Faghihi, R., Haghighatafshar, M., and Entezarmahdi, S. M., *Effects of the attenuation correction and reconstruction method parameters on conventional cardiac dynamic spect*, Medicine **97** (2018).

[104] Chen, Y., Goorden, M. C., and Beekman, F. J., *Automatic attenuation map estimation from spect data only for brain perfusion scans using convolutional neural networks*, Physics in Medicine & Biology **66**, 065006 (2021).

[105] Modzelewski, R., Janvresse, E., de la Rue, T., and Vera, P., *Comparison of heterogeneity quantification algorithms for brain spect perfusion images*, EJNMMI research **2**, 1 (2012).

[106] Larsson, A., Johansson, L., Sundström, T., and ÅHLSTRÖM, K. R., *A method for attenuation and scatter correction of brain spect based on computed tomography images*, Nuclear medicine communications **24**, 411 (2003).

[107] Bateman, T. M. and Cullom, S. J., *Attenuation correction single-photon emission computed tomography myocardial perfusion imaging*, in *Seminars in nuclear medicine*, Vol. 35 (Elsevier, 2005) pp. 37–51.

[108] Nakano, S., Kinoshita, K., Jinnouchi, S., Hoshi, H., and Watanabe, K., *Dynamic spect with iodine-123 imp in meningiomas*, J Nucl Med **29**, 1632 (1988).

[109] Ogasawara, K., Ogawa, A., Ezura, M., *et al.*, *Dynamic and static 99mtc-ecd spect imaging of subacute cerebral infarction: comparison with 133xe spect*, Journal of Nuclear Medicine **42**, 543 (2001).

[110] Komatani, A., Sugai, Y., and Hosoya, T., *Development of "super rapid dynamic spect," and analysis of retention process of 99m tc-ecd in ischemie lesions: Comparative study with 133 xe spect*, Annals of nuclear medicine **18**, 489 (2004).

[111] Gullberg, G. T., Reutter, B. W., Sitek, A., Maltz, J. S., and Budinger, T. F., *Dynamic single photon emission computed tomography—basic principles and cardiac applications*, Physics in Medicine & Biology **55**, R111 (2010).

[112] Knutsson, L., Börjesson, S., Larsson, E.-M., *et al.*, *Absolute quantification of cerebral blood flow in normal volunteers: Correlation between xe-133 spect and dynamic susceptibility contrast mri*, Journal of Magnetic Resonance Imaging: An Official Journal of the International Society for Magnetic Resonance in Medicine **26**, 913 (2007).

[113] Dahlbom, M., Reed, J., and Young, J., *Implementation of true continuous bed motion in 2-d and 3-d whole-body pet scanning*, IEEE Transactions on Nuclear Science **48**, 1465 (2001).

[114] Brasse, D., Newport, D., Carney, J., *et al.*, *Continuous bed motion acquisition on a whole body combined pet/ct system*, in *2002 IEEE nuclear science symposium conference record*, Vol. 2 (IEEE, 2002) pp. 951–955.

[115] Newport, D. F., Casey, M. E., Luk, W. K., and Reed, J. H., *Continuous tomography bed motion data processing apparatus and method*, (2005), uS Patent 6,915,004.

[116] Bailey, D. L. and Willowson, K. P., *An evidence-based review of quantitative spect imaging and potential clinical applications*, Journal of nuclear medicine **54**, 83 (2013).

[117] King, M. A., Glick, S. J., Pretorius, P. H., *et al.*, *Attenuation, scatter, and spatial resolution com-*

pensation in spect, in *Emission tomography: The fundamentals of PET and SPECT* (Academic, 2004) pp. 473–498.

[118] Goetze, S., Brown, T. L., Lavely, W. C., Zhang, Z., and Bengel, F. M., *Attenuation correction in myocardial perfusion spect/ct: effects of misregistration and value of reregistration*, Journal of Nuclear Medicine **48**, 1090 (2007).

[119] Berker, Y. and Li, Y., *Attenuation correction in emission tomography using the emission data—a review*, Medical physics **43**, 807 (2016).

[120] Zaidi, H. and Hasegawa, B., *Determination of the attenuation map in emission tomography*, Journal of Nuclear Medicine **44**, 291 (2003).

[121] Macey, D., Denardo, G. L., and DeNardo, S., *Comparison of three boundary detection methods for spect using compton scattered photons*, Journal of nuclear medicine **29**, 203 (1988).

[122] Wallis, J. W., Miller, T. R., and Koppel, P., *Attenuation correction in cardiac spect without a transmission measurement*, Journal of Nuclear Medicine **36**, 506 (1995).

[123] Pan, T.-S., King, M. A., De Vries, D. J., and Ljungberg, M., *Segmentation of the body and lungs from compton scatter and photopeak window data in spect: a monte-carlo investigation*, IEEE transactions on medical imaging **15**, 13 (1996).

[124] Younes, R. B., Mas, J., and Bidet, R., *A fully automated contour detection algorithm the preliminary step for scatter and attenuation compensation in spect*, European journal of nuclear medicine **14**, 586 (1988).

[125] Jha, A. K., Clarkson, E., Kupinski, M. A., and Barrett, H. H., *Joint reconstruction of activity and attenuation map using lm spect emission data*, in *Medical imaging 2013: physics of medical imaging*, Vol. 8668 (International Society for Optics and Photonics, 2013) p. 86681W.

[126] Brusaferri, L., Bousse, A., Emond, E. C., *et al.*, *Joint activity and attenuation reconstruction from multiple energy window data with photopeak scatter re-estimation in non-tof 3-d pet*, IEEE Transactions on Radiation and Plasma Medical Sciences **4**, 410 (2020).

[127] Leynes, A. P., Yang, J., Wiesinger, F., *et al.*, *Zero-echo-time and dixon deep pseudo-ct (zedd ct): direct generation of pseudo-ct images for pelvic pet/mri attenuation correction using deep convolutional neural networks with multiparametric mri*, Journal of Nuclear Medicine **59**, 852 (2018).

[128] Mok, G. S., Zhang, Q., Cun, X., *et al.*, *Initial investigation of using a generative adversarial network for denoising in dual gating myocardial perfusion spect*, in *2018 IEEE Nuclear Science Symposium and Medical Imaging Conference Proceedings (NSS/MIC)* (IEEE, 2018) pp. 1–3.

[129] Wang, G., Li, W., Ourselin, S., and Vercauteren, T., *Automatic brain tumor segmentation based on cascaded convolutional neural networks with uncertainty estimation*, Frontiers in computational neuroscience **13**, 56 (2019).

[130] Shiri, I., Arabi, H., Geramifar, P., *et al.*, *Deep-jasc: joint attenuation and scatter correction in whole-body 18 f-fdg pet using a deep residual network*, European journal of nuclear medicine and molecular imaging **47**, 2533 (2020).

[131] Reimold, M., Nikolaou, K., Christian La Fougère, M., and Gatidis, S., *18 independent brain f-fdg pet attenuation correction using a deep learning approach with generative adversarial networks*, Hellenic journal of nuclear medicine **22**, 179 (2019).

[132] Liu, M., Cheng, D., Wang, K., and Wang, Y., *Multi-modality cascaded convolutional neural net-*

works for alzheimer's disease diagnosis, Neuroinformatics **16**, 295 (2018).

[133] Guo, Z., Li, X., Huang, H., Guo, N., and Li, Q., *Medical image segmentation based on multi-modal convolutional neural network: Study on image fusion schemes*, in *2018 IEEE 15th International Symposium on Biomedical Imaging (ISBI 2018)* (IEEE, 2018) pp. 903–907.

[134] Ronneberger, O., Fischer, P., and Brox, T., *U-net: Convolutional networks for biomedical image segmentation*, in *International Conference on Medical image computing and computer-assisted intervention* (Springer, 2015) pp. 234–241.

[135] Aubert-Broche, B., Griffin, M., Pike, G. B., Evans, A. C., and Collins, D. L., *Twenty new digital brain phantoms for creation of validation image data bases*, IEEE transactions on medical imaging **25**, 1410 (2006).

[136] NIST, *National institute of standards technology*, (2020), [last access: Sep 2020].

[137] Jan, S., Santin, G., Strul, D., *et al.*, *Gate: a simulation toolkit for pet and spect*, Physics in Medicine & Biology **49**, 4543 (2004).

[138] Nguyen, M. P., Goorden, M. C., Kamphuis, C., and Beekman, F. J., *Evaluation of pinhole collimator materials for micron-resolution ex vivo spect*, Physics in Medicine & Biology **64**, 105017 (2019).

[139] Moeskops, P., Viergever, M. A., Mendrik, A. M., *et al.*, *Automatic segmentation of mr brain images with a convolutional neural network*, IEEE transactions on medical imaging **35**, 1252 (2016).

[140] Kingma, D. P. and Ba, J., *Adam: A method for stochastic optimization*, arXiv preprint arXiv:1412.6980 (2014).

[141] Paix, D., *Pinhole imaging of gamma rays*, Physics in Medicine & Biology **12**, 489 (1967).

[142] Collins, D. L., Zijdenbos, A. P., Kollokian, V., *et al.*, *Design and construction of a realistic digital brain phantom*, IEEE transactions on medical imaging **17**, 463 (1998).

[143] Tzourio-Mazoyer, N., Landeau, B., Papathanassiou, D., *et al.*, *Automated anatomical labeling of activations in spm using a macroscopic anatomical parcellation of the mni mri single-subject brain*, Neuroimage **15**, 273 (2002).

[144] Yang, J., Park, D., Gullberg, G. T., and Seo, Y., *Joint correction of attenuation and scatter in image space using deep convolutional neural networks for dedicated brain 18f-fdg pet*, Physics in medicine & biology **64**, 075019 (2019).

[145] Ramon, A. J., Yang, Y., Pretorius, P. H., *et al.*, *Initial investigation of low-dose spect-mpi via deep learning*, in *2018 IEEE nuclear science symposium and medical imaging conference proceedings (NSS/MIC)* (IEEE, 2018) pp. 1–3.

[146] Zhang, Q., Sun, J., and Mok, G. S., *Low dose spect image denoising using a generative adversarial network*, arXiv preprint arXiv:1907.11944 (2019).

[147] Reymann, M. P., Würfl, T., Ritt, P., *et al.*, *U-net for spect image denoising*, in *2019 IEEE Nuclear Science Symposium and Medical Imaging Conference (NSS/MIC)* (IEEE) pp. 1–2.

[148] Djang, D. S., Janssen, M. J., Bohnen, N., *et al.*, *Snm practice guideline for dopamine transporter imaging with 123i-ioflupane spect 1.0*, Journal of Nuclear Medicine **53**, 154 (2012).

[149] Winogrodzka, A., Bergmans, P., Booij, J., *et al.*, *[123 i] fp-cit spect is a useful method to monitor the rate of dopaminergic degeneration in early-stage parkinson's disease*, Journal of neural transmission **108**, 1011 (2001).

[150] Darcourt, J., Booij, J., Tatsch, K., *et al.*, *Eanm procedure guidelines for brain neurotransmission spect using 123 i-labelled dopamine transporter ligands, version 2*, European journal of nuclear medicine and molecular imaging **37**, 443 (2010).

[151] Rajeevan, N., Zubal, I. G., Ramsby, S. Q., *et al.*, *Significance of nonuniform attenuation correction in quantitative brain spect imaging*, Journal of Nuclear Medicine **39**, 1719 (1998).

[152] Crespo, C., Gallego, J., Cot, A., *et al.*, *Quantification of dopaminergic neurotransmission spect studies with 123 i-labelled radioligands. a comparison between different imaging systems and data acquisition protocols using monte carlo simulation*, European journal of nuclear medicine and molecular imaging **35**, 1334 (2008).

[153] Rahmim, A., Huang, P., Shenkov, N., *et al.*, *Improved prediction of outcome in parkinson's disease using radiomics analysis of longitudinal dat spect images*, NeuroImage: Clinical **16**, 539 (2017).

[154] Censor, Y., Gustafson, D. E., Lent, A., and Tuy, H., *A new approach to the emission computerized tomography problem: simultaneous calculation of attenuation and activity coefficients*, IEEE Transactions on Nuclear Science **26**, 2775 (1979).

[155] Nuyts, J., Dupont, P., Stroobants, S., *et al.*, *Simultaneous maximum a posteriori reconstruction of attenuation and activity distributions from emission sinograms*, IEEE transactions on medical imaging **18**, 393 (1999).

[156] Krol, A., Bowsher, J. E., Manglos, S. H., *et al.*, *An em algorithm for estimating spect emission and transmission parameters from emission data only*, IEEE transactions on medical imaging **20**, 218 (2001).

[157] Welch, A., Campbell, C., Clackdoyle, R., *et al.*, *Accurate attenuation correction in pet without accurate transmission measurements*, in *1997 IEEE Nuclear Science Symposium Conference Record*, Vol. 2 (IEEE, 1997) pp. 1697–1701.

[158] Bronnikov, A. V., *Reconstruction of attenuation map using discrete consistency conditions*, IEEE transactions on medical imaging **19**, 451 (2000).

[159] Gourion, D., Noll, D., Gantet, P., Celler, A., and Esquerré, J.-P., *Attenuation correction using spect emission data only*, IEEE transactions on nuclear science **49**, 2172 (2002).

[160] Yan, Y. and Zeng, G. L., *Attenuation map estimation with spect emission data only*, International journal of imaging systems and technology **19**, 271 (2009).

[161] Hebert, T. J., Gopal, S., and Murphy, P., *A fully automated optimization algorithm for determining the 3-d patient contour from photo-peak projection data in spect*, IEEE transactions on medical imaging **14**, 122 (1995).

[162] Yu, Z., Rahman, M. A., Schindler, T., Laforest, R., and Jha, A. K., *A physics and learning-based transmission-less attenuation compensation method for spect*, in *Medical Imaging 2021: Physics of Medical Imaging*, Vol. 11595 (International Society for Optics and Photonics, 2021) p. 1159512.

[163] Morton, R. J., Guy, M. J., Marshall, C. A., Clarke, E. A., and Hinton, P. J., *Variation of datscan quantification between different gamma camera types*, Nuclear medicine communications **26**, 1131 (2005).

[164] Notghi, A., O'Brien, J., Clarke, E. A., and Thomson, W. H., *Acquiring diagnostic datscan images in claustrophobic or difficult patients using a 180° configuration*, Nuclear medicine communications **31**, 217 (2010).

[165] Volterrani, D., Erba, P. A., Ignasi, C., William, S. H., and Mariani, G., *Nuclear medicine textbook*, (2019).

[166] Lapa, C., Spehl, T. S., Brumberg, J., *et al.*, *Influence of ct-based attenuation correction on dopamine transporter spect with [123i] fp-cit*, American journal of nuclear medicine and molecular imaging **5**, 278 (2015).

[167] Beauregard, J.-M., Hofman, M. S., Pereira, J. M., Eu, P., and Hicks, R. J., *Quantitative 177lu spect (qspect) imaging using a commercially available spect/ct system*, Cancer Imaging **11**, 56 (2011).

[168] El Naqa, I., *The role of quantitative pet in predicting cancer treatment outcomes*, Clinical and translational imaging **2**, 305 (2014).

[169] Akahoshi, M., Abe, K., Uchiyama, Y., *et al.*, *Attenuation and scatter correction in i-123 fp-cit spect do not affect the clinical diagnosis of dopaminergic system neurodegeneration*, Medicine **96** (2017).

[170] Jreige, M., Allenbach, G., Meyer, M., *et al.*, *I-123-ioflupane quantification in lewy body dementia and parkinson disease: Efficient role of xspect-derived absolute and relative suv*, Journal of Nuclear Medicine **61**, 1530 (2020).

[171] Cokgor, I., Akabani, G., Kuan, C.-T., *et al.*, *Phase i trial results of iodine-131–labeled antitenascin monoclonal antibody 81c6 treatment of patients with newly diagnosed malignant gliomas*, Journal of clinical oncology **18**, 3862 (2000).

Acknowledgements

I would like to take this chance to express my sincere gratitude to many people who have given me support and made this thesis possible.

First of all, I would like to thank my supervisors Prof. Freek Beekman and Dr. Marlies Goorden for guiding me through this research. Being a PhD student is not easy, and being a supervisor can be even harder.

Freek, thank you for offering me the opportunity to work as a PhD candidate in the group which lead me to the field of SPECT imaging. This thesis would not be possible without your help throughout all these years. I see a great scientist in you who is passionate and strives to invent more possibilities for revolutionary molecular imaging. You are critical about research and responsible for the products and customers. Whenever my work was questioned by you, I knew that your comments would always make my work better, although the revision process can be painful. I feel lucky that as a junior researcher with limited experience on SPECT imaging, I could get comments and advice from an expert like you who has worked in this field for more than 30 years. Also, for the first 3 years of my PhD that I spent many days in the company as an external student, you gave me a lot of support. The many trips, in Utrecht, Rotterdam and Den Haag, with colleagues in the company are beautiful memories. There are also many other things I bear gratitude, e.g. your advice on career development and support for my postdoc application.

Marlies, thank you for your supervision and availability. You are a great female scientist that I admire: smart, diligent, kind and responsible. I received so much help from you with paper revision and research design. For every submission, you helped me with writing and revising very patiently. This PhD work could not be finished without you. Now when I am writing, I always think of what your comments would be if I write it in this way. I am very lucky to have had your supervision and the opportunities to learn from you for doing research.

Beien and Minh, you are the best peer PhD colleagues I could have expected. You both are knowledgeable, friendly, and were always there when I need help. I could always easily turn to you for advice without worrying that you would be bothered. The stand-up chat in the office are such nice memories. We used to talk about study, work, trips, holidays, driving exams, etc. To me, you two are my very close friends besides colleagues. Walking through the PhD journey was tough, and you two made my journey a memorable experience. We went to two conferences together; one in Atlanta and one in Manchester.

Beien always brought ideas where to eat; Minh and I only needed to follow. And Minh would take care of Uber for the most cost-efficient transportation. How much I would miss these trips and the everyday coffee break, lunch break with you. I sincerely wish all the best with your future career.

Rob and Jan, you two are such nice group members. Although my research topic did not have a large overlap with your expertise, you were always willing to help. You were also there for the conference trip in Manchester. It was a lovely trip that I am already missing. Besides, Rob, thanks for your timely help with translation of the Dutch summary and many other things.

Trudy, thanks for all the help with administrations, booking flights, arranging hospitality, etc. You always respond quickly and have things arranged efficiently. You are a great asset to this group.

I also received lots of help from colleagues in MIlabs during the first three years of my PhD.

Brendan, you were a great helper as my supervisor in the company. Before my PhD project, you had been working on the G-SPECT. You are very busy, and still you make time to kindly and patiently help me with my PhD project for G-SPECT image acquisition and reconstruction. Thank you for all the help. I enjoyed working with you.

Chao, thank you for helping me when I was stuck at work. You are very smart. Even though I knew this at the beginning of my PhD when I heard that you were from the top 1 university in China, I was more and more convinced of this in the following years while working with you. You always gave me valuable insights for any questions. And I am still impressed by your detailed scientific explanation when we were asked about the lunar calendar.

Ruud, many thanks for helping me with experiments, radio sources, and organizing Chinese hotpot dinner. You are always there, as a friend, if I need advice. You brought me a lot of laughter as well. I have nice memories talking and working with you.

I would like to thank many colleagues that I have worked or had lunch with in Delft. Many thanks to colleagues from the biomedical imaging group at Delft: Pieter, Sasha, Jarno, Monika, and the new colleagues Arif and Valerio. Many thanks to colleagues I had coffee or lunch with in the RID building: Giácomo, Maarten, Stefan, Tianshui and Hongde.

Many thanks to colleagues from MIlabs who have helped me. Hiddo, Arian, Michiel and Stephan were my office mates for the first office I stayed at the company. I was new to things in the company at the beginning, and you were so nice and friendly to me. David, Chris, Wouter, Yutaro, Jose, Henk Tjebbe, Rene, Harald and Peggy have also given me support. Many thanks.

Many thanks to my friends in Eindhoven, the city I lived in for six years. Lin, Yang, Xi, Lina,

Xiong, Xuan, Zizheng and QiaoQi, thank you for the countless dinners we had together, and the many many poker games we played till mid-night. Especially, Lin and Yang have cooked so many times for our gathering, almost weekly. Jiong, thanks for accepting me working on the retina project in Eindhoven, and also for being my very good friend later. Tao and Yue, thank you for the dinners and many oyster picking outings we had together. These were warm and nice memories in Eindhoven. This city was my second hometown because you were there.

I also would like to thank many outstanding girls I met in Utrecht UMC: Yujie, Xiaoshan, Yuxi, Bochao. Yujie, thanks for the many presents you sent to me and visiting me in Delft. Xiaoshan and Yuxi, thank you for the gatherings we had together. Bochao, you are a lovely girl, and I believe you will be a great scientist.

Many thanks to friends in Delft for the dinners and barbecues we had together. Xinmin and Qian, thank you for the many helping hands I received from you. The shrimps you bought really made my fish tank a lively aquarium. Bei and Dan, I had lovely memories about the dinners and barbecues we had together.

Also, thanks Marius, Marleen and Wiro who helped me with my master project at BIGR group and led me to the field of medical imaging. Thanks Xiao Xuan Zi and Hua (Ma) for being my friends all these years since my master study.

Lastly, thanks to my loving parents and two elder brothers for the many years of caring for me. And thanks to my husband for the many years of friendship and accompanying.

Curriculum Vitæ

Yuan Chen

18-April-1990 Born in Hunan, China.

May 2016 — Present	Delft University of Technology, The Netherlands Ph.D. candidate Thesis: Image acquisition and attenuation map estimation for multi-pinhole clinical SPECT
Nov. 2014 — Sep. 2015	Eindhoven University of Technology, The Netherlands Research Assistant Project 1: Automatic localization of prostate cancer with multi-parametric ultrasound imaging Project 2: Automatic vessel segmentation on retina images
Sep. 2012 — Aug. 2014	Delft University of Technology, Netherlands M.Sc. in Applied Physics Thesis: Automatic detection of enlarged perivascular spaces on brain MRI
Sep. 2011 — Jun. 2012	Ulm University, Ulm, Germany Exchange student in Communication Engineering
Sep. 2009 — Feb. 2010	Sun yat-sen University, Guangdong, China Exchange student in Applied Physics
Sep. 2008 — Jul. 2012	Shandong University, Shandong, China B.Eng. in Optical Information Science and Technology

List of Publications

Peer-Reviewed Journal Article

Yuan Chen, Marlies C. Goorden, Freek J. Beekman. *Convolutional neural network based attenuation correction for SPECT DaTscans with focused striatum imaging*, Physics in Medicine and Biology **under revision**.

Yuan Chen, Marlies C. Goorden, Freek J. Beekman. *Automatic attenuation map estimation from SPECT data only for brain perfusion scans using convolutional neural networks*, Physics in Medicine and Biology **66** (2022), 065006.

Yuan Chen, Brendan Vastenhouw, Marlies C. Goorden, Freek J. Beekman. *Optimized sampling for high resolution multi-pinhole brain SPECT with stationary detectors*, Physics in Medicine and Biology **65** (2020), 015002.

Yuan Chen, Brendan Vastenhouw, Chao Wu, Marlies C. Goorden, Freek J. Beekman. *Optimized image acquisition for dopamine transporter imaging with ultra-high resolution clinical pinhole SPECT*, Physics in Medicine and Biology **63** (2018), 225002.

Conference Abstract

Yuan Chen, Marlies C. Goorden, Freek J. Beekman. *Automatic attenuation map estimation from SPECT data only for DaTscan using a convolutional neural network*, IEEE Nuclear Science Symposium and Medical Imaging Conference 2020, Boston, USA.

Yuan Chen, Marlies C. Goorden, Freek J. Beekman. *Attenuation map estimation from SPECT data only using a convolutional neural network*, IEEE Nuclear Science Symposium and Medical Imaging Conference 2019, Manchester, UK.
Recipient of Best Paper Award.

Yuan Chen, Brendan Vastenhouw, Marlies C. Goorden, Freek J. Beekman. *Optimized image acquisition for high resolution full brain perfusion SPECT*, IEEE Nuclear Science Symposium and Medical Imaging Conference 2019, Manchester, UK.

Yuan Chen, Brendan Vastenhouw, Chao Wu, Marlies C. Goorden, Freek J. Beekman. *Optimized image acquisition for dopamine transporter imaging with ultra-high resolution clinical multi-pinhole SPECT*, World Molecular Imaging Conference 2018, Seattle, USA.

Yuan Chen, Brendan Vastenhouw, Chao Wu, Marlies C. Goorden, Freek J. Beekman. *Optimized image acquisition for dopamine transporter imaging with ultra-high resolution clinical*

multi-pinhole SPECT, IEEE Nuclear Science Symposium and Medical Imaging Conference 2017, Atlanta, USA.


9 789463 842327
TU Delft